9.09 The History of the Earth's Rotation: Impacts of Deep Earth Physics and Surface Climate Variability

WR Peltier, University of Toronto, Toronto, ON, Canada

9.09.1 Polar Motion and Length-of-Day Variations Through (Geologic) Time

Observations of the evolving state of planetary rotation reveal the occurrence of variability on timescales ranging from daily, to annual, to interannual, decadal, and millennial and extending even to the timescale of hundreds of millions of years on which the process of mantle convection governs planetary evolution and to the 4.56 billion-year age of the planet itself. These variations in the state of rotation are most usefully discussed in terms of changes in the rate of planetary rotation about the instantaneous spin axis and thus variations in the length of the day, on the one hand, or in terms of the wobble of the spin axis as observed in a body-fixed frame of reference on the other. On relatively short subannual to annual timescales, variations in the length of day have been clearly shown to arise

 http://dx.doi.org/10.1016/B978-0-444-53802-4.00161-5

primarily as a consequence of the exchange of angular momentum between the solid Earth and its overlying atmosphere (e.g., Hide et al., 1980) and oceans. On the interannual timescale, an important recent discovery concerning length-of-day (l.o.d.) variability has been the documentation of a significant excitation associated with El Niño Southern Oscillation (ENSO) events (Cox and Chao, 2002; Dickey et al., 2002). Concerning the sources of wobble excitation, it is clear that on the timescale of the seasonal cycle of climate change, the excitation of the annual component of wobble variability is due to the interhemispheric exchange of atmospheric mass. The Chandler wobble, however, a free oscillation of the Earth's spin axis in a body-fixed frame of reference with a period close to 14 months, is apparently significantly forced by the dynamic state of the oceans (e.g., Gross, 2000) and by the atmosphere. These most recent analyses of the problem of Chandler wobble excitation, to be reviewed in what follows, appear to have finally resolved what had remained an unresolved problem for decades.

On the longer timescale of millennia, both of these 'anomalies' in the Earth's rotation exhibit apparent secular variations that are caused primarily by the Late Pleistocene cycle of glaciation and deglaciation (Peltier, 1982) that has been an enduring feature of climate system variability for the past 900 000 years of Earth history (e.g., Deblonde and Peltier, 1991). A primary focus of the discussion to follow in this chapter will be upon the manner in which, through the process of glacial isostatic adjustment (GIA), these ice-age engendered variations in the Earth's rotation feed back upon postglacial relative sea-level history, thus enabling detailed tests to be performed on the quality of the theory that has been developed to compute the rotational response to the GIA process (Peltier, 2005). The importance of an accurate attribution of the source of excitation of the observed secular changes in the l.o.d. and polar motion to the GIA process concerns the important role that these observations may be invoked to play in the inference of the viscosity of the deep Earth, a parameter that is required in the construction of models of the mantle convection and continental drift processes.

An interesting additional aspect of the history of the Earth's rotation on the timescale of the Late Pleistocene ice-age cycle concerns the way in which temporal variations in the precession and obliquity components of the evolving geometry of the Earth's orbit around the Sun, forced by gravitational n-body effects in the solar system, have been employed to refine the timing of the ice-age cycle itself (Shackleton et al., 1990).

On the very longest timescales on which the thermal evolution of the planet is governed by the mantle convection process, there also exists the distinct possibility that relatively rapid and large amplitude changes in the rotational state could have occurred in association with an 'avalanche effect' during which the style of the mantle convective circulation switches from one characterized by significant radial layering of the thermally forced flow to one of 'whole mantle' form (e.g., Solheim and Peltier, 1994a,b). This process could conceivably act so as to induce the inertial interchange true polar wander (IITPW) instability that was suggested initially by Gold (1955) and that has recently been invoked by Kirschvink et al. (1997) as plausibly having occurred in the early Cambrian period of Earth history.

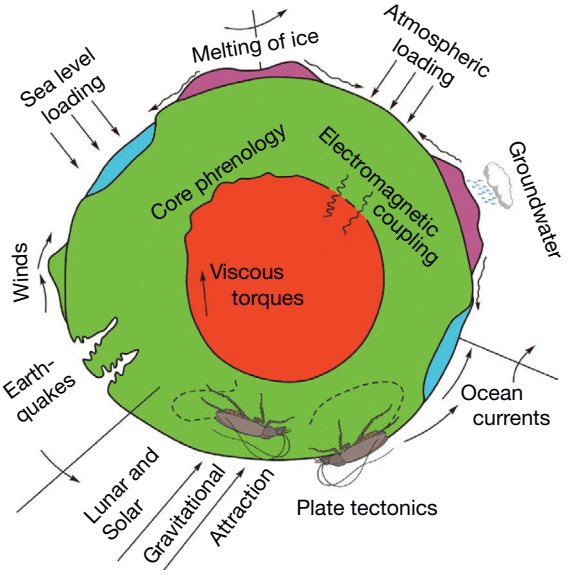

Figure 1 Schematic diagram illustrating the range of processes that contribute to the excitation of variations in the rotational state of the planet. The centipedes in the figure, which are a modification of the beetles employed by Gold (1955) for the same illustrative purpose, are intended to represent the contribution to rotational excitation due to the mantle convection process. This schematic is a modification of that in Lambeck (1980a) paper commenting upon the important paper of Hide et al. (1980).

Figure 1 provides a schematic depiction of the extremely broad range of processes that contribute to the excitation of variations in the Earth's rotation on all timescales. The centipedes in the sketch, following the colorful analogy by Gold (1955), are intended to represent, by their ability to move over the surface and thereby slowly (?) modify the moment of inertia tensor of the planet, the excitation of a rotational response due to the action of the internal mantle convective mixing process. How this component of the rotational excitation might be most accurately described is still a matter of considerable debate, as will be discussed in the final section of this chapter.

9.09.2 Theoretical and Observational Background I: Angular Momentum Conservation on Subannual to Interannual Timescales

9.09.2.1 Theoretical Preliminaries

An instantaneous state of the Earth's rotation is described entirely by the three Cartesian components of the planet's evolving angular velocity vector with components $\omega_i(t)$. The evolution of the angular velocity vector is itself determined by a solution of the classical Euler equation describing the conservation of angular momentum of a system subjected to external torques τ_j, as

$$\frac{\mathrm{d}}{\mathrm{d}t}\left(J_{ij}\omega_i\right) + \in_{ijk}\omega_j J_{kl}\omega_l = \tau_j \qquad [1]$$

in which J_{ij} are the elements of the moment of inertia tensor and $\in_{ijk}$ is the Levi-Civita (alternating) tensor. Restricting

attention to small departures from a modern state of steady rotation with angular velocity Ω_o, we may construct a solution to eqn [1], accurate to the first order in perturbation theory, by expanding

$$\omega_i = \Omega_o(\delta_{i3} + m_i);\ m_i = \omega_i/\Omega_o \quad [2a]$$

$$J_{11} = A + I_{11} \quad [2b]$$

$$J_{22} = B + I_{22} \quad [2c]$$

$$J_{33} = C + I_{33} \quad [2d]$$

$$J_{ij} = I_{ij},\ i \neq j \quad [2e]$$

Substitution of these expansions into eqn [1], keeping only terms of first order, leads to the standard set of governing equations for polar wander and the l.o.d., respectively (see, e.g., Munk and MacDonald (1960)), as

$$\left.\begin{aligned} \frac{dm_1}{dt} + \frac{(C-B)}{A}\Omega_o m_2 &= \Psi_1 \\ \frac{dm_2}{dt} + \frac{(C-A)}{B}\Omega_o m_1 &= \Psi_2 \end{aligned}\right\} \text{ polar wander} \quad [3a,b]$$

$$\left.\frac{dm_3}{dt} = \Psi_3\right\} \text{ length of day} \quad [3c]$$

in which the 'excitation functions' are defined as

$$\Psi_1 = \left(\frac{\Omega_o}{A}\right) I_{23} - \frac{(dI_{13}/dt)}{A} + \tau_1 \quad [4a]$$

$$\Psi_2 = -\left(\frac{\Omega_o}{B}\right) I_{13} - \frac{(dI_{23}/dt)}{B} + \tau_2 \quad [4b]$$

$$\Psi_3 = -\left(\frac{I_{33}}{C}\right) + \tau_3 \quad [4c]$$

Now, it is important to recognize that we are here distinguishing between two different ways of describing the rotational excitation, due, respectively, to externally applied torques τ_i and to 'internally' originating perturbations I_{ij} to the moment of inertia tensor. In this section, a brief review will be provided of our current understanding of the nature and origins of the variations in the Earth's rotation that occur on subannual to interannual timescales. These variations are most simply understood by considering the rotational response of an 'almost rigid' solid Earth to externally applied torques derivative of the action upon it of the atmosphere and oceans and to the redistributions of mass that occur both subseasonally and interannually within these fluid components of the Earth system. As we will see in Section 9.09.4, it will be more natural to describe the process involved in the excitation of millennial timescale variations of the Earth's rotation by invoking 'internally' generated changes in the moment of inertia tensor.

9.09.2.2 Variations in the l.o.d.

Focusing first upon changes in the l.o.d. on relatively short timescales, the connection of variations on these timescales to the exchange of angular momentum between the solid Earth and overlying atmosphere was first established most clearly in the important paper by Hide et al. (1980). It will be useful to revisit their initial order of magnitude arguments here in order to fix ideas. If one denotes the total axial angular momentum of the Earth system by the sum $M + M_a$, as in Hide et al., which has the approximate value $5.85 \times 10^{33}\,kg\,m^2\,s^{-1}$ and divides this by the axial moment of inertia that the atmosphere plus solid Earth system would have if the whole system were in a state of rigid body rotation, namely, $I + I_a \approx 8.04 \times 10^{37}\,kg\,m^2$, then one would obtain for the angular velocity of the Earth system $\Omega_R \approx 0.726 \times 10^{-4}\,rad\,s^{-1}$. A consequence of the fact that the atmosphere of the Earth is differentially heated by the Sun is that the complex general circulation of its atmosphere is characterized by a marked differential rotation between it and the solid Earth. This leads to a net increase in the angular momentum of the atmosphere by the (approximate) amount $\delta M_a \approx 1.5 \times 10^{26}\,kg\,m^2\,s^{-1}$ as determined on the basis of direct atmospheric observations. Given the approximate value of the moment of inertia of the atmosphere, $I_a \approx 1.42 \times 10^{32}\,kg\,m^2$, this leads to an approximate value for the change in angular velocity of magnitude $\delta M_a/I_a \approx 10^{-6}\,rad\,s^{-1} \approx 3 \times 10^{-8}\Omega_R$, or given that the l.o.d. is just $2\pi/\Omega_R$, one obtains an approximate magnitude for the change in the length of the day due to the solar differential heating forced general circulation of the atmosphere of 3×10^{-3} s. Detailed astronomical measurements by the Bureau Internationale de l'Heure (BIH) directly demonstrate that on the annual and interannual timescales, this is in fact the order of magnitude of the variations in the l.o.d. observed.

Figure 2 reproduces a figure from the original paper of Hide et al. in which a detailed analysis of the angular momentum budget of the atmosphere was performed by evaluating the axial component of the relative angular momentum m_a as

$$m_a = \frac{a^2}{g}\int_{-\pi/2}^{+\pi/2}\int_0^{2\pi}\int_0^{p_g} u(p, \theta, \lambda, t)\cos^2\theta\, dp\, d\lambda\, d\theta \quad [5]$$

in which a is the radius of the Earth, g is the surface gravitational acceleration, u is the zonal component of the velocity of atmospheric air in a frame of reference rotating with the solid Earth, p is atmospheric pressure, p_g is the pressure at the surface of the Earth, θ is the latitude, λ is the longitude, and t is the time. The radial part of the required volume integral has been converted to an integral over pressure by employing the hydrostatic approximation. Based upon the use of independent sets of reanalysis data from the UK Meteorological Office and from the US National Meteorological Center, the authors inferred the changes in the l.o.d. that should have occurred if the atmosphere was simply exchanging its axial angular momentum with that of the solid Earth. These estimates of temporal changes in the l.o.d. were compared directly to the astronomically derived measurements provided by the BIH over a 9-month period extending from the winter of 1978 to the summer of 1979. These results, which have since only been reconfirmed by later and more detailed analysis, clearly establish that on these short timescales, changes in the l.o.d. are primarily associated with the exchange of angular momentum between the solid Earth plus oceans and its overlying atmosphere.

Considered over a period of many decades, rather than years, one begins to see additional structure in the variability in the l.o.d. that includes the measurable influence of an effect due to the changing axial component of the moment of inertia of the solid Earth, an influence that is generally measured in

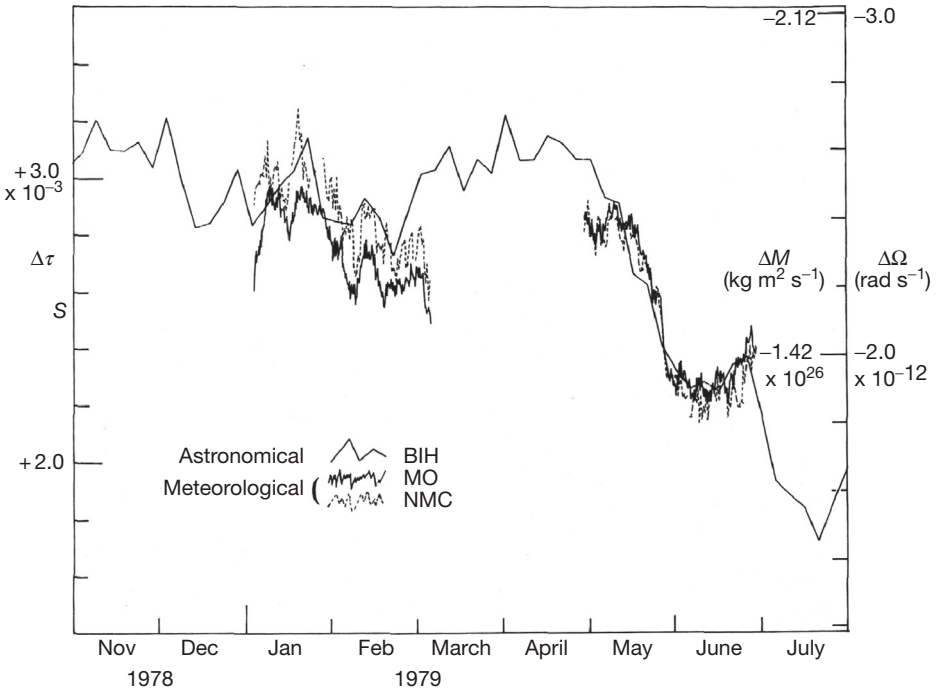

Figure 2 Comparison of the expected changes in the length of the day, represented by the parameter $\triangle\tau$ measured in milliseconds and derived from the meteorological results (either UK Meteorological Office (MO) or the US National Meteorological Center), with the observed changes based upon the astronomical measurements of the Bureau International de l'Heure (BIH). Reproduced from Hide R, Birch NT, Morrison LV, Shea DJ, and White AA (1980) Atmospheric angular momentum fluctuations an changes in the length of the day. *Nature* 286: 114–117.

terms of a parameter $\dot{J}_2$, which will be discussed at length in subsequent sections of this chapter (the 'dot' above the symbol 'J' here represents time differentiation). The parameter J_2 is itself the nondimensional degree 2 and order 0 coefficient in the spherical harmonic expansion of the gravitational field of the planet. The connection between this parameter and the angular velocity of the planet and thus the l.o.d. is given by the following simple expression:

$$\dot{J}_2 = \frac{3}{2}\frac{C}{a^2 m_e}\dot{m}_3 \qquad [6]$$

in which 'a' and 'm_e' are the Earth's radius and mass, respectively, and $m_3 = \omega_3/\Omega_0$.

Superimposed upon the secular trend in J_2, an effect we will show to be unambiguously connected to the GIA process, the analyses by Cox and Chao (2002) were the first in which an interannual timescale variation of this quantity was detected that was apparently associated with the ENSO phenomenon. This internal oscillatory ENSO mode of climate system variability is supported by coupling between the atmosphere and the oceans across the equatorial Pacific region and recurs on a timescale that varies from 3 to 7 years. Further analysis of this interannual variability of J_2, which at the time of writing is still not entirely understood, was presented by Dickey et al. (2002) in which an attempt was made to ascribe the El Niño influence to a particular related process having to do with "a recent surge in subpolar glacial melting and by mass shifts in the Southern, Pacific and Indian Oceans." Figure 3, from the Dickey et al. paper, displays a set of time series of the parameter J_2 that marked (**A**) being the time series of the raw data from the BIH. Although prior to approximately late 1996 the time series reveals a consistent secular decrease in the value of this parameter, such that a least-squares best fit of a straight line to the data delivers the best estimate of $\dot{J}_2$ of approximately -2.9×10^{-11} year^{-1}, beginning in late 1996, the onset of a significant deviation developed from this secular trend. The timing of this excursion in the time series was interpreted as being associated with the onset of the intense El Niño event that occurred in 1998. As we will discuss in Section 9.09.4.3 in the succeeding text, this interpretation has become questionable. The remaining time series shown in Figure 3 display the alterations to it that obtain upon successive removal of the influence of the forcing associated with four plausible influences, respectively, in (**B**) integrated ocean effects as determined using a data-constrained ocean model, in (**C**) subpolar glacier wasting effects, in (**D**) integrated atmospheric effects derived on the basis of National Center for Environmental Prediction (NCEP) reanalysis data, and in (**E**) integrated groundwater effects based upon NCEP reanalysis data. Although it remains an issue as to whether the attribution of the influence of ENSO upon the J_2 excursion as due to an enhanced wasting of subpolar glaciers is correct, there can be no doubt that the warming associated with the strong 1998 ENSO event appears to have induced a substantial variation in the l.o.d. Although the BIH data prior to 1984 were not of sufficient accuracy to generate a longer time series of the variability in this parameter that is equally useful as that shown in Figure 3, it is nevertheless extremely important that the dominant secular variation in the time series is essentially the same as that previously inferred on the basis of the analysis of ancient eclipse observations as we will discuss in the following sections of this chapter.

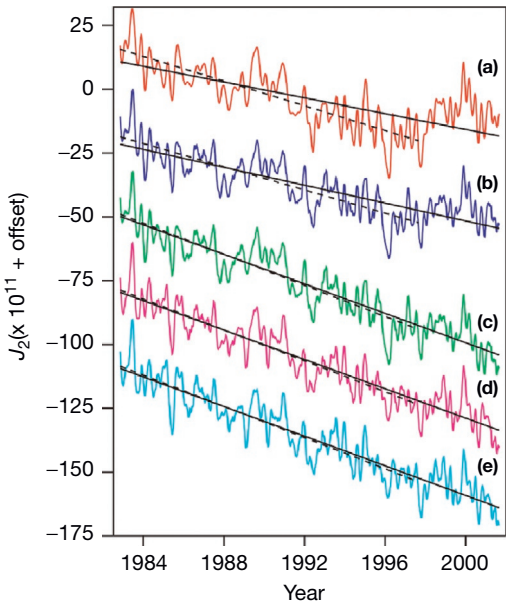

Figure 3 (a) The geodetically observed time series of the parameter J_2 over the time period 1983–2002 and residuals (b)–(e) obtained by successive removal of modeled source terms related, respectively, to the processes of (b) integrated ocean effects, (c) subpolar glacial effects, (d) integrated atmospheric effects, and (e) integrated groundwater effects. Note that these analyses did not anticipate the results of Roy and Peltier (2011), which demonstrated that the rate of secular variation of this parameter underwent a marked change early in the 1990s (see **Section 9.09.4.3**). Reproduced from Dickey JO, Marcus SL, de Viron O, and Fukumori I (2002) Recent Earth oblateness variations: Unravelling climate and postglacial rebound effects. *Science* 298: 1975–1977.

9.09.2.3 Polar Motion: The Annual and Chandler Wobbles

The Chandler wobble or free Eulerian nutation of the spin axis of the Earth in a body-fixed frame of reference was first discovered by Chandler (1891). A detailed theory of the Chandler wobble from a 'normal-mode' perspective was first presented by Dahlen and Smith (1975) and has been more fully developed since by Wahr (1982, 1983) whose investigation focused upon the important influence of the atmosphere and oceans on the phenomenon. Although manipulation of eqn [3a,b] in the preceding text predicts the existence of a simple harmonic 'free' oscillation of frequency $\sigma_R = \Omega_0(C-A/A)$, to which I will subsequently refer as the Chandler wobble frequency of the rigid Earth, this expression substantially errs in its prediction of the period of the actual Chandler wobble because of the importance of these components of the Earth system and the existence of the fluid core upon wobble dynamics.

Furthermore, this system of equations would predict a Chandler wobble that would have infinite 'Q' in the sense that, once excited, it would never decay in amplitude.

Aside from the Chandler wobble, which has a variable amplitude that ranges between ~100 and 200 milliarcseconds (mas) in the angular displacement of the pole, several additional physical processes contribute to the complete range of polar motion that is observed using the space-geodetic techniques of very long-baseline interferometry (VLBI), satellite and lunar laser ranging, and Global Positioning System interferometry. These include (1) a forced annual wobble with an amplitude of ~100 mas, which occurs in response to the seasonal variability of the atmosphere and oceans, (2) a weaker but quasiperiodic variation on decadal timescales with an amplitude of ~30 mas that is often referred to as the Markowitz wobble, and, the most important from the perspective of this chapter, (3) a linear trend corresponding to a secular drift in the position of the pole that is presently occurring at a rate of ~3.5 mas year^{-1}. The latter ultra-low-frequency feature, which will be a primary focus in the main body of this chapter to follow, is the polar motion counterpart to the secular variation in the l.o.d. represented in terms of $\dot{J}_2$ and discussed in the last subsection. The rate of 3.5 mas year^{-1} corresponds to a rate of drift of the pole across the surface of ~0.95° My^{-1}.

Although each of the highest-frequency contributions to the motion of the pole has been studied in depth, it has been the development of a detailed understanding of the Chandler wobble that has attracted the greatest interest, as the explanation of its excitation mechanism has proved to be extremely elusive. Attempts were made to ascribe its excitation to the atmosphere (Wahr, 1983; Wilson and Haubrich, 1976), to core–mantle interactions (Jault and Le Mouel, 1993; Rochester and Smiley, 1965), to the occurrence of earthquakes (Gross, 1986; Sauriau and Cazanave, 1985), and even to continental water storage (Chao et al., 1987; Kuehne and Wilson, 1991). More recent research has however suggested that the primary excitation may in fact be oceanographic (Gross, 2000), although aided to significant degree by the atmosphere.

In attempting to attribute the excitation of the Chandler wobble to any particular forcing function, it is also important to recognize that this important mode of rotational free oscillation also has a finite 'Q' so that if all sources of excitation were to vanish, the amplitude of the polar motion would decay to zero. For this reason, a simple heuristic model, derivable from the linearized Liouville equations [3a,b] in the preceding text, given the extremely small amplitude of the observed motion, is just (e.g., Lambeck, 1980b)

$$\Gamma + \frac{i}{\sigma_{CW}}\frac{d\Gamma}{dt} = \chi(t) \qquad [7]$$

in which $\Gamma = x_p - iy_p$ where x_p and y_p are, respectively, the displacements of the pole from the Conventional International Origin (CIO) along the Greenwich and 90°W meridians and σ_{CW} is the complex Chandler wobble frequency of the real anelastic Earth for which the 'Q' of the Chandler wobble has been estimated by Wilson and Vincente (1990) to be 179 with 1σ bounds of 74 and 789. Equation [7] describes simple harmonic motion in the complex plane subject to the forcing represented by the function $\chi(t)$, an excitation function that Wahr (1982) had shown may be written as

$$\chi(t) = \frac{1.61}{\Omega_o(C-A)}\left[h(t) + \frac{\Omega_o I(t)}{1.44}\right] \qquad [8]$$

in which the complex valued function $I(t) = I_{13}(t) + iI_{23}(t)$ where I_{13} and I_{23} are the perturbations of the inertia tensor associated with the variations in the mass distributions in the atmosphere and the oceans that may be responsible for wobble excitation. The function $h(t) = h_1(t) + ih_2(t)$ represents changes

of relative angular momentum associated, for example, with atmospheric winds and ocean currents. The numerical factors 1.61 and 1.44, respectively, account for the influences of core decoupling and the yielding of the solid Earth under the weight of the changing surface mass load.

In the paper by Gross (2000), detailed analyses were presented of Chandler wobble excitation that were based upon the assumption of the validity of the estimates of the Chandler period and Q by Wilson and Vincente (1990), an analysis in which the estimates were based upon the longest time series of polar motion data available at that time (86 years), the only study in which the duration of the data set analyzed was longer than the e-folding time for the decay of the Chandler amplitude. Since the polar motion is resonant at the Chandler period, most analyses of the excitation mechanism have been conducted in the frequency domain by direct comparison of the spectrum of the rotational response to the spectrum of the excitation as computed on the basis of assumed *a priori* knowledge of a range of plausible excitation mechanisms. Figure 4(a), from Gross (2000), presents such a comparison, one that focused upon assessing the effectiveness of both atmospheric and oceanographic processes.

Inspection of this figure demonstrates, as shown earlier by Wilson and Haubrich (1976) and Wahr (1983), that the net effect of the sum of atmospheric wind and pressure fluctuations (determined on the basis of NCEP/National Center for Atmospheric Research (NCAR) reanalysis data) is insufficient to explain the Chandler excitation in terms of availability as compared to required power (whereas this excitation is entirely adequate insofar as the annual wobble is concerned as previously remarked). On the other hand, when the oceanographic excitation is added to the forcing at the Chandler period, with

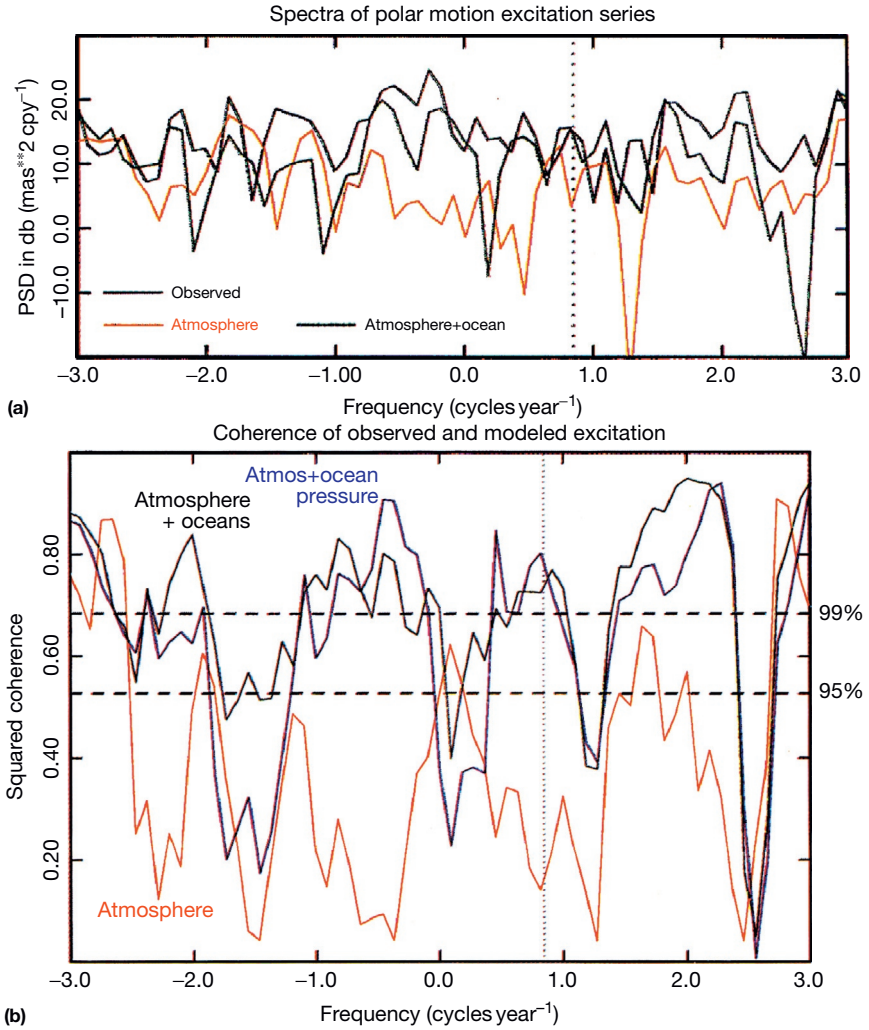

Figure 4 (a) The power spectral density (PSD) estimates in decibels (dB) computed from time series of polar motion excitation functions ($\chi(t)$) for the period 1985.0–1996.0 for the observed polar motion excitation function derived from space-geodetic Earth's rotation measurements (black curve), for the sum of the excitation functions due to atmospheric wind and pressure changes (red curve) where the atmospheric pressure term is that computed by assuming the validity of the inverted barometer approximation, and for the sum of all atmospheric and oceanic excitation processes (green curve). (b) Squared coherence between the observed polar motion excitation functions in the period 1985.0–1996.0 and the excitation functions due to the sum of atmospheric wind and (inverted barometer) pressure changes (red curve), due to the sum of atmospheric pressure and ocean bottom pressure fluctuations (blue curve), and due to the sum of all atmospheric and oceanic excitation processes. Reproduced from Gross RS (2000) The excitation of the Chandler wobble. *Geophysical Research Letters* 27: 2329–2342.

this determined on the basis of output of the MIT ocean general circulation model (Ponte et al, 1998) driven by 12 h wind stress and 24 h surface heat and freshwater fluxes from NCEP, the total power in the forcing at the Chandler period was found to fit the requirements of the observations extremely well.

In the Gross (2000) paper, this analysis in terms of the available power in the total forcing by the atmosphere and ocean was complemented by an analysis of the coherence between the observed excitation and modeled excitation, the results from which are reproduced here in Figure 4(b). Inspection of results of this analysis demonstrates that the atmospheric excitation alone is not coherent with the observed excitation, whereas the atmospheric plus oceanographic excitation is highly coherent with the observed excitation. Through detailed analysis, the author of this paper concludes that "the Chandler wobble is being excited by a combination of atmospheric and oceanic processes" and that "the single most important mechanism exciting the Chandler wobble has been ocean bottom pressure fluctuations which contribute about twice as much excitation power in the Chandler frequency band as do atmospheric pressure fluctuations." It would appear on the basis of these results that our understanding of the Chandler component of Earth's polar motion has become as well understood as are the similarly high-frequency variations in the l.o.d. discussed in the previous subsection.

In the following section of this chapter, I will extend the characteristic timescale of our interest in the Earth's rotation history to include the last million years, a period during which the surface of the solid Earth has been continuously subjected to a quasicyclic glaciation–deglaciation cycle involving extremely large exchanges of mass between the oceans and the surface of the continents on which massive continental ice sheets formed and episodically disintegrated. It should not be surprising, given the magnitude of this mass redistribution over the surface, that this 'ice-age cycle' has involved that it had, and continues to have, a profound impact upon the rotational state of the planet. What is often seen as very surprising, however, is the fidelity with which the Earth has conspired to remember the details of both the rotational excitation to which it was subjected and the response to it.

9.09.3 Theoretical Background II: The Viscoelastic Rotational Response to the Late Pleistocene Ice-Age Cycle

Given the extremely broad range of processes that contribute to the excitation of variations in the Earth's rotational state (see Figure 1), it is always an issue as to the degree to which one is able to uniquely ascribe the observed variability in a particular range of timescales to any one particular process. On the characteristic timescale of millennia and tens to hundreds of millennia, however, it is apparently the case that the excitation mechanism is so strongly dominated by the Late Pleistocene process of glaciation and deglaciation that such unambiguous attribution has come to be quite generally accepted. This is due to the advances that have been achieved over the past several decades in the development of a detailed viscoelastic theory of the GIA process.

9.09.3.1 The Global Theory of the GIA Process

The modern theory of global glacial isostasy addresses the question of the changes in the Earth's shape, gravitational field, and rotational state caused by the variations in surface mass load that occur when water is irreversibly removed from the oceans and delivered to the high-latitude continents to form large accumulations of land ice. Since the amount of water removed from the ocean basins in a typical 100 ky cycle of glaciation and deglaciation has been such as to cause mean sea level to fall by $\sim$120 m, it should not be surprising that this process has been accompanied by highly significant variations in the Earth's rotation, variations of sufficient amplitude as to leave indelible imprints in the geologic record of relative sea-level history. The dominant timescale of the Late Pleistocene ice-age cycle is most clearly appreciated on the basis of oxygen-isotopic measurements made on the calcium carbonate shells (tests) of foraminifera that are a ubiquitous component of the sedimentology of deep-sea sedimentary cores. One example of such a record is shown in Figure 5. The oxygen-isotopic anomaly $\delta^{18}O$, as measured on the tests of foraminifera extracted as a function of depth from such cores, provides a high-quality proxy for the amount of ice that existed on the continents as a function of time in the past, determined by the depth in the core from which the individual samples are taken (Shackleton, 1967). This is a simple consequence of the fact that the process whereby water is irreversibly removed from the oceans to build the ice sheets is a process that fractionates mass. $H_2{}^{16}O$ is preferentially removed from the oceans through the evaporation and precipitation processes whereby water is eventually delivered to the high-latitude continents as snow, resulting in an ocean left behind that is anomalously rich in the isotopologue $H_2{}^{18}O$ at a time in the past when large-scale continental ice sheets are in place, an anomaly that is recorded in the shells of foraminifera so long as these remain open systems. This isotopic anomaly is defined as

$$\delta^{18}O = \left(\frac{\left[{}^{18}O/{}^{16}O\right]_{\text{sample}}}{\left[{}^{18}O/{}^{16}O\right]_{\text{standard}}} - 1 \right) \qquad [9]$$

The record shown in Figure 5, from Ocean Drilling Program Site 677 in the Panama Basin off the west coast of the South American continent, remains one of the highest-resolution records available and was employed in Shackleton et al. (1990) to refine the entire chronology of the Pleistocene glacial epoch (see Section 9.09.7 in the succeeding text for a detailed discussion). Inspection of the power spectrum of this record, which is also shown in this figure for both the most recent and previous million years of the Pleistocene epoch, will show that for the most recent 900 000 years (see Deblonde and Peltier (1993) for a statistical assessment of the sharpness of this 'mid-Pleistocene climate transition'), the climate system has been dominated by a quasicyclic variation of ice cover with an average period of $\sim$100 000 years. Also evident by inspection of the power spectrum of this record are the additional weaker spectral peaks, one at a period of $\sim$41 000 years and a triplet of very weak spectral lines at periods of 19 000, 22 000, and 23 000 years. These additional spectral lines are associated with the component of ice-volume variability that is directly forced by the weak variations in solar radiation caused by the

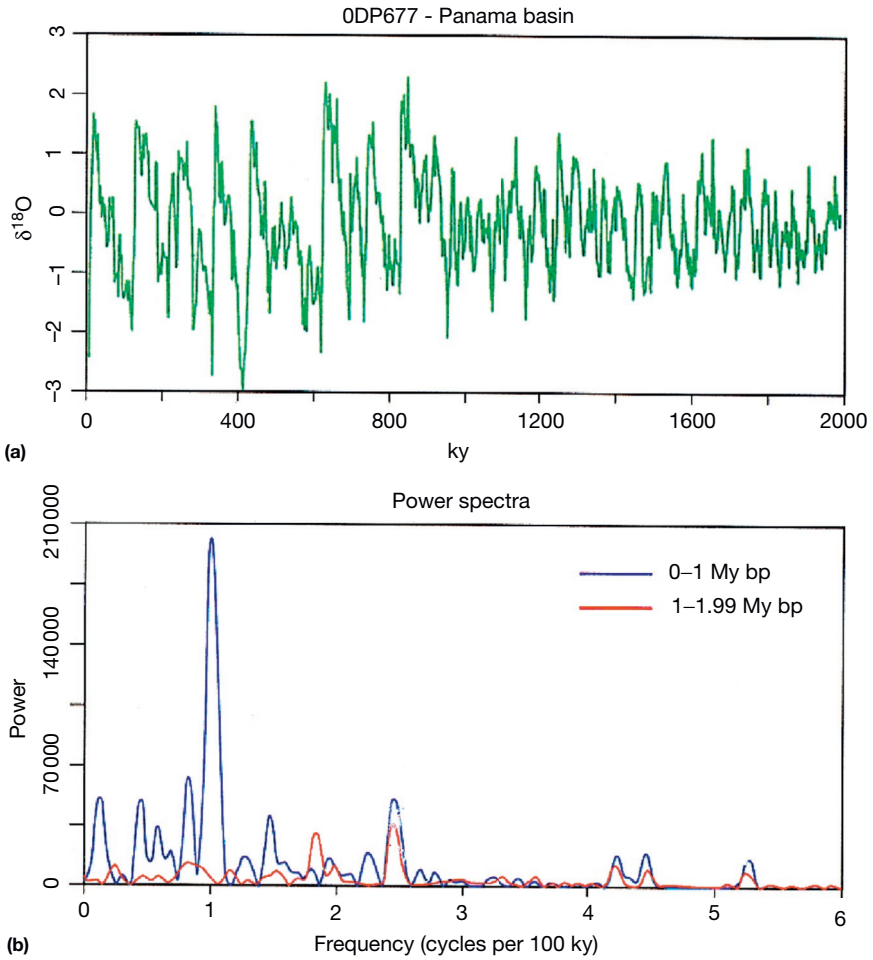

Figure 5 Oxygen-isotopic record from Ocean Drilling Program Site 677 in the Panama Basin extending to 2 million years before present from Shackleton et al. (1990). Also shown are the power spectra for the first and last million years of the record illustrating the onset of the 100 000-year cycle of glaciation and deglaciation in mid-Pleistocene time. Also evident in this continental ice-volume proxy record are the additional spectral lines associated with the variations of orbital obliquity and with the eccentricity modulation of the precessional effect (see **Section 9.09.7** for further discussion).

changing geometry of the Earth's orbit around the Sun that are in turn due to gravitational n-body effects in the solar system. Because the Earth and Sun are not alone in the solar system, the planet's orbit around the Sun does not consist of a time-invariant Keplerian ellipse but rather one whose ellipticity varies slowly with time at dominant periods of 100 000 and 400 000 years. Furthermore, as the planet continuously executes its almost elliptical orbit around the Sun, the axis, about which it spins and which presently makes an angle of $\sim 23.5^\circ$ with the plane of the ecliptic, also varies with time such that this angle (the so-called obliquity of the spin axis) varies with a dominant period of 41 000 years. As will be discussed more fully in **Section 9.09.7** of this chapter, it is these sources of variability in the Earth's rotational state together with the precession of the equinoxes that are responsible for the onset of the individual ice ages themselves.

Given the large variations in surface mass load that have accompanied the growth and decay of continental ice sheets over the past ~900 000 years of Earth history, during which a quasiperiodic ice-age cycle has persisted with a period of ~100 000 years, it should be clear that the key to understanding the excitation of the Earth's rotation that has accompanied the process must involve the ability to construct a detailed model of the variations in the moment of inertia tensor caused by the process. This requires the solution of what I have come to call the sea-level equation (SLE), an equation that accurately describes the way in which water must be distributed over the ocean basins when ice sheets melt so as to ensure that the evolving surface of the ocean remains a surface of constant gravitational potential. An initial version of this equation was first solved in papers by Clark et al. (1978) and Peltier et al. (1978) based upon the combination of results obtained in Peltier (1974, 1976), Farrell and Clark (1976), and Peltier and Andrews (1976). Since the completion of this original work, the theory underlying the SLE has been significantly extended, however, and it is these extensions that have proved crucial to the accurate understanding of the important role that the Earth's rotational response to the GIA process plays in the theory.

The solution of the SLE delivers a prediction of the history of relative sea-level change, $S(\theta, \lambda, t)$ say, that is caused by an assumed known history of the variations in continental ice

mass, represented by a history of continental ice-sheet thickness variations $I(\theta,\lambda,t)$. In these expressions, θ is latitude, λ is longitude, and 't' is time. The form of the SLE that relates these quantities is as follows:

$$S(\theta,\lambda,t)=C(\theta,\lambda,t)\left[\int_{-\infty}^{t}\mathrm{d}t'\iint_{\Omega}\mathrm{d}\Omega'\left\{L(\theta',\lambda',t')G_{\phi}^{L}(\phi,t-t')+\Psi^{R}(\theta',\lambda',t')_{R}G_{\phi}^{T}(\phi,t-t')\right\}+\frac{\Delta\Phi(t)}{g}\right] \quad [10]$$

In this equation, $C(\theta,\lambda,t)$ is the 'ocean function,' which is, as defined by Munk and Macdonald (1960), unity over the oceans and zero over the continents. The function 'C' is time-dependent because the removal of water from, or its addition to, the ocean basins causes the coastline to migrate, an effect that may be accurately computed on a global basis using the methodology described in Peltier (1994). The space–time-dependent surface mass load per unit area 'L' in the aforementioned equation has the composite form

$$L(\theta,\lambda,t)=\rho_{\mathrm{I}}I(\theta,\lambda,t)+\rho_{\mathrm{W}}S(\theta,\lambda,t) \quad [11]$$

in which ρ_{I} and ρ_{W} are the densities of ice and water, respectively. The angle ϕ in the Green functions G_{ϕ}^{L} and ${}_{R}G_{\phi}^{T}$ is the angular separation between the source point (θ',λ') and the field point (θ,λ). The function $\Psi^{R}(\theta,\lambda,t)$ is the variation of the centrifugal potential due to the changing rotational state of the Earth that is caused by the surface loading and unloading process associated with the ice-age cycle. Following Dahlen (1976), this may be expressed, to first order in perturbation theory, in terms of the following spherical harmonic expansion, as

$$\Psi^{R}(\theta,\lambda,t)=\Psi_{00}Y_{00}(\theta,\lambda,t)+\sum_{m=-1}^{+1}\Psi_{2m}Y_{2m}(\theta,\lambda,t) \quad [12]$$

with

$$\Psi_{00}=\frac{2}{3}\omega_{3}(t)\Omega_{\mathrm{o}}a^{2} \quad [13a]$$

$$\Psi_{20}=-\frac{1}{3}\omega_{3}(t)\Omega_{\mathrm{o}}a^{2}\sqrt{4/5} \quad [13b]$$

$$\Psi_{2,-1}=(\omega_{1}-i\omega_{2})(\Omega_{\mathrm{o}}a^{2}/2)\sqrt{2/15} \quad [13c]$$

$$\Psi_{2,+1}=-(\omega_{1}+i\omega_{2})(\Omega_{\mathrm{o}}a^{2}/2)\sqrt{2/15} \quad [13d]$$

The ω_i in the aforementioned equations are to be obtained as solutions to the appropriate version of eqns [3] in Section 9.09.2 in the preceding text, the form from which the externally applied torques τ_i have been removed as the rotational excitation in this case must be considered to be internally generated. The remaining terms in the SLE consist of the surface mass loading and tidal potential loading Green functions, which have been shown in Peltier (1976) and Peltier et al. (2012) to have the mathematical representations

$$G_{\phi}^{L}(\phi,t)=\frac{a}{m_{e}}\sum_{l=0}^{\infty}\left(1+k_{l}^{L}(t)-h_{l}^{L}(t)\right)P_{l}(\cos\theta) \quad [14a]$$

$${}_{R}G_{\phi}^{T}(\phi,t)=\frac{1}{g}\sum_{l=0}^{\infty}\frac{(2l+1)}{4\pi}\left(1+k_{l}^{T}(t)-h_{l}^{T}(t)\right)P_{l}(\cos\theta) \quad [14b]$$

in which k_l^T, h_l^T are the viscoelastic tidal potential loading Love numbers and k_l^L, h_l^L are the corresponding surface mass loading Love numbers of Peltier (1974). The renormalization factor $(2l+1)/4\pi$ in eqn [14b] is needed to ensure that the centrifugal potential introduces only local influence as discussed in detail in Peltier et al. (2012). Peltier (1976, 1985) had shown that the time-domain viscoelastic Love numbers that appear in eqns [14a] and [14b] may be expressed, in the case of impulsive point mass or centrifugal potential loading at the surface of the planet, in the form of the following normal-mode expansions:

$$k_{l}^{T}(t)=k_{l}^{T,E}\delta(t)+\sum_{j=1}^{M}q^{l}{}_{j}e^{-s_{j}^{l}t} \quad [15a]$$

$$h_{l}^{T}(t)=h_{l}^{T,E}\delta(t)+\sum_{j=1}^{M}r^{l}{}_{j}e^{-s_{j}^{l}t} \quad [15b]$$

$$k_{l}^{L}(t)=k_{l}^{L,E}\delta(t)+\sum_{j=1}^{M}q_{j}^{L}e^{-s_{j}t} \quad [15c]$$

$$h_{l}^{L}(t)=h_{l}^{L,E}\delta(t)+\sum_{j=1}^{M}r_{j}^{L}e^{-s_{j}^{l}t} \quad [15d]$$

In these normal-mode expansions, the $k_l^{T,E}, h_l^{T,E}, k_l^{L,E}$, and $h_l^{L,E}$ are the elastic surface mass load and tidal potential loading Love numbers of Farrell (1972), the s_j^l are the inverse relaxation times of a discrete set of normal modes of viscoelastic gravitational relaxation determined as the zeros of an appropriate secular function (Peltier, 1985) or by collocation (Peltier, 1974, 1976), and the amplitudes $q_j^l, r_j^l, q_j^l, r_j^l$ are the residues at these poles. Insofar as understanding of the polar wander component of the rotational response of the planet to the GIA process is concerned, the parameter k_2^T plays an especially crucial role as will be made clear in what follows. Solutions of the SLE are computed using an extension of the pseudo-spectral algorithm of Mitrovica and Peltier (1991).

9.09.3.2 Computation of the Rotational Response to Ice–Earth–Ocean Interactions in the Ice Age

The important role of the Love number $k_2^T(t)$ may be understood by returning to eqns [4] of Section 9.09.2 and focusing upon the polar wander component of the rotational response of the planet in circumstances in which it may be assumed that externally applied torques vanish ($\tau_i \equiv 0$) and noting that in this case, we must distinguish between two distinct but intimately related sources of excitation. The first of these derives from the perturbations of inertia caused by the direct affect of the isostatic adjustment process, an influence that may be represented in the form (e.g., Peltier, 1982)

$$I_{ij}^{\mathrm{GIA}}=\left(\delta(t)+k_{2}^{L}(t)\right)*I_{ij}^{R}(t) \quad [16]$$

in which the $I_{ij}^{R}(t)$ are the perturbations of inertia that would be obtained due to the variations in surface mass load if the Earth were a rigid body rather than viscoelastic and the symbol * represents the temporal convolution operation.

The second contribution to the perturbations of inertia is that due to the changing rotation itself, this may be derived from an application of a linearized version of MacCullagh's formula (e.g., see Munk and MacDonald (1960)) as

$$I_{13}^{\mathrm{ROT}} = \left(\frac{k_2^T * a^5 \omega_1 \omega_3}{3G}\right) = \left(\frac{k_2^T}{k_f}\right) * m_1 (C-A) \qquad [17a]$$

$$I_{23}^{\mathrm{ROT}} = \left(\frac{k_2^T * a^5 \omega_2 \omega_3}{3G}\right) = \left(\frac{k_2^T}{k_f}\right) * m_2 (C-A) \qquad [17b]$$

with

$$k_f = \left(\frac{3G}{a^5 \Omega_o^2}\right)(C-A) \qquad [17c]$$

in which $A=B$ has been assumed in eqns [4] and $k_2^T(t)$ is the tidal potential loading Love number of degree 2 defined in the preceding text, the parameter that will be seen to play a crucial role in what follows. Equally critical for the arguments to be presented is the so-called fluid Love number k_f, the value of which is determined entirely on the basis of the well-known equatorial flattening of the planet that is represented by the difference between the polar and equatorial moments of inertia $(C-A)$ in eqn [17c]. Substituting in eqn [17c] for Newton's gravitational constant 'G' the Earth's radius 'a' (for which we might take either the equatorial or polar value in order to investigate two hypothetical values for k_f), the present-day rate of angular rotation Ω_o, and the polar and equatorial moments of inertia C and A, respectively, taking all data from the tabulation of Yoder (1995) (see www.agu.org/references/geophys/4_Yoder.pdf), one obtains for the value of k_f, taking 'a' to be the polar radius, that

$$k_f \cong 0.9414 \qquad [18a]$$

or taking 'a' to be the equatorial radius, we obtain, alternatively,

$$k_f = 0.9382 \qquad [18b]$$

An important part of the discussion to follow will involve understanding of the connection between k_f and $\mathrm{Lim}_{t\to\infty} k_2^T(t)$, the infinite time asymptote of the viscoelastic tidal loading Love number of degree 2 in response to a constant tidal potential applied at $t=0$ and maintained.

Since the solution of eqn [3c] for the change in the axial rate of rotation is uncomplicated, it will suffice to focus in what follows on the solution of eqns [3a] and [3b] for the polar wander component of the response to surface loading. This focus is furthermore motivated by the fact that the influence of polar wander strongly dominates the influence of rotational feedback upon sea-level history. Substituting eqns [17a] and [17b] together with eqn [16] into eqns [3a] and [3b] using [4a] and [4b] for the excitation functions, the Laplace-transform forms of the equations that follow are simply

$$s m_1 + \sigma\left(1 - \frac{k_2^T(s)}{k_f}\right) m_2 = \Psi_1(s) \qquad [19a]$$

$$s m_2 + \sigma\left(1 - \frac{k_2^T(s)}{k_f}\right) m_1 = \Psi_2(s) \qquad [19b]$$

where

$$\sigma = \Omega_o \frac{(C-A)}{A} \qquad [19c]$$

is the Chandler wobble frequency of the rigid Earth, 's' is the Laplace transform variable, and again, $A=B$ has been assumed. The Laplace-transformed forms of the excitation functions in eqns [19a] and [19b] are simply

$$\Psi_1(s) = \left(\frac{\Omega_o}{A}\right) I_{23}(s) - \left(\frac{s}{A}\right) I_{13}(s) \qquad [20a]$$

$$\Psi_2(s) = \left(\frac{\Omega_o}{A}\right) I_{13}(s) - \left(\frac{s}{A}\right) I_{23}(s) \qquad [20b]$$

with

$$I_{ij}(s) = \left(1 + k_2^L(s)\right) I_{ij}^{\mathrm{Rigid}}(s) \qquad [20c]$$

Now, eqns [19a] and [19b] are elementary algebraic equations for $m_1(s)$ and $m_2(s)$, and these may be solved, neglecting terms of order s^2/σ^2, as is appropriate for the analysis of a physical process evolving on a timescale that is much longer than the period of the Chandler wobble, to obtain

$$m_1(s) = \left(\frac{\Omega_o}{A\sigma}\right)\left[\frac{1 + k_2^L(s)}{1 - \dfrac{k_2^T(s)}{k_f}}\right] I_{13}^{\mathrm{Rigid}}(s) = H(s) I_{13}^{\mathrm{Rigid}}(s) \qquad [21a]$$

$$m_2(s) = H(s) I_{23}^{\mathrm{Rigid}}(s) \qquad [21b]$$

A convenient shorthand form for the solution vector $(m_1, m_2) = \underline{m}$ is to write

$$\underline{m}(s) = \frac{\underline{\Psi}^L(s)}{\left[1 - \dfrac{k_2^T(s)}{k_f}\right]} = H(s)\left(I_{13}^{\mathrm{Rigid}}(s), I_{23}^{\mathrm{Rigid}}(s)\right) \qquad [22a]$$

where

$$\underline{\Psi}^L(s) = \left[\left(\frac{\Omega_o}{A\sigma}\right)\left(1 + k_2^L(s)\left(I_{13}^{\mathrm{Rigid}}(s), I_{23}^{\mathrm{Rigid}}(s)\right)\right)\right] \qquad [22b]$$

From eqns [22], it will be clear that the polar wander solution $\underline{m}(s)$ will depend critically upon the ratio $k_2^T(s)/k_f$. This fact was more fully exposed in the analysis of Peltier (1982) and Wu and Peltier (1984) who rewrote the Laplace-transformed domain forms of $k_2^T(s)$ and $k_2^L(s)$ as (e.g., see eqn [61] of Wu and Peltier (1984))

$$k_2^T(s) = k_2^T(s=0) - s\sum_{j=1}^{N} \frac{\left(q_j'/s_j\right)}{(s+s_j)} \qquad [23a]$$

$$k_2^L(s) = (-1 + \ell_s) - s\sum_{j=1}^{N} \frac{(q_j/s_j)}{(s+s_j)} \qquad [23b]$$

in which the superscript $\ell=2$ on q_j^2, r_j^2, s_j^2 has been suppressed for convenience. Substituting eqn [23a] into eqn [22], this may be rewritten as

$$\underline{m}(s) = \frac{\underline{\Psi}^L(s)}{\left[1 - \dfrac{k_2^T(s=0)}{k_f}\right] + \dfrac{s}{k_f}\displaystyle\sum_{j=1}^{N} \frac{\left(q_j'/s_j\right)}{(s+s_j)}} \qquad [24]$$

In discussing the formal inversion of eqn [24] into the time domain, I will distinguish for the purpose of this chapter the

results that follow from the application of an important modified form of this equation from those that follow from the complete eqn [24].

9.09.3.3 The 'Equivalent Earth Model' Approach of Munk and MacDonald (1960): An Approximate Solution

Since the surface of the Earth is broken into a large number of individually rigid lithospheric 'plates' whose boundaries are in general weak, it should be the case that, at the large horizontal scale represented by spherical harmonic degree 2, the effective $k_2^T(s=0)$ will be close to k_f since in this limit, the absence of strength at plate boundaries will enable the planet as a whole to adjust to the tidal (rotational) forcing as if the planet had no surface lithosphere at all. This is highly plausible on physical grounds as the product $\mathrm{Lim}_{s\to 0} s k_2^T(s)$, via the Tauberian theorem (e.g., see Widder (1946)), is identical to $\mathrm{Lim}_{t\to\infty} k_2^T(t)$. That $k_2^T(s=0)$ does tend towards k_f in response to the sustained application of the rotational forcing as the thickness of the lithosphere tends to zero will be clear on the basis of Figure 6 (see also Table 5 in Wu and Peltier (1984)). Based upon Figure 6, it will be clear that the deviation of $k_2^T(s=0)$ from k_f is by $<1\%$ for either of the plausible values of k_f denoted by the dashed lines. It is an interesting question as to whether this small deviation is physical as opposed to being an artifact due to a slight error in the radial variation of density in the PREM model that is being employed to represent the unperturbed form of the spherically symmetrical approximation to the planet upon which the GIA process is superimposed. For present purposes, I will consider that the difference is plausibly physically meaningful and derivative of the action of the mantle convection process. The mathematical methods required to invert eqn [24] under the assumption

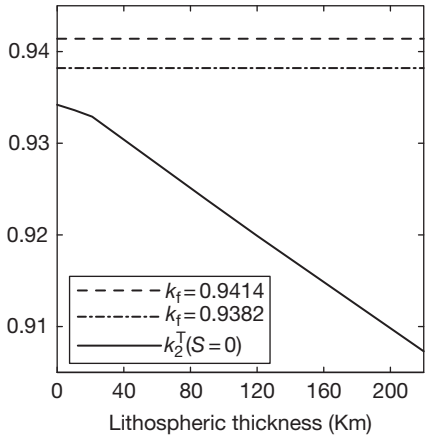

Figure 6 The infinite time asymptotic value of the tidal potential loading Love number of degree 2 is shown as a function of lithospheric thickness. This infinite time limit is identical to the limit in which the Laplace transform variable 's' equals zero. Also shown in the figure are two plausible values of the fluid Love number k_f, which is a nondimensional constant determined by the observed flattening of Earth's shape as measured by the difference between the polar and equatorial moments of inertia (C − A). Note that the difference between $k_2^T(s=0)$ and k_f in the limit of zero lithospheric thickness is $<1\%$ for either one of the two values of k_f. See text for further discussion.

$$1 - \frac{k_2^T(s=0)}{k_f} \equiv 0 \qquad [25]$$

were presented in Peltier (1982) and Wu and Peltier (1984) and will not be repeated here. This is the assumption upon which the equivalent Earth model (EQM) approach of Munk and MacDonald (1960) is based. However, it will be important to make the point immediately that eqn [24] subject to eqn [25] does not constitute a mathematically unstable formulation as it remains finite in the infinite time limit by the Tauberian theorem mentioned in the preceding text, contrary to the apparent claim made by Mitrovica et al. (2005).

9.09.3.4 A Formulation that Retains the Difference Between $k_2^T(s=0)$ and k_f

In this case, the assumption $k_2^T(s=0)=k_f$ that is at the heart of the 'equivalent Earth model' approach is abandoned, and the Laplace transform domain impulse response is then

$$H(s) = \left(\frac{\Omega_o}{A\sigma}\right) \frac{1 + k_2^L(s)}{\frac{s}{k_f}\sum_{j=1}^{N} \frac{(q_j/s_j)}{(s+s_j)} + \varepsilon} \qquad [26a]$$

where

$$\varepsilon = 1 - \frac{k_2^T(s=0)}{k_f} \qquad [26b]$$

As will become clear, even though ε is a small quantity (especially in the case that the finite thickness of the lithosphere may be neglected in the limit $t\to\infty$), retaining it in expression [26a] for the impulse response could have a significant impact upon the solution as the rotational response of the system is modified. Now, the construction of the solution for the time-domain form of the impulse response $H(t)$ proceeds in this case as in the case based upon the EQM assumption, although the result differs from a physical perspective, especially in circumstances in which, as we will see, a perturbation to the inertia tensor is applied and maintained over a sufficiently long timescale. In this case, it is useful to make the distinction between the Chandler wobble frequency of a rigid Earth σ and the Chandler wobble frequency of the viscoelastic Earth σ_o, by employing the definition

$$\sigma_o = \frac{(k_2^T(s=0) - k_2^{TE})}{k_2^T(s=0)}\sigma \qquad [27]$$

We may then rewrite the expression for $H(s)$ as

$$H(s) = \left(\frac{\Omega_o}{A\sigma_o}\right) \frac{(1 + k_2^L(s))}{\left((1-\varepsilon)s\sum_{i=1}^{N} \frac{g_j}{s+s_j}\right) + \varepsilon'} \qquad [28a]$$

with

$$\varepsilon' = \varepsilon\frac{\sigma}{\sigma_o} \qquad [28b]$$

and,

$$g_j = \frac{q_j'/s_j}{\sum_j (q_j'/s_j)} \qquad [28c]$$

The inversion of $H(s)$ into the time domain now proceeds by expanding the sum in the denominator of eqn [28a] in the form

$$\sum_{j=}^{N}\frac{g_j}{(s+s_j)}=\frac{Q_{N-1}(s)}{\prod_{j=1}^{N}(s+s_j)}=\frac{\prod_{j=1}^{N-1}(s+\lambda_j)}{\prod_{j=}^{N}(s+s_j)} \qquad [29]$$

since $\sum g_j \equiv 1$. Then, we have, suppressing for the moment the factor $(\Omega_o/A\sigma_o)$,

$$H(s)=\frac{\prod_{j=1}^{N}(s+s_j)\left[1+k_2^L(s)\right]}{(1-\varepsilon)s\prod_{i=1}^{N-1}(s+\lambda_i)+\varepsilon'\prod_{j=1}^{N}(s+s_j)} \qquad [30]$$

Now, substituting for the function $1+k_2^L(s)$ from eqn [23b], we obtain

$$H(s)=\frac{\prod_{j=1}^{N}(s+s_j)\ell_s}{(1-\varepsilon)s\prod_{i=1}^{N-1}(s+\lambda_i)+\varepsilon'\prod_{i=1}^{N}(s+s_i)}$$

$$+\sum_{j=1}^{N}\frac{(-q_j/s_j)s\prod_{i\neq j}^{N}(s+s_i)}{(1-\varepsilon)s\prod_{i=1}^{N-1}(s+\lambda_i)+\varepsilon'\prod_{i=1}^{N}(s+s_i)} \qquad [31a]$$

$$=\frac{\prod_{j=1}^{N}(s+s_j)\ell_s}{(1-\varepsilon+\varepsilon')\prod_{i=1}^{N}(s+\kappa_i)}+\sum_{j=1}^{N}\frac{(-q_j/s_j)s\prod_{i\neq j}^{N}(s+s_j)}{(1-\varepsilon+\varepsilon')\prod_{i=1}^{N}(s+\kappa_i)} \qquad [31b]$$

where the κ_i are the N roots of the polynomial in the denominator of the two terms in eqn [31a]. This expression for the impulse response may be further reduced by rewriting the ratios of products as follows:

$$\frac{\prod_{j=1}^{N}(s+s_j)}{\prod_{j=1}^{N}(s+\kappa_i)}=1-\frac{q'(s)}{\prod_{i=1}^{N}(s+\kappa_i)} \qquad [32a]$$

where now,

$$q'(s)=\prod_{j=1}^{N}(s+\kappa_i)-\prod_{j=1}^{N}(s+s_j) \qquad [32b]$$

and

$$\frac{s\prod_{i\neq j}^{N}(s+s_i)}{\prod_{j=1}^{N}(s+\kappa_i)}=1-\frac{R_j'(s)}{\prod_{i=1}^{N}(s+\kappa_i)} \qquad [33a]$$

with

$$R_j'(s)=\prod_{i=1}^{N}(s+\kappa_i)-s\prod_{i\neq j}^{N}(s+s_i) \qquad [33b]$$

We then have, for the Laplace transform of the impulse response, the expression

$$H(s)=\frac{\ell_s}{(1-\varepsilon+\varepsilon')}\left\{1-\frac{q'(s)}{\prod_{i=1}^{N}(s+\kappa_i)}\right\}$$

$$+\frac{1}{(1-\varepsilon+\varepsilon')}\sum_{j=1}^{N}\left(-\frac{r_j}{s_j}\right)\left\{1-\frac{R_j'(s)}{\prod_{i=1}^{N}(s+\kappa_i)}\right\} \qquad [34a]$$

or

$$H(s)=\frac{\ell_s-\sum_{j=1}^{N}r_j/s_j}{(1-\varepsilon+\varepsilon')}-\frac{\ell_s q'(s)}{(1-\varepsilon+\varepsilon')\prod_{i=1}^{N}(s+\kappa_i)}$$

$$+\frac{1}{(1-\varepsilon+\varepsilon')}\sum_{j=1}^{N}\frac{(q_j/s_j)R_j'(s)}{\prod_{i=1}^{N}(s+\kappa_i)} \qquad [34b]$$

Denoting $\ell_s-\sum_{j=1}^{N}r_j/s_j=1+k_2^{LE}=D_1$, say, then we may further reduce the expression for the impulse response to

$$H(s)=\frac{D_1}{(1-\varepsilon+\varepsilon')}-\frac{1}{(1-\varepsilon+\varepsilon')}\left\{\frac{\ell_s q'(s)-\sum_{j=1}^{N}(q_j/s_j)R_j'(s)}{\prod_{i=1}^{N}(s+\kappa_i)}\right\} \qquad [35]$$

The inverse Laplace transform of this expression is such that the solution in the present case, in which $k_2^T(s=0)\neq k_f$, is just

$$m_1(t)=\frac{1}{(1-\varepsilon+\varepsilon')}\left(\frac{\Omega_o}{A\sigma_o}\right)$$

$$\left\{\left[\ell_s-\sum_{j=1}^{N}\frac{r_j}{s_j}\right]I_{13}^{\text{Rigid}}(t)+\sum_{i=1}^{N}E_i'e^{-\kappa_i t}*I_{13}^{\text{Rigid}}(t)\right\} \qquad [36a]$$

$$m_2(t)=\frac{1}{(1-\varepsilon+\varepsilon')}\left(\frac{\Omega_o}{A\sigma_o}\right)$$

$$\left\{\left[\ell_s-\sum_{j=1}^{N}\frac{r_j}{s_j}\right]I_{23}^{\text{Rigid}}(t)+\sum_{i=1}^{N}E_i'e^{-\kappa_i t}*I_{23}^{\text{Rigid}}(t)\right\} \qquad [36b]$$

where

$$E_i'=\left\{-\ell_s q'(-\kappa_i)+\sum_{j=1}^{N}\frac{r_j}{s_j}R_j'(-\kappa_i)\right\}/\prod_{i=j}^{N}(\kappa_j-\kappa_i) \qquad [36c]$$

The polar wander velocity vector components are obtained simply by time differentiation of eqns [36a] and [36b]. It is useful to compare the results in eqn [36] to those obtained under the EQM assumption. In the limit $\varepsilon \to o$, we have $\kappa_N=0$ and $\kappa_i=\lambda_i$, which are the $N-1$ relaxation times that govern the system in this limit (see Wu and Peltier (1984)). In this case, the parameter E_N' in the in the preceding text becomes

$$E_N'=-\frac{\ell_1 q(o)}{\prod_{j=1}^{N-1}(\kappa_j-\kappa_N)}=-\frac{\ell_s q(o)}{\prod_{j=1}^{N-1}\lambda_i} \qquad [37]$$

and the EQM result is fully recovered. The mathematical analysis leading to the aforementioned analytic result for the polar

wander speed prediction embodied in eqn [36] is original to Peltier and Luthcke (2009) from which paper the aforementioned analysis has been extracted.

In order to compare the temporal histories of the rotational anomalies predicted in the two cases in response to an ice-age cycle of loading and unloading, it will be important to proceed by keeping as many features of the Earth model fixed as possible. To this end and for much of the rest of this chapter, I will focus primarily upon the VM2 viscosity model of Peltier (1996b) and the simple multilayer approximation to it that has been referred to as VM5a by Peltier and Drummond (2010) that will be employed together with the PREM radial elastic structure of Dziewonski and Anderson (1981). However, I will also discuss the results for simple two-layer viscosity models that may be directly compared to the earlier results for such models (e.g., see Peltier and Jiang (1996)).Equally important, of course, will be the model of glaciation and deglaciation that is employed to represent the surface mass load forcing. This is described in the next subsection.

9.09.3.5 Models of the History of Variations in the Elements of Earth's Moment of Inertia Tensor

As stated in the preceding text, the surface mass load forcing associated with the ice-age cycle of the Late Quaternary will, for the most part, be taken to be that either of the ICE-5G (VM2) model of Peltier (2004) or of the ICE-6G (VM5a) model of Peltier et al. (2014) that has been designed to eliminate the flaws in the North American and Antarctic components of the loading history identified in Argus and Peltier (2010) and Argus et al. (2011). **Figure 7** shows the distribution of the continental ice sheets at the Last Glacial Maximum (LGM) 26 000 years ago compared with that in the modern climate system of the Holocene along with the detailed variations of the vertical mean buoyancy frequency of the oceans for these two epochs according to the detailed reconstructions of atmosphere–ocean climate for these two epochs described in Peltier and Solheim (2004). **Figure 8** compares the contribution to the eustatic rise of sea level from LGM to the present for the ICE-5G (VM2) model with that of the ICE-6G-A (VM5a) refined model for each of the primary regions from which significant deglaciation occurred subsequent to LGM. ICE-6G is characterized by a significant geographic redistribution of the surface mass load. The most important of these changes, which the interested reader will find discussed in detail in Peltier et al. (2014); Argus et al. (2014), involves a significant redistribution of mass over the North American continent and a diminution of the mass loss from Antarctica during post-LGM deglaciation and the elimination of significant mass loss from the interior of East Greenland. In both models, meltwater pulse 1A in the Barbados record (see the succeeding text) is assumed to derive primarily from the northern hemisphere although ICE-6G envisions a small contribution to this pulse from Antarctica as well. Meltwater pulse 1B in the Barbados record is assumed to derive entirely from Antarctica in both models. It should also be noted that the ~128 m net

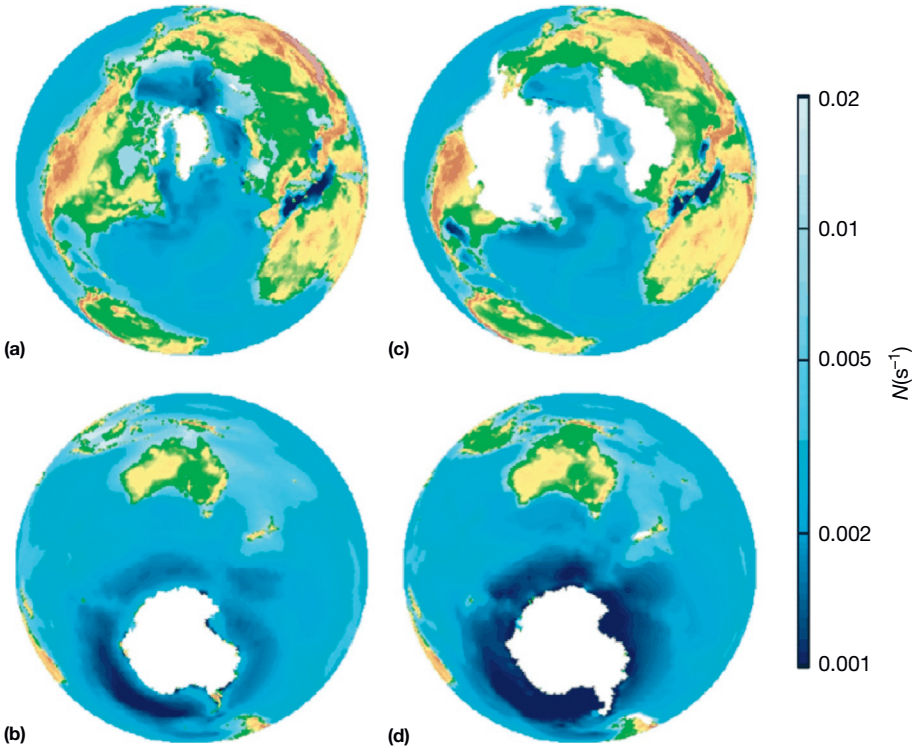

Figure 7 The difference between the distribution of land ice at LGM and the vertically averaged static stability (Brunt–Väisälä frequency '*N*') of the LGM ocean as compared with the modern ocean. The latter data are provided by the coupled atmosphere–ocean model integrations for the Last Glacial Maximum period of Peltier and Solheim (2004) and for the modern ocean by the same model operating under modern boundary conditions. These data are required for the reconstruction of the tidal regime by direct numerical solution of Laplace's tidal equation. Reproduced from Griffiths SD and Peltier WR (2008) Mega-tides in the glacial ocean and rapid climate change. *Geophysical Research Letters* 35: L08605, http://dx.doi.org/10.10292008GL033263.

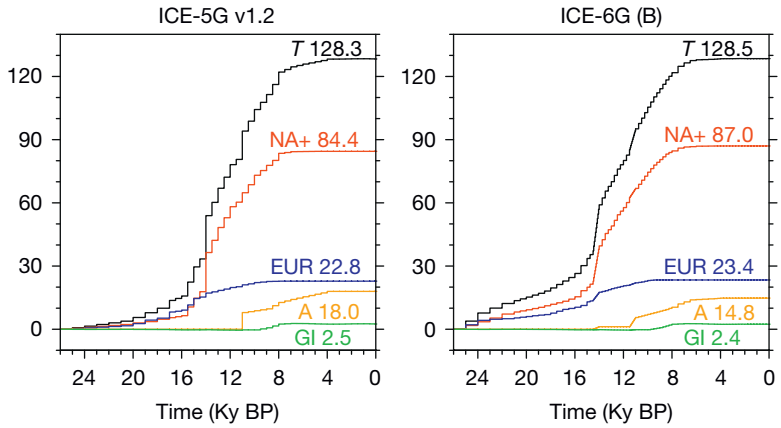

Figure 8 Ice-equivalent eustatic sea-level curves for the ICE-5G (VM2) and the ICE-6G (VM5a) models of the last glacial–interglacial transition and the contributions from each of the main regions from which land ice was lost. By ice-equivalent eustatic sea level, I mean the rise of sea level expected on the basis of the volume of water produced by the melting ice divided by the present-day surface area of the oceans. If the variation in the surface area of the oceans were taken into account, the glacial–interglacial eustatic rise would increase by ~10 m (e.g., see Peltier (2007a) for a detailed discussion). For the purpose of constructing this figure, I have left out the contributions from the Patagonian ice sheet and from the mountain glaciers of New Zealand, which explains why the sum over all regional ice masses does not exactly equal the total. This is done so as to provide a specific number for the contribution to eustatic sea-level rise for Antarctica with adding needless clutter to the diagrams. As discussed fully in the text, the sharp onset of Antarctic deglaciation at meltwater pulse 1B time ~11 500 years ago is constrained by data from sedimentary cores raised from the Antarctic shelf (see Figure 10 in the succeeding text and the discussion of these data in MacKintosh et al. (2011)). Notable is that in both of these reconstructions, LGM has been assumed to have occurred at ~26 000 years before present rather than the conventionally assumed age of 21 000 years ago. The data on the basis of which this revision is required were presented in Peltier and Fairbanks (2006). Of further importance is that the net rise of ice-equivalent eustatic sea level exceeds the conventionally assumed 120 m only because the timing of LGM has been pushed back to 26 000 years before present.

eustatic rise during deglaciation is greater than the usually assumed maximum of ~120 m only because the timing of LGM has been assumed to have been reached by 26 000 years before present rather than by the usually assumed time of 21 000 years before present. In both models, the sea-level depression at this conventional time is actually somewhat less than 120 m.

Since the relative sea-level data set from the island of Barbados has been employed to validate the total surface mass load, it will be useful to consider the extent to which the ICE-6G (VM5a) model of Peltier et al. (2014) reconciles the observed sea-level history at this site. **Figure 9**, which presents the extended compilation of Barbados data from Peltier and Fairbanks (2006), compares this observed RSL history with that predicted using the refined ICE-6G (VM5a) model of the GIA process and the SLE formalism as the red curve. On the same figure and shown as the red step discontinuous curve, the ice-equivalent eustatic sea-level history for this model is shown. The LGM ice-equivalent eustatic low stand of the sea in the ICE-6G (VM5a) model, assuming the modified LGM age of 26 ka proposed by Peltier and Fairbanks (2006) for the time of deepest glaciation, is ~128 m. This exceeds the usually assumed depth of the eustatic low stand of the sea, as previously discussed, only because the timing of LGM has been pushed back to 26 ka from the usually assumed age of 21 ka. The necessity of this reinterpretation has been defended in Peltier and Fairbanks (2006). By the ice-equivalent eustatic curve, I mean the variation of globally averaged sea level deduced directly on the basis of the time-dependent ratio of the volume of water generated by melting ice, taking into account the difference in density between ice and water, divided by the *modern* surface area of the oceans. This purposefully neglects the impact of the changing surface area of the oceans that accompanies the ice-age cycle itself so that the change in eustatic level is solely a function of the changing ice volume. The value of 128 m is still extremely close to the conventional oxygen isotope-derived estimate of ~120 m (e.g., see Shackleton (2000)), which was based upon the assumption that the depth of the LGM low stand was being accurately measured by the Barbados data itself. In the recent paper of Oba and Irino (2012), further evidence is provided of the validity of this depth of the eustatic low stand of the sea. It is a further important property of the extended Barbados record of Peltier and Fairbanks that the data appear to strongly reject the hypothesis of Yokoyama et al. (2000) that a strong meltwater pulse occurred at 19 ka. In the ICE-6G reconstruction, such rapid melting events are taken to have occurred only at the times of meltwater pulses 1A and 1B originally identified by Fairbanks (1989) of respective ages of 14.2 and 11.5 ka and which are clearly evident in **Figure 9**.

Also evident by inspection of the previous **Figure 8** is that the contribution to ice-equivalent eustatic sea-level rise from the Antarctic continent in version 1.2 of the ICE-5G (VM2) and ICE-6G (VM5a) models is characterized by a significant abrupt rise at ~11 500 years before present. This late onset of Antarctic melt-back has always been a characteristic of the ICE-NG sequence of models, it having been argued (e.g., see Peltier (2005)) that this region was the most likely source of the meltwater pulse 1B event that is clearly evident in the extended Barbados sea-level record discussed in Peltier and Fairbanks (2006). Very recently, this assumption in the ICE-NG reconstructions has been strikingly verified by the dating of an hiatus that has been observed to characterize the sedimentary

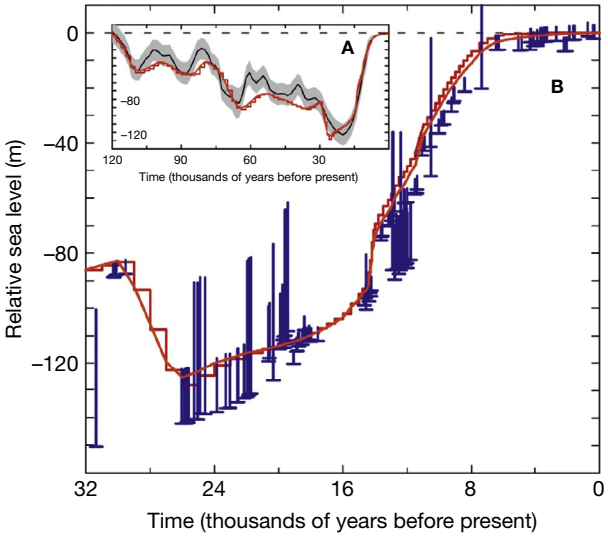

Figure 9 The fit of the predicted relative sea-level history at the island of Barbados to the extended coral-based data set from this location tabulated in Peltier and Fairbanks (2006) for model ICE-6G (VM5a). The blue symbols with error bars of various lengths represent these new Barbados data. Those data represented by the shorter error bars of 5 m length derive from the *Acropora palmata* species of coral that provide the best constraints on sea level. The data represented by the error bars on intermediate 20 m length derive from the *Montastrea annularis* species of coral. The data represented by the longest error bars derive from either the *Porites astreoides* species or the *Diploria* species. The inset to the figure shows the comparison between the eustatic history of the ICE-6G model and the complete 10^5-year glacial cycle with that inferred by Waelbroeck et al. (2002) based upon benthic δ^{18}O records corrected for the influence of the change in abyssal ocean temperature. It is notable that the GIA-based and paleoceanographic models are very close in terms of eustatic sea level.

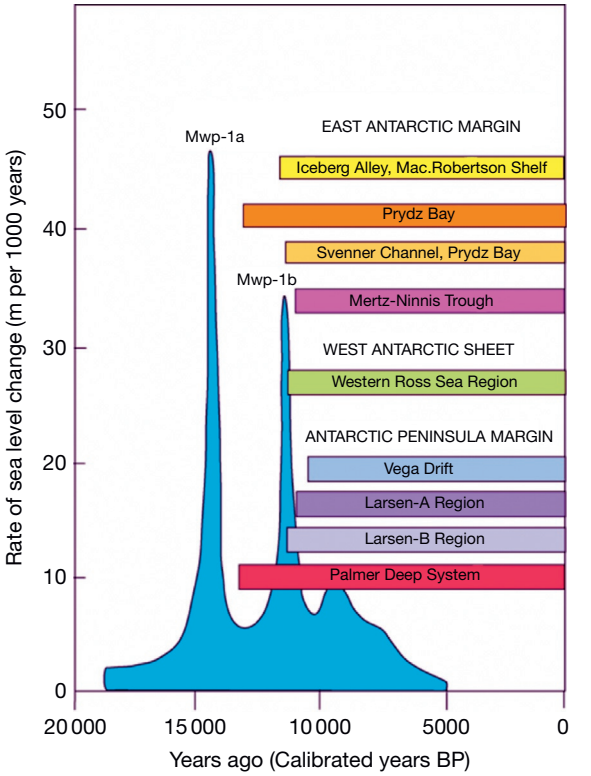

Figure 10 The timing of the onset of pullback of Antarctic ice from the shelf break surrounding the continent determined on the basis of the age of the hiatus in each of the sedimentary cores that marks the transition to the onset of continuous marine sedimentation following a period during which such sedimentation was absent. The data are those from the paper of MacKintosh et al. (2011) and the figure is redrawn from one provided to this author by Eugene Domack. Notable is the fact that at almost all locations from which such sedimentary cores have been raised, the timing of the onset of ice loss from Antarctica is coincident with meltwater pulse 1B in the Barbados record. These data directly refute the notion that any significant contribution to the earlier meltwater pulse 1A event could have originated from Antarctica.

stratigraphy of a very large number of sedimentary cores that have been raised from the shelf outboard of the current coastline of Antarctica. The sedimentology above the hiatus in each core is characterized by continuous marine sedimentation, whereas below the hiatus, marine sedimentation is absent. At each of the sites of these sedimentary cores, the hiatus is interpreted as representing the time at which the grounded ice, which extended out to the shelf break at LGM, first pulled back towards the present coastline (e.g., See Domack et al. (2005) and MacKintosh et al. (2011)). The age of the hiatus is therefore the age of the initial onset of significant Antarctic deglaciation. Inspection of the available data (from the paper by MacKintosh et al. (2013)) shown in **Figure 10** demonstrates that the time of onset of deglaciation is effectively coincident with the timing of meltwater pulse 1B in the Barbados record of sea-level history. These new observational results effectively rule out the suggestion in Clark et al. (2002) that the primary source of the earlier and more intense meltwater pulse 1A event was Antarctica. Peltier (2005) discussed additional evidence on the basis of which this suggestion appears to be implausible, and Tarasov and Peltier (2005, 2006) had provided further discussion of the Clark et al. (2002) suggestion. A sequence of predictions of relative sea-level histories based upon the ICE-5G (VM2) model at a sequence of well-dated sites from Scotland derivative of isolation basin-based inferences of RSL (see Peltier et al. (2002) for a detailed discussion of these data) appears to further reinforce the hypothesis of an Antarctic origin for meltwater pulse 1B. As discussed in Peltier et al. (2002), the highly nonmonotonic nature of these RSL curves, which are so well fit by the theoretical predictions (see also **Figure 23** in the succeeding text for a single example of these records from the Arisaig site), is significantly a consequence of the assumed late glacial melting event emanating from Antarctica and its abrupt onset as is characteristic of the ICE-5G v1.2 and ICE-6G (VM5a) model reconstructions.

The primary models of the glaciation–deglaciation process that will be employed here for the purpose of analyzing the Earth's rotational response to the ice-age cycle are therefore ICE-5G (VM2) and the closely related ICE-6G (VM5a) models, the extension of which in the interval between the Eemian interglacial and LGM is based upon the SPECMAP record of Imbrie et al. (1984). In the inset to **Figure 9**, the complete ICE-6G record of the most recent glaciation–deglaciation cycle is compared with the reconstruction of Waelbroeck et al. (2002), whose reconstruction was based upon deep-sea δ^{18}O records

corrected for the influence of the temperature variability of the abyssal ocean. The comparison of this record with that for the ICE-6G (VM5a) model demonstrates that the two approximations to the ice-equivalent eustatic sea-level history over the most recent glaciation–deglaciation cycle are extremely similar. In order to construct a complete surface loading model for use in the computation of the Earth's rotation anomalies, however, a model that includes more than a single glacial cycle is required. Since approximately seven such cycles have occurred during the past 800 000 years of Earth history, for the purpose of the analyses to be discussed herein, it will be assumed that an ~100 ky periodic cycle of glaciation and deglaciation has continued to operate over this same period.

Construction of the polar wander and length-of-day solutions requires the time series $I_{13}^{\text{Rigid}}(t)$, $I_{23}^{\text{Rigid}}(t)$, and $I_{33}^{\text{Rigid}}(t)$, inputs to the calculation that may be computed from the definition of the I_{ij}^{Rigid}. This definition is

$$I_{ij}^{\text{Rigid}}(t) = \iint \nu(\theta, \phi, t)\left(a^2\delta_{ij} - x_i x_j\right) \mathrm{d}s \qquad [38]$$

where the integral is over the surface of the sphere and where $\nu(\theta, \phi, t)$ is the surface mass load per unit area. Since this may be expressed in the form of a spherical harmonic expansion as

$$\nu(\theta, \phi, t) = \sum_{\ell=o}^{\infty} \sum_{m=-\ell}^{+\ell} \nu_{\ell m}(t) Y_{\ell m}(\theta, \phi) \qquad [39]$$

it follows that

$$I_{13}^{\text{Rigid}}(t) + iI_{23}^{\text{Rigid}}(t) = -\left(\frac{32}{15}\right)^{1/2} \pi a^4 \nu_{21}(t) \qquad [40a]$$

$$I_{33}^{Rigid}(t) = -\left(\frac{8}{3}\right)\pi a^4 \left[\left(\frac{1}{5}\right)^{1/2} \nu_{20}(t) - 2\nu_{oo}(t)\right] \qquad [40b]$$

An issue that immediately arises concerning the evaluation of these inputs to the theory concerns the way in which the component of the surface load is computed that is associated with the water that is extracted from or added to the oceans as the ice sheets grow and decay, respectively. Although the loading and unloading of the continents due to the growth and decay of the ice sheets are an a priori-specified input to the theory, the ocean loading component must be obtained self-consistently as a solution to the SLE eqn [10]. However, this equation for the space–time history of the load on the ocean basins includes the influence of rotational feedback through the convolution of Ψ^R with ${}_R G_\phi^T$. The problem of determining the rotational response to the ice-age cycle must therefore be determined iteratively. We first compute a solution for the ω_i by neglecting this feedback effect. We next add the feedback terms into eqn [10] and recompute the sea-level history and thus the modification to the ocean load needed to determine the inertia perturbations required for the computation of the $\omega_i(t)$, etc. The iteration sequence is found to converge rapidly. It is also important to note that the ocean component of the surface load varies over a single glacial cycle in a way that depends somewhat upon the viscosity model of the Earth that is employed to represent the GIA process.

Figure 11 illustrates two example solutions for the time series of the Cartesian components of the angular velocity vector for two different combinations of ice-sheet loading history and mantle viscosity profile. In Figure 11(a), the time series are shown for models in which seven 100 ky cycles of glacial loading and unloading are assumed. The time series plotted are of $m_1(t) = \omega_1(t)/\Omega_o$ and $m_2(t) = \omega_2(t)/\Omega_o$ in which Ω_o, as before, is the angular velocity of Earth about its unperturbed axis of rotation. Notable is the fact that there exists a secular variation in each component upon which the impact of individual 100 000-year periodic ice-age cycles is superimposed. The model of glaciation and deglaciation for ICE-5G (VM2) is exactly that illustrated in Figure 5 of Peltier and Luthcke (2009). The second model is denoted ICE-6G (VM5aD1), the viscosity model of which, VM5aD1, is one of the soft D″ (VM5a) models described in Peltier and Drummond (2010), whereas the ice loading and unloading history is a slightly modified version of ICE-5G in which the only significant changes have involved the slight redistribution of mass

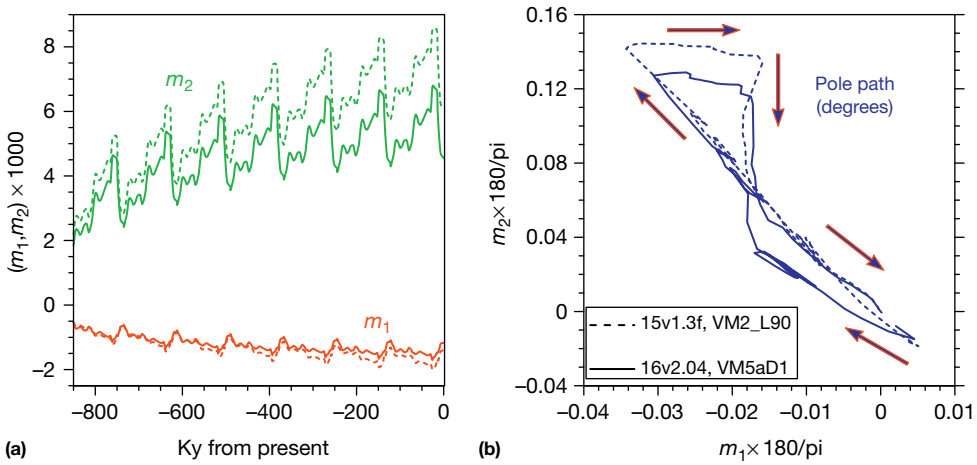

Figure 11 The reaction of the rotation pole in response to forcing by the 100 ky cycle of Late Pleistocene time. (a) The response of the pole in terms of the variables m_1 and m_2 for two different models of the inertia tensor variations for an assumed seven cycles of glacial loading and unloading. The two Earth models for which results are shown are ICE-5G (VM2) and ICE-6G (VM5a). (b) The actual pole paths for these two models are also shown in which the 'loops' associated with the two meltwater pulses are clearly evident.

over North America required to eliminate the misfits to the large database of GPS observations of vertical motion discussed in Argus and Peltier (2010) and a modification to the Antarctic component of the deglaciation history, which essentially eliminates mass loss from the interior of East Antarctica and moderately redistributes mass loss from West Antarctica (see Argus et al. (2014) and Peltier et al. (2014) for details). The secular component of the angular velocity time series arises because the surface mass load of ice on the continents, averaged in time, is nonzero. **Figure 11(b)** shows the polar wander path for the final cycle of loading and unloading for each of the example combinations of glaciation history and radial viscoelastic structure with the present day corresponding to the origin in the x–y plane. The 'loops' in the polar wander path are associated with meltwater pulses 1*A* and 1*B* that are clearly defined in the Barbados record of Peltier and Fairbanks (2006).

The time-domain form of the Liouville equation that connects these variations in the Cartesian components of the angular velocity vector of the planet to the corresponding elements of the products of inertia then states (e.g., Munk and MacDonald, 1960)

$$\frac{i\mathrm{d}\overline{m}/\mathrm{d}t}{\Omega\left(\frac{C-A}{A}\right)}+\overline{m}=\frac{1}{(C-A)}\left(\overline{I}-\frac{i\mathrm{d}\overline{I}/\mathrm{d}t}{\Omega}\right) \qquad [41]$$

In writing this equation, we have here employed the conventional complex variable-based definitions:

$$\begin{aligned}\overline{m}(t)&=m_x(t)+im_y(t)\\ \overline{I}(t)&=I_{xz}(t)+iI_{yz}(t)\end{aligned} \qquad [42]$$

In the low-frequency limit that is appropriate to understanding of the GIA process, eqn [35] reduces simply to the form

$$\overline{m}(t)=\frac{\overline{I}(t)}{(C-A)} \qquad [43]$$

In the expression for $\overline{I}$ in the preceding text, it is to be understood that this consists of two distinct parts, namely,

$$\overline{I}(t)=\overline{I}_{\mathrm{LOAD}}(t)+\overline{I}_{\mathrm{ROT}}(t) \qquad [44]$$

In **Figure 12**, we illustrate the variations of each of these contributions to the products of inertia that govern the polar wander effect for a single glacial cycle and the sum of these contributions according to eqn [38] along with a diagnostic constructed to test the accuracy of the mathematical methods employed to solve the low-frequency approximation to the Liouville equation [37]. The diagnostic is labeled 'ratio,' and the fact that it is unity demonstrates that the Liouville equation is being satisfied to high accuracy (see Peltier et al. (2012) for a detailed discussion). Given these models for a single ice-age cycle of the variation of I_{xz} and I_{yz} and a corresponding model for I_{zz} (see Peltier and Luthcke (2009) for an example of the latter), we are in a position to make detailed predictions of the time rate for change of the length of day and of polar wander speed and direction for a multicycle model of Late Quaternary glaciation and deglaciation, which we may compare to observations.

9.09.4 Observations of Millennial Scale Secular Variations in the Earth's Rotation Anomalies and the Impact of the Global Warming Era upon Them

Although the existence of a secular trend, persisting over thousands of years, in the nontidal variations of the l.o.d., has been known for at least the last quarter of the twentieth century and an equivalently important secular drift in the position of the pole has also become evident in the same period, debate has continued as to the cause of these secular variations in the Earth's rotation anomalies. Only through the development of the theory described in the last subsections of this chapter, however, has it proved possible to unambiguously attribute

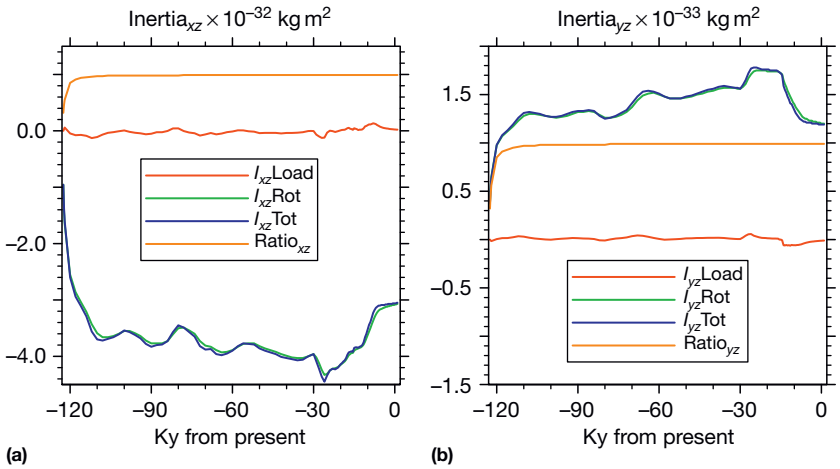

Figure 12 The primary components of the 'total' perturbations of the moment of inertia tensor that are responsible for driving the polar motion associated with the glaciation cycle shown in **Figure 11**. Also shown are the individual contributions to the total perturbation due to the surface mass 'load' and to the influence of rotational feedback, which is denoted 'rot.' The time series labeled ratio in each plate must equal unity if the combination of the time series of the inertia perturbations and the time series of variations in the components of the angular velocity satisfy the Liouville equation. The theory that has been developed to solve this equation is clearly highly accurate on this basis.

both signals to the GIA process. Prior to reviewing the analyses that have established this result, it will be useful to briefly review the observations themselves. As we will also demonstrate, these secular rates of change have themselves begun to deviate sharply from their previously stable rates over the past several decades. As we will argue, these sharp changes in the rates of secular variation are associated with the ongoing influence of the warming of the lower atmosphere that is due to the increasing concentration of carbon dioxide due to fossil fuel burning.

9.09.4.1 Ancient Eclipse Observations and the Nontidal Acceleration of Rotation

That an anomaly in Earth's rate of axial rotation did exist, beyond the relatively well-understood decrease due to the action of the tidal friction that arises because of the frictional dissipation of the tide raised in the Earth's oceans by (primarily) the gravitational attraction of the Moon, was first suggested (e.g., Morrison, 1973; Muller and Stephenson, 1975; Newton, 1972) on the basis of analyses of ancient eclipse data extending back more than 2500 years before present. For much of this interval of time, in both Babylon and China, naked-eye astronomers kept careful records of the timing and place of occurrence of total eclipses of the Sun and Moon. On the basis of the assumption that tidal friction had remained constant over this interval, a highly reasonable assumption as sea level has not changed appreciably over this Late Holocene period, one may accurately predict when and where a total eclipse of the Sun or Moon should have occurred. Analysis of such data, as described most recently in Stephenson and Morrison (1995) and Morrison and Stephenson (2001), clearly demonstrates that the further back in time for which an eclipse prediction is made, the larger is the error in timing, the sign of the error being such as to imply the action of a acceleration of rotation that is acting opposite to the effect of tidal friction. The compilation of data from the paper by Stephenson and Morrison (1995) is shown in **Figure 13**. Based upon the analysis of both lunar and solar eclipses that occurred between 700 BC and AD 1600, these authors reported an increase in the length of the mean solar day (l.o.d) of (1.7 ± 0.5) ms per year, which implies a rate of decrease of the angular speed of rotation of $(-4.5 \pm 0.1) \times 10^{-22}\,\mathrm{rad\,s^{-2}}$ on average over the past 2.7 ky. After subtracting the contribution due to tidal friction, which is accurately known based upon observations of the rate of recession of the Moon using Lunar Laser Ranging, Stephenson and Morrison (1995) inferred an average rate of nontidal acceleration of $(1.6 \pm 0.4) \times 10^{-22}\,\mathrm{rad\,s^{-2}}$ over this period. This value for the nontidal acceleration of rotation corresponds to a value for $\dot{J}_2$ of $(-3.5 \pm 0.8) \times 10^{-11}\,\mathrm{year^{-1}}$. As discussed in **Section 9.09.2**, this parameter provides a direct measure of the rate of change of the oblateness of planetary shape such that the larger J_2, the larger the oblateness or, equivalently, the polar moment of inertia. The fact that the time derivative is negative

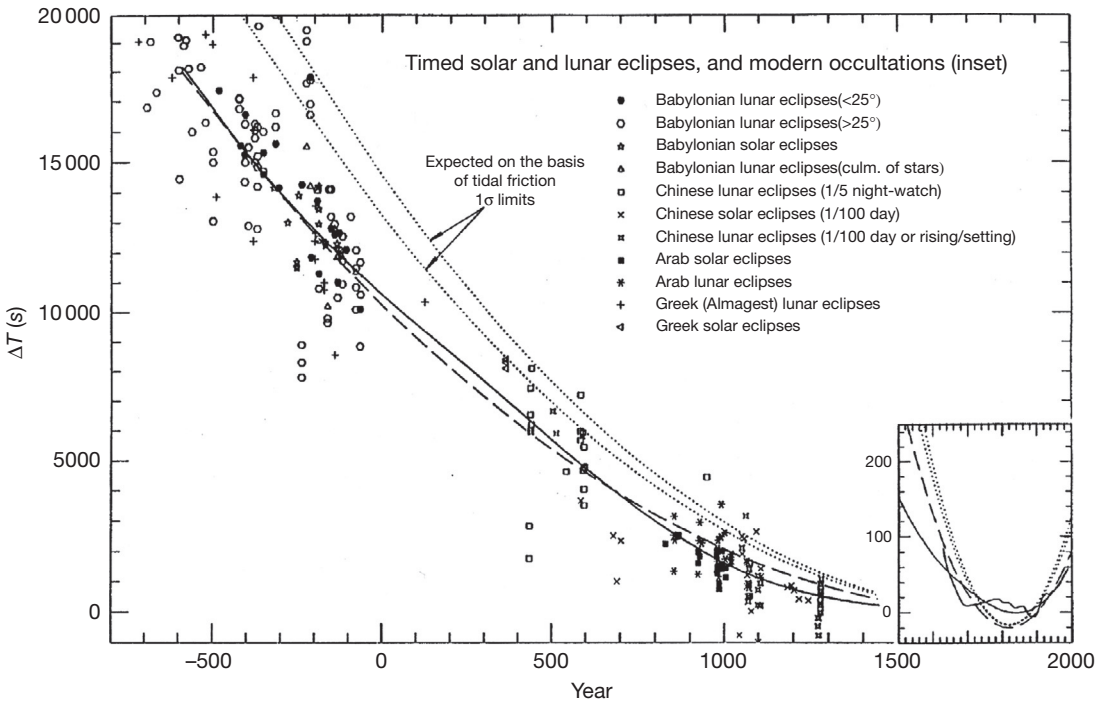

Figure 13 Results obtained for the time difference between the observed time of a total eclipse of the Sun or the Moon and the time at which the event was predicted to occur based upon the assumption of constant tidal torque. The inset (on a scale 25 times greater) includes the continuous curve derived from the lunar occultations in the period AD 1620–1955.5 and the difference TAI-UT1 + 32.1845 from 1955.5 to 1990. The dashed curve is the best fitting parabola $31t^2s$. The solid curve is fitted using cubic splines. This curve, the best fitting parabola, and the parabola expected on the basis of tidal friction are continued on the inset. Reproduced from Stephenson ER and Morrison LV (1995) Long term fluctuations in the earth's rotation: 700 B.C. to A.D. 1990. *Philosophical Transactions of the Royal Society of London, Series A: Mathematical, Physical and Engineering Sciences A* 351: 165–202.

therefore implies that the nontidal acceleration of rotation is derivative of a secular decrease in the oblateness of figure and therefore of a decrease in the value of the polar moment of inertia. That this is plausibly a consequence of the GIA process follows from the fact that at glacial maximum, the oblateness would have been increased by the increased surface mass load at the poles. Once this load is eliminated during the deglaciation process, this ice-age contribution to enhanced oblateness would have begun to relax viscoelastically as the planet returned to the more spherical shape characteristic of an interglacial period. Since angular momentum is conserved in the absence of external torques, the rate of axial rotation would have continued to increase thus leading to the observed nontidal *acceleration* of rotation.

Beginning with the first publication and interpretation of data from the Laser Geodynamics Satellite (LAGEOS) by Yoder et al. (1983), which appeared simultaneously with the interpretation of the nontidal acceleration as a consequence of the GIA effect (Peltier, 1982, 1983), the validity of the ancient eclipse-based inference of the nontidal acceleration was clearly established. Many estimates of the nontidal acceleration based upon the analysis of SLR data have now appeared (the effect observed is an acceleration in the rate of precession of the node of the orbit of the satellite). A relatively complete set of published estimates up to 1991 is shown in **Figure 14** where the estimates of various authors are provided in terms of $\dot{J}_2$. As will become clear in what follows, my reason for truncating the list of available estimates at 1991 has to do with the fact that subsequent to this time, a pronounced shift in the value of this parameter has become evident.

As a final comment upon the most recent research that has been conducted on l.o.d changes on millennial timescale, it is worth noting the work of Dunberry and Bloxham (2006) on the possibility of the existence of an oscillation in the l.o.d. that may be evident in the historical eclipse data set, an oscillation that the authors suggest may have a period of 1500 years. A similar timescale is suggested to be evident from archaeomagnetic artifacts, lake sediments, and lava flows (Daly and Le Goff, 1996; Hongre et al., 1998; Korte and Constable, 2003). They interpret this as plausibly arising as a consequence of coupling between the outer core and the mantle across the core–mantle interface. It should be noted, however, that the existence of any such 1500-year oscillatory component in the l.o.d. variations has been questioned by Dalmau (1997).

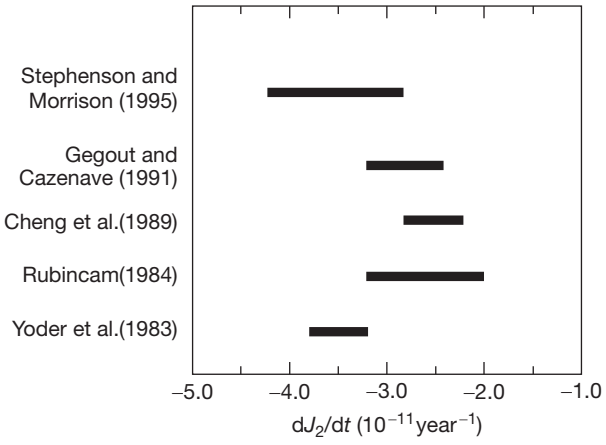

Figure 14 Published estimates of the parameter $\dot{J}_2$.

9.09.4.2 Millenial Timescale Polar Wander and the Glaciation–Deglaciation Cycle

Insofar as the second of the secular anomalies in the Earth's rotation is concerned, namely, the true wander of the north pole of rotation relative to the surface geography, the data originally obtained by the International Latitude Service that have been employed to constrain it are shown in **Figure 15**. The data initially tabulated by Vincente and Yumi (1969, 1970) were derived on the basis of observations of star transits using a northern-hemisphere array of photo-zenith tubes. The data consist of time series of the x and y coordinates of the position of the north pole of rotation relative to a reference frame fixed to the Earth's crust with origin at the CIO. This reference frame is shown in the inset polar projection in **Figure 15** and has its x-axis aligned with the Greenwich meridian. Inspection of the x and y time series demonstrates them to be dominated by an oscillatory pattern of beats with a period of $\sim$7 years. This pattern is well understood to arise as a consequence of the interference between the 12-month periodic annual wobble and the $\sim$14-month periodic Chandler wobble that were discussed in **Section 9.09.2** of this chapter. Based upon the review of our understanding of these features of the Earth's rotational history discussed therein, it would appear that previous controversies concerning their excitation have now been satisfactorily resolved. According to Dickman (1977), the true polar wander (TPW) evident as the secular drift of the position of the pole upon which the oscillatory signal is superimposed was occurring at a rate of $(0.95 \pm 0.15)^\circ\,\mathrm{My}^{-1}$ along the 75.5° W meridian over this time period as shown in the inset polar projection in **Figure 15**. An unambiguous connection of this anomaly of the Earth's rotation to the GIA process was first suggested in Peltier (1982) and Wu and Peltier (1984), whose detailed theoretical analysis, since further generalized in Peltier and Jiang (1996), showed that the initial analysis by Munk and MacDonald (1960) of the excitation of polar wander by surface loading of a viscoelastic model of the Earth did not in fact rule out an explanation in terms of the GIA process even though the surface mass load during the Late Holocene interglacial period has been very nearly time-invariant. The analysis of the data by Dickman (1977) was preceded by several earlier analyses and has been followed by others. Most of these results are shown in **Figure 16** where they are accompanied by an early result derived on the basis of the analysis of VLBI observations by Carter et al. (1986).

The most recent analysis of the ILS data is that of Argus and Gross (2004), who have investigated the possibility that all of these interpretations may be contaminated by the failure to account for the influence of surface plate tectonic motions. Their analysis of the raw data delivered the best estimate of the speed of polar wander of $1.06^\circ\,\mathrm{My}^{-1}$. Depending upon how this estimate was corrected for the influence of plate tectonics, however, considerably different results could be obtained, as listed on **Table 1** of that paper. Whereas the ILS inference uncorrected for plate motion was that the ongoing polar wander was along the 75.5° W meridian, if the same data set is corrected by making the inference in the frame of

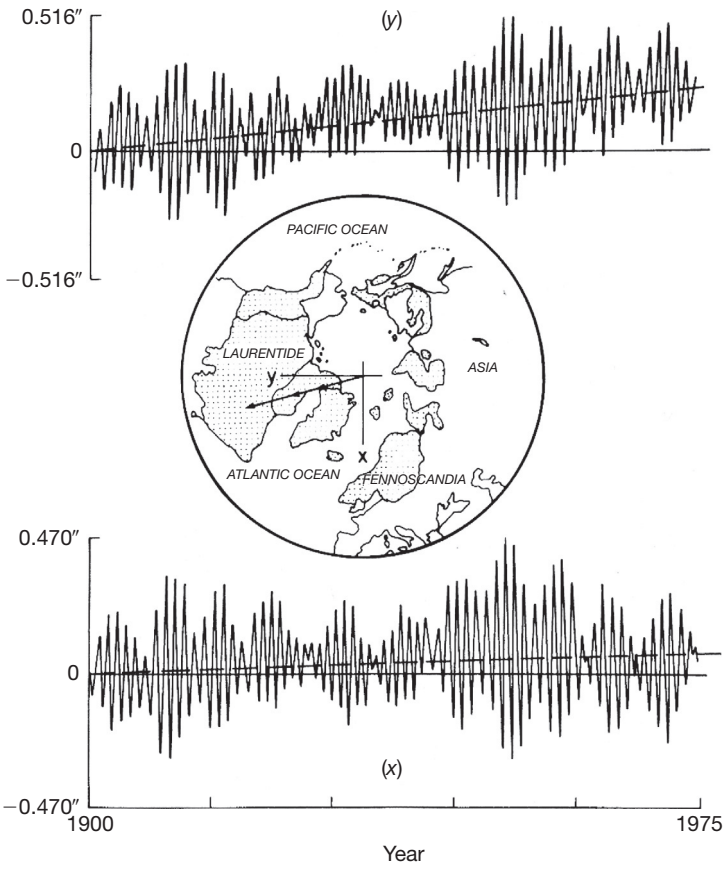

Figure 15 Time series of the location of the north pole of rotation of the planet, as x and y coordinates relative to the coordinate system shown in the inset polar projection with origin at the Conventional International Origin (CIO). These data are those of the International Latitude Service (Vincente and Yumi, 1969, 1970), and they reveal a secular drift of the pole at a rate near 0.95° My^{-1} approximately along the 75.5° W meridian of longitude.

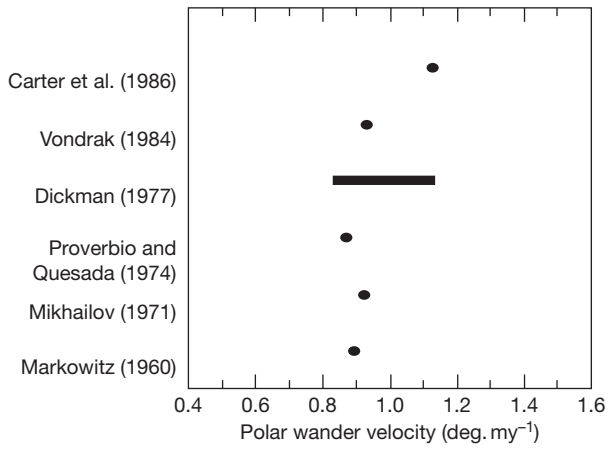

Figure 16 Published estimates of the speed of polar motion based primarily upon the ILS data.

reference in which the lithosphere exhibits no net rotation, then the corresponding speed and direction change slightly to 0.98° My^{-1} southward along the 79.9° W meridian. However, if the correction to these data is based upon the 'hot spot frame,' then one obtains, from the ILS data, according to Argus and Gross (2004), the values 1.12° My^{-1} for the speed and southward along the 69° W meridian for the direction, a significant difference. The fact that all of these inferences of polar wander direction suggest it to be moving 'towards' what was the centroid of the ancient Laurentide ice sheet (see Figure 7) is nevertheless highly significant insofar as the explanation in terms of glacial isostasy is concerned. Since the constraint of angular momentum conservation requires that the pole must drift so as to align itself along the axis relative to which the moment of inertia is largest, it is clear why, as a consequence of the GIA effect, the pole should now be moving towards what was the centroid of the greatest concentration of land ice. Following deglaciation, there exists a residual depression of the land that has yet to be eliminated by the slow viscous process of GIA. This region therefore constitutes a localized deficit of mass relative to the state of gravitational equilibrium that will eventually be reached once the GIA-related relaxation of shape has been completed. It is towards this regional mass deficit that the pole must move in order to come into alignment with the axis of greatest inertia. That it never reaches and in general will not reach this region is simply a consequence of the fact that the speed of polar wander decreases as a function of time as the shape relaxation proceeds at a rate determined by mantle viscosity.

Table 1 Interstudy comparison of secular trends in polar wander and $\dot{J}_2$

Source	*Fits*	*Time covered*	*Polar motion (mas year^{-1})*	*Direction*
Polar wander				
Argus and Gross (2004) (ILS) (relative to mean lithosphere)	1	1899–1979	3.53	79.9° W
Gross and Vondrák (1999) (HIPPARCOS)	1	1900–1992	3.51	79.2° W
Gross and Vondrák (1999) (SPACE96)[a]	1	1976–1997	4.12	73.9° W
Gross and Poutanen (2009) (SPACE2007)[a]	2	1976–1995	4.23	72.2° W
		1995–2007	2.92	64.8° W
This study (SPACE2008)	2	1976–1992	4.5(±0.1)	68(±8)° W
		1992–2008	1.8(±0.4)	58(±9)° W

Source	*Fits*	*Time covered*	$\dot{J}_2$ ($\times 10^{-11}$ year^{-1})
$\dot{J}_2$			
Yoder et al. (1983)	1	1978–1983	−3.5
Stephenson and Morrison (1995)	1	700 BC–AD 1600	−3.5
Cheng and Tapley (2004)	1	1976–2004	−2.75
This study	2	1976–1992	−3.7 (±0.1)
		1992–2009	−0.9 (±0.2)

[a]SPACE2007 and SPACE96 are two earlier versions of the SPACE2008 Earth Orientation Parameters-based data series for polar motion.

Reproduced from Roy K and Peltier WR (2011) GRACE era secular trends in Earth rotation parameters: A global scale impact of the global warming process? *Geophysical Research Letters* 38: L10306, http://dx.doi.org/10.1029/2011GL047282.2011.

The question of the accuracy of the direction of the secular drift of the pole that is derived on the basis of the ILS data may be at least as important as the speed. The reason for this has to do with the use of the rotational anomalies to constrain the rate of melting of land ice that may be occurring at present due to the action of greenhouse gas-induced global warming. Depending upon the polar wander prediction due to the continuing action of the GIA effect, there will exist a residual between this prediction and the modern observations that may be employed to constrain the rate and geographic locations of modern sources of land-ice melting (Greenland, Antarctica, small ice sheets and glaciers, see Dyurgerov and Meier (2005)) as previously discussed in Peltier (e.g., 1998, see Figure 46 of that paper). Further comment on this issue will follow in the next section of this chapter in which the theory reviewed in **Section 9.09.3** will be applied to understanding the observational constraints upon pre-1990s polar wander described in this section. First, however, we will show here that a very substantial shift in the trends of both rotational anomalies has occurred over the past several decades.

9.09.4.3 Global Warming Era Shifts in the Millennial Timescale Trends in the Earth's Rotation Anomalies Based upon Modern Earth Orientation Data Sets

Modern trends in the polar wander signal have been examined using a recent set of independent space-geodetic Earth orientation measurements, which are generated annually by the Jet Propulsion Laboratory (JPL). The particular set analyzed in the recent paper by Roy and Peltier (2011), known as SPACE2008, was made available from JPL's Geodynamics and Space Geodesy Group via anonymous ftp at <ftp://euler.jpl.nasa.gov/keof/combinations/2008> and spanned the period from 28 September 1976 to 2 July 2009. It includes the values of the polar motion components at daily intervals, with components extending from the CIO along an x-axis aligned with the Greenwich meridian and along a y-axis aligned with the 90° W meridian (Ratcliff and Gross, 2010). As discussed earlier, polar motion is dominated by large high-frequency variations, and in order to study the linear trends in the series influenced by the process of GIA, it is imperative to remove those signals. In Roy and Peltier (2011), a Butterworth-type low-pass filter was applied to the polar motion series (Butterworth, 1930), with a period cutoff set at 6 years, a value that is consistent with previous studies of polar motion trends (Gross and Vondrák, 1999). The Butterworth filter is preferred to simpler, idealized digital filters such as the simple boxcar filter, as it has a maximally flat frequency response and phase shift effects that are simple to compensate. The smoothed series, shown in **Figure 17(a)** and **17(c)** (for the x- and y-components, respectively), served as the basis for the analysis in Roy and Peltier (2011) of quasiperiodic low-frequency residual variability, using a methodology similar to that employed in Gross and Vondrák (1999). Low-frequency and quasiperiodic terms were determined by performing a simultaneous weighted least-squares fit for a mean, a linear trend, and low-frequency periodic terms that correspond to the most prominent peaks in the amplitude spectrum of the time series. Changes in the linear trend were isolated by separating the time series into two subsets. The position of the 'pivot time' that separates the two adjacent periods of best fit was allowed to vary, and the linear trend and mean were adjusted as this 'knot' was shifted in time in order to find the pivot time that minimizes the overall root-mean-square error of the two-segment fit. This new fit is then compared with the best overall fit with a single linear trend and must be characterized by a substantially lower root-mean-square error of fit to be considered plausible physically. The resulting two-segment fits are presented in **Figure 17(b)** and **17(d)** for both the x- and y-components, respectively, and are listed in **Table 1**.

Recent variations in the linear trends for the nontidal acceleration of planetary rotation rate are studied using the most recently available satellite laser ranging (SLR) data for a subset of eight geodetic satellites (Starlette, Ajisai, Stella, LAGEOS 1 and 2,

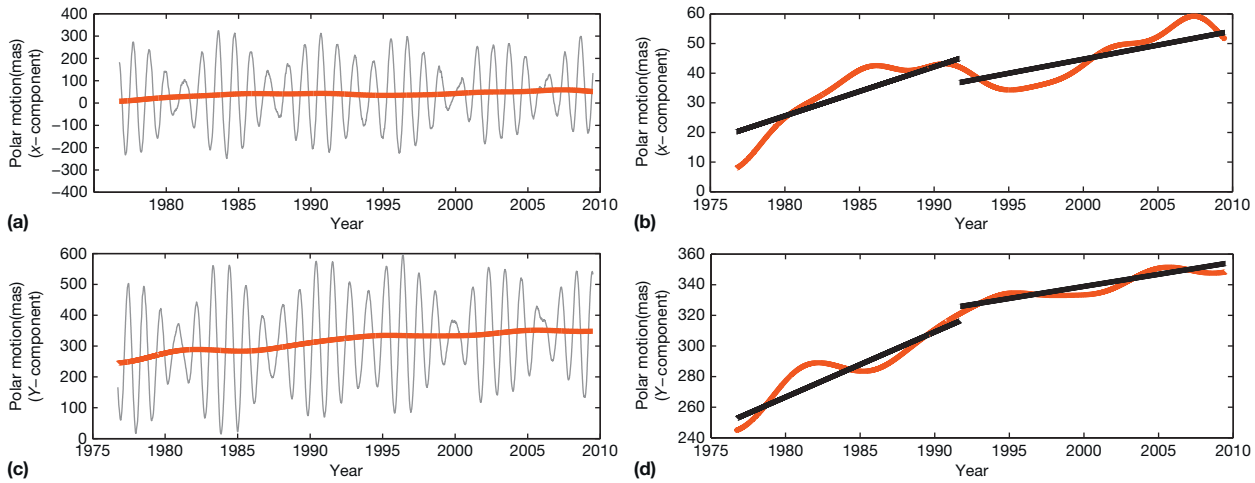

Figure 17 (a) and (b) show the *x*- and *y*-components of the polar motion for the period ~1975–2010 based upon the Earth orientation data set discussed in the text. (c) and (d) show both the Butterworth low-pass filtered versions of the time series in (a) and (b) together with two-segment linear fits designed to optimally reduce the RMS misfit of the secular rate(s) of change compared with that determined by a single-segment fit. The key result, which is from the paper by Roy and Peltier (2011), is that a marked shift in the secular rate of change occurred in the early 1990s.

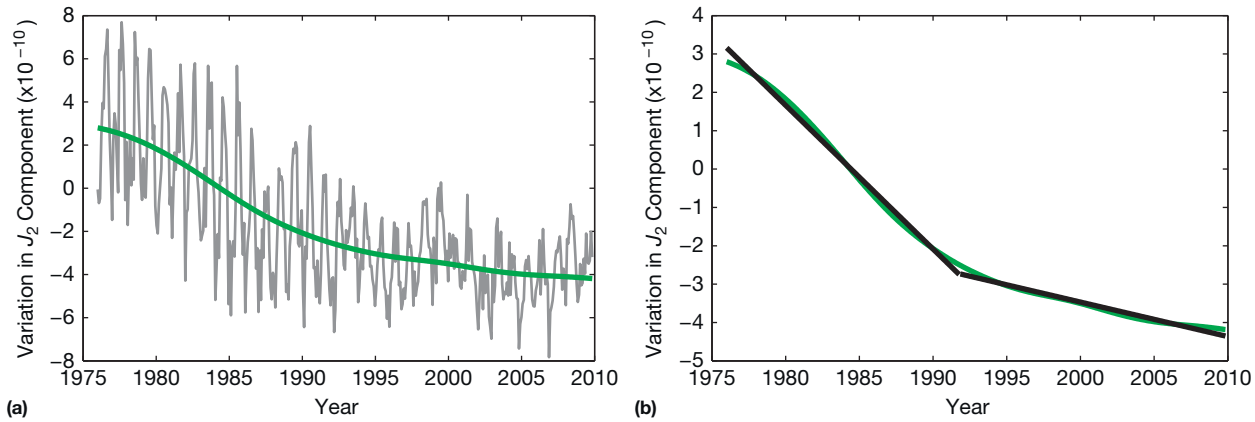

Figure 18 The results of a similar analysis to that shown in **Figure 17** but here for the time series of J_2. (a) shows the raw time series data and the Butterworth low-pass filtered version, while (b) shows the two-segment fit to the low-pass filtered time series in (a), which once more establishes the timing of the apparent shift in the secular variation of the time series as having occurred in the early 1990s. This result is again from Roy and Peltier (2011).

Etalon-1 and Etalon-2, and BE-C (from 1999 onward)) (Cheng and Tapley, 2004; Tapley et al., 2004). The available data, obtained originally via anonymous ftp at <ftp://ftp.csr.utexas.edu/outgoing/cheng/j2.76010911>, span January 1976 to the end of 2009 and are presented in **Figure 18(a)**, also from the study of Roy and Peltier, 2011. In order to study variations in the linear trend over this period, low-frequency terms are also eliminated using a low-pass Butterworth filter. The cutoff in this case was fixed at 20 years, which is sufficient to remove suggested 18.6-year tidal and decadal variations and is consistent with the analysis of Cheng and Tapley (2004). The smoothed series, plotted in **Figure 18(a)**, reveals a marked change in approximately the mid-1990s. Linear trends were then determined in the smoothed J_2 series, by separating the data series into two segments and fitting the trend separately for each part, as for the polar motion. The pivot time was again shifted in time to find the position of the 'knot' in time that minimizes the overall root-mean-square error of fit, the final result of which is presented in **Figure 18(b)**.

Changes in the recent linear trends for the secular drift of the position of the pole relative to the surface geography and the nontidal acceleration of the rate of planetary rotation have been independently revealed to exist through these analyses. However, it is most instructive to compare the variation of the total root-mean-square error for the two rotation-related time series as the position of the transition in the linear trend is allowed to vary. These results, which are presented in **Figure 19**, show that the transition in the linear trends for both anomalies occurs near 1992.

As shown in **Table 1**, this study of the observations of the polar motion time series suggests that its rate remained approximately fixed, prior to 1992, at $4.5(\pm 0.1)$ mas year^{-1} ($1.3°\,\mathrm{My}^{-1}$), along the $68(\pm 8)°$W meridian, while it slows to $1.8(\pm 0.4)$ mas year^{-1} ($0.5°\,\mathrm{My}^{-1}$) after 1992, along the $58(\pm 9)°$W meridian. Although not corrected for plate tectonics, as in Argus and Gross (2004), the Roy and Peltier (2011) analysis demonstrates that dividing the time series into two distinct epochs increases the magnitude of the established

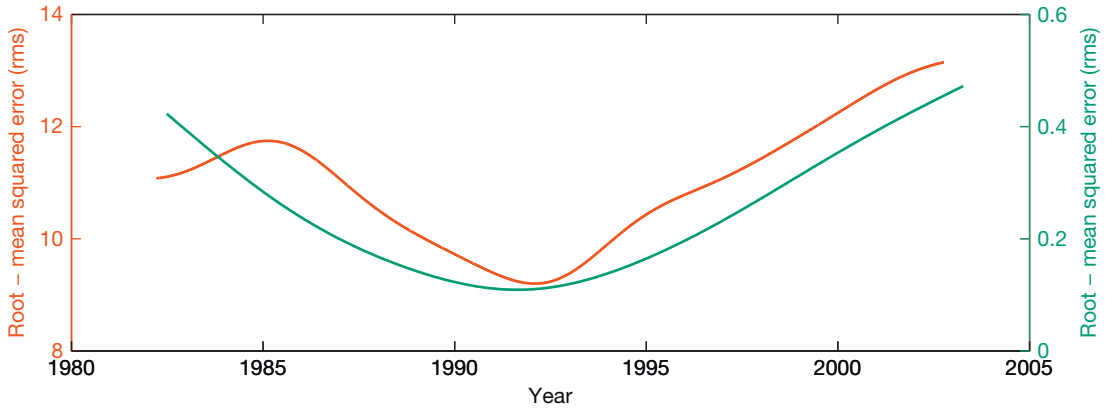

Figure 19 The RMS misfit of the two-linear-segment fits relative to that of a single-segment fit for both the polar motion and length-of-day related observables as a function of the time selected for the pivot point in time at which the secular variation is assumed to change. The minimum in the misfit for both time series is thereby shown to occur in ~1992, a full decade prior to the launch of the GRACE satellites.

secular rates of change prior to 1992, but decreases them for modern times subsequent to this. With regard to changes in the J_2 component, the Roy–Peltier analyses suggest a rate of change of $-3.7(\pm0.1)\times10^{-11}$ year^{-1} before 1992 and $-0.9(\pm0.2)\times10^{-11}$ year^{-1} after 1992. Dividing the data series into two parts is very significant, because it better reconciles the observed rate of change for J_2 presented in Cheng and Tapley (2004) with the estimate from historical records of Stephenson and Morrison (1995) ($-3.5(\pm0.8)\times10^{-11}$ year^{-1}).

The inference of a notable change in the linear trends for both anomalies is highly significant, as both the variation in J_2 and the polar wander data are dependent on completely independent elements of the Earth's moment of inertia tensor (e.g., Peltier and Luthcke, 2009). Models of the GIA process, in which the moment of inertia tensor of the planet is determined by a specific model of the time-dependent continental ice-sheet loading and of the depth dependence of mantle viscosity, are able to fit simultaneously those two rotational anomalies with great success, which suggests that it would be very surprising if the observed change in the linear trends inferred to have occurred since 1992 was not caused by recent changes in the surface ice-sheet loading on the planet.

The existence of a link between the timing of the changes in the linear trends for the rotational state anomalies and recent changes in the ice-sheet loading on the planet is supported by studies of the year-to-year melting rates in major continental ice sheets around the world. Thomas et al. (2006), for example, compared various diverging estimates of elevation changes and mass balance for the Greenland ice sheet and suggested that satellite altimetry measurements might seriously underestimate Greenland ice losses. If that were the case, all other indicators, such as snow-accumulation rates and airborne laser altimetry measurements, support the idea of a sharp decrease in ice-sheet mass starting in the mid-1990s.

9.09.5 Earth's Rotational Response to the Cyclic Glaciation Cycle of Late Pleistocene Time: Data–Model Comparisons

Based upon the discussion in Section 9.09.3 of this chapter, it will be clear that accurate predictions of relative sea-level history are a required preliminary to accurate predictions of the rotational response to the GIA process and thus to the understanding of the Earth's rotation history on millennial timescales. Since the best test of the accuracy of relative sea-level history predictions based upon solution of the SLE is provided by radiocarbon-dated relative sea-level curves from coastal locations, it will be clear that the confrontation of theory with observational 'truth' requires a voluminous compilation of such records, individual examples of which have been produced by innumerable scientists working in the area of Pleistocene geomorphology over the past half century. That a global database of such records is expected to record a wide range of signatures of the GIA process will be clear on the basis of Figure 20, which shows predictions of the present-day rate of relative sea-level rise for the ICE-6G (VM5a) model both including Figure 20(a) and excluding 20(b) the influence of rotational feedback. The difference between these predictions (Figure 20(a) and 20(b)) is shown in Figure 20(c), which establishes the dominant role that the polar wander component of the rotational response to the GIA effect plays in contributing to sea-level history. The 'signature' of this feedback is the existence of the strong degree 2 and order 1 spherical harmonic component, a quadrupolar distribution that is the expected form of this feedback based upon eqns [13] in Section 9.09.3. Figure 20(d) shows the sum of the signal shown in Figure 20(a) for the present-day rate of relative sea-level rise and the prediction for the same model of the present-day rate of radial displacement of the crust. As first discussed in Peltier (1999), this sum represents the time rate of change of geoid height due to the GIA process, an approximation to which is being measured by the Gravity Recovery and Climate Experiment (GRACE) dual-satellite system (see Figure 21) that is now in space. The reason why GRACE is able to observe only an approximation to the actual sea level-defined geoid has been discussed in detail in the recent paper of Peltier et al. (2012). In order to test the accuracy of predictions of the Earth's rotational response to the GIA process produced by the theory discussed in Section 9.09.4, an appropriate strategy is therefore to focus upon the observational constraints provided by geologic recordings of postglacial relative sea-level change through the Holocene interval of time in those regions in which the impact of rotational feedback is expected to be most intense.

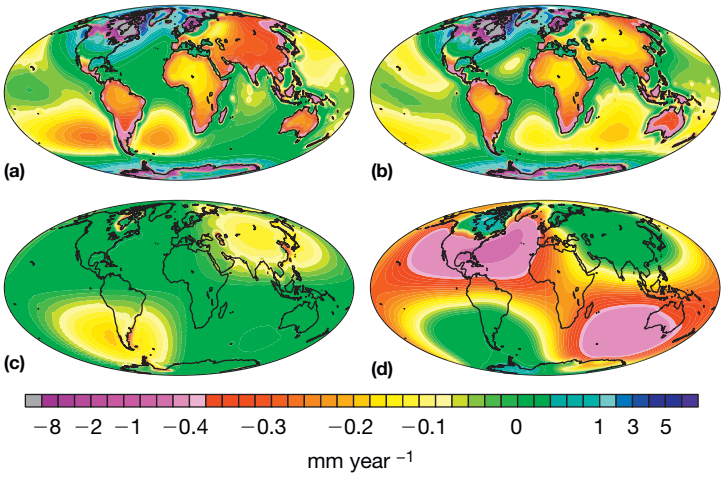

Figure 20 (a) The ICE-6G (VM5a) model prediction of (a) the present-day rate of sea-level rise relative to the deforming surface of the solid Earth, including the influence of rotational feedback; (b) same as (a) but excluding the influence of rotational feedback; (c) the difference between (a) and (b) illustrating the spherical harmonic degree 2 and order 1 pattern that dominates the influence due to rotational feedback on account of the control exerted by the polar wander effect; (d) the present-day geoid height time dependence predicted by the ICE-6G (VM5a) model, obtained by adding to the field in (a) the prediction of the time rate of change of radial displacement of the surface of the solid Earth with respect to the center of mass of the planet.

9.09.5.1 A Database of Holocene Relative Sea-Level Histories

A location map of the positions on Earth's surface from which ^{14}C-dated relative sea-level histories are available in the University of Toronto database is shown in **Figure 22** (from Peltier (1998)). Comparing the coverage provided by these many hundreds of individual RSL curves with the geographically intricate pattern evident in **Figure 20**, it will be clear that there exists, not surprisingly, much better coverage of this signature of the GIA process in the northern hemisphere than is available from the southern hemisphere. Yet, as will be made clear in what follows, the role of the available southern hemisphere data in confirming the important role that variations in the Earth's rotation play in forming the detailed signature of the GIA effect evident in Holocene RSL records is extremely important. **Figure 23** compares a number of ^{14}C-dated RSL records from this database with the predictions of the ICE-5G (VM2) and ICE-6G (VM5a) models that served as the basis for the computation of the time series of the variations in the elements of the moment of inertia tensor that are required in the computation of the rotational response to the glaciation–deglaciation cycle. The locations of the individual sites are shown in the map of the prediction of the present-day rate of sea-level rise predicted by the ICE-6G (VM5a) model of the GIA process that forms the central portion of **Figure 23**. Inspection of this initial set of comparisons will show that the theoretical structure developed to explain such widely varying histories of postglacial sea-level change is able to capture the details of this variability in a highly accurate fashion.

9.09.5.2 The Influence of Rotational Feedback upon Postglacial Relative Sea-Level History and Its Impact upon Predictions of the Earth's Rotation Anomalies

Although the purpose of this subsection of this chapter will be to explore the extent to which the most recent models of the GIA process may be employed to further reinforce the interpretation of the millennial timescale variations in the Earth's rotation anomalies in terms of the GIA process, it will be useful to begin by revisiting the results previously obtained by Peltier and Jiang (1996) who employed the ICE-4G deglaciation model of Peltier (1994, 1996b) to investigate the extent to which both of the previously discussed anomalies were explicable in these terms. Their results are summarized in **Figure 24** (reproduced from their paper), which shows, respectively, in **Figure 24(a)** and **24(b)** the theoretical predictions of $\dot{J}_2$ and polar wander speed as a function of the viscosity of the lower mantle of the Earth below a depth of 660 km, with the value of the viscosity of the upper mantle fixed to the nominally accurate value of 10^{21} Pa s, and the thickness of the surface lithosphere taken to be $L = 120$ km. Inspection of this Figure demonstrates that both of the millennial timescale secular anomalies are fit by the same simple model of the radial variation of mantle viscosity. With the upper-mantle viscosity fixed to the aforementioned value, the lower-mantle viscosity required to fit the observations is $\sim 2 \times 10^{21}$ Pa s. It might be seen as unlikely, given that the two rotational anomalies depend upon entirely independent elements of the moment of inertia tensor that this degree of agreement would exist if GIA were not the primary explanation for both observations.

It is extremely important, however, that we demonstrate that this result is robust against explicit incorporation of the difference between k_f and $k_2^T(s=0)$ as previously discussed in **Section 9.09.3**. This issue is explored in detail via **Figure 25**, which is from the recent paper of Peltier and Luthcke (2009), and in greater detail in **Figure 26**, also reproduced from their paper. These analyses are based upon the use of the ICE-5G loading history with seven cycles of glaciation and deglaciation included in the calculation. **Figure 25** may be compared directly with **Figure 24** and is shown to quite accurately reproduce that result for polar wander speed in the case in which the parameter $\Delta = 0$, which represents the EQM case in which

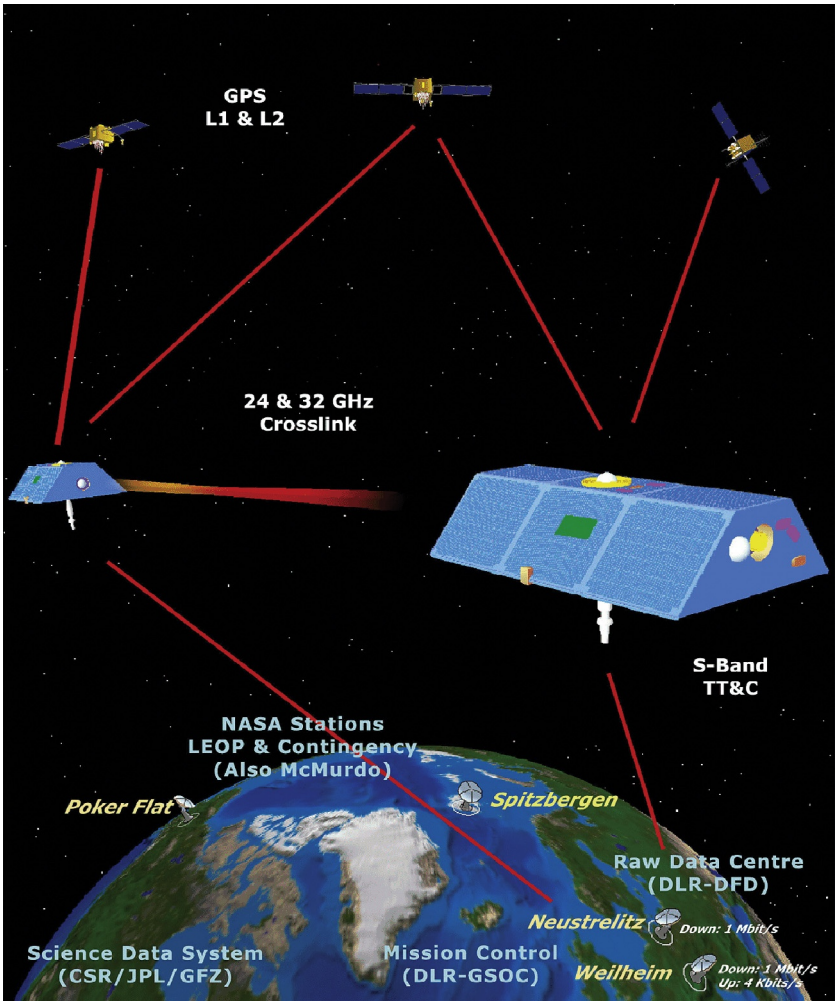

Figure 21 Schematic of the dual-satellite Gravity Recovery and Climate Experiment (GRACE) satellite experiment designed to measure the time dependence of the gravitational field of the planet. It is important to keep in mind that questions remain concerning the accuracy with which this system is able to directly measure the time-dependent amplitudes of the Stokes coefficients of degree 2 and order 1. These are most accurately obtained on the basis of the polar wander measurements of Roy and Peltier (2011) using the theoretical connections between these data and the crucial Stokes coefficients.

$k_f = k_2^T(s=0)$. On this figure, the phrase 'with rotation' is employed to represent the fact that the full impact of the change in ocean loading due to the changing rotation of the Earth is taken into account in the calculation. The case $\Delta = 1$ corresponds to the case in which not only is k_f different from $k_2^T(s=0)$ but also the elastic lithospheric thickness in the limit of infinite time is taken to be equal to 90 km, the same thickness as is approximately characteristic for short timescale continental ice-sheet cycle loading events. The two additional cases for which results are shown in the figure for polar wander speed correspond to cases in which the thickness of the lithosphere is taken to vanish in the infinite time limit but in which either one of the two plausible values of k_f shown in Figure 6 is assumed so that there continues to exist a difference between k_f and $k_2^T(s=0)$. Inspection of this figure demonstrates that the assumption of a finite value of lithospheric thickness in the infinite time limit leads to the failure of the model to simultaneously explain both of the pre-1992 values of the rotational anomalies. However, when the lithospheric thickness is assumed to vanish in the limit of infinite time, then, even when the difference between k_f and $k_2(s=0)$ is taken fully into account, the model still reasonably explains both data simultaneously.

In Figure 26, the robustness of the results shown in Figure 25 is explored by investigation of the sensitivity of the polar wander speed analyses to variations in the assumed value of the viscosity of the upper mantle and transition zone viscosity and to variations in the accuracy with which the representation of the ocean component of the surface mass loading cycle is included. Since the latest inferences of the mean viscosity of the upper mantle and transition zone fix this parameter to a value close to 0.4×10^{21} Pa s, the analyses demonstrate that this shift in value from the previously assumed value of 10^{21} Pa s has only a minor effect. However, the figure also suggests that it is important that the full influence of rotational feedback on the redistribution of mass in the global ocean is accurately calculated.

Since the aforementioned publication described two-layer viscosity model results of Peltier and Jiang (1996) and Peltier

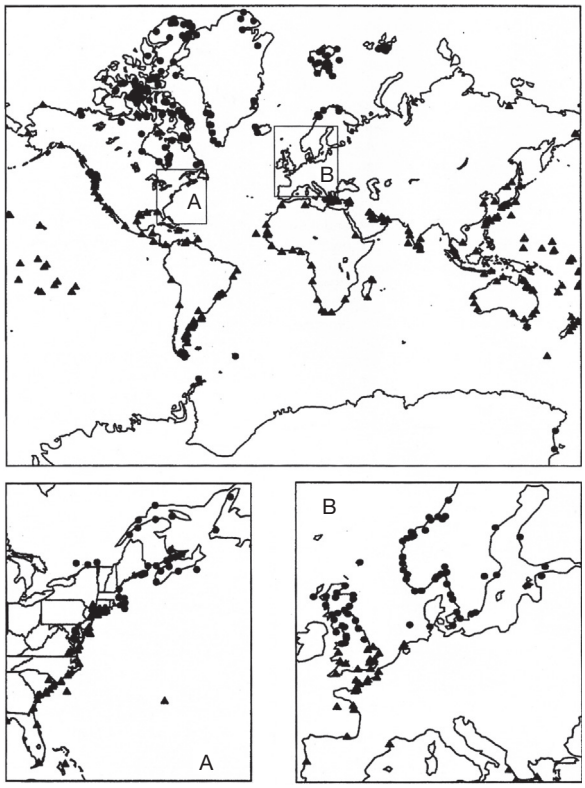

Figure 22 Global location map of the sites from which ^{14}C-dated time series of relative sea-level history are available in the University of Toronto database.

and Luthcke (2009), further refinements of the required analyses have been performed. In particular, in Peltier (1996b), the VM2 model of the radial viscosity structure was inferred on the basis of a full Bayesian inversion of the available data (see Figure 27). Equally important has been the considerable further refinement of the loading history that is represented by the ICE-5G model of Peltier (2004) and previously introduced in Section 9.09.3 of this chapter and the even more recent model ICE-6G (VM5a). The first row of Table 2 lists the predictions of present-day polar wander speed and direction and $\dot{J}_2$ for the ICE-6G (VM5aD1) model, assuming the validity of this model of the radial viscosity structure discussed in Peltier and Drummond (2010), which is a relatively minor variant upon the VM5a structure that includes a slight softening of the viscosity of the D″ layer above the core–mantle boundary. Model VM5a is itself a simple multilayer fit to VM2, but one that allows for viscosity stratification of the lower lithosphere. These analyses include the full influence of rotational feedback as discussed in Peltier et al. (2012) and demonstrate that the model well fits the pre-1992 values of all three of the rotational anomalies. The additional columns of Table 2 contain values of the degree 2 and order 1 Stokes coefficients in the spherical harmonic expansion of the time dependence of geoid height, a field that has been measured approximately by the GRACE satellite system that has been in space only since March of 2002 and therefore could not provide measurements of these parameters in the pre-1992 period subsequent to which a marked change in the Earth's rotation anomalies took place.

In the second row of Table 2, predictions of the same Earth's rotation observables for a model labeled 'A' are shown

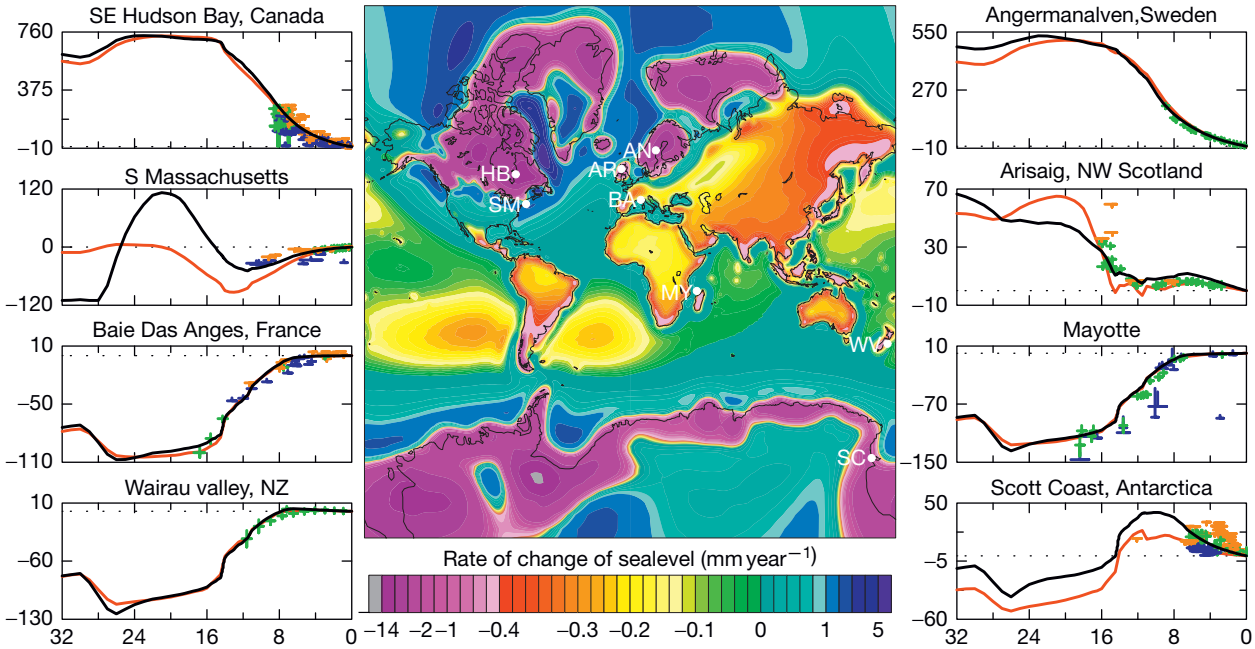

Figure 23 Illustrative suite of predictions of the history of relative sea-level change at eight sample locations using the ICE-5G(VM2) model of the global GIA process. The locations of the individual sites are superimposed upon a Mercator projection of the predicted present-day rate of relative sea-level rise. Predictions are shown for two slightly different versions of the model that differ from one another only in terms of the assumption made concerning the timing of Last Glacial Maximum. For one version of the model, LGM is assumed to have occurred at the conventional age of 21 ka; for the other, it is assumed, as illustrated in Figure 8, that LGM occurred considerably earlier at 26 ka as suggested on the basis of the Barbados data discussed in Peltier and Fairbanks (2006). The results for the ICE-6G (VM5a) model at these sites are very similar.

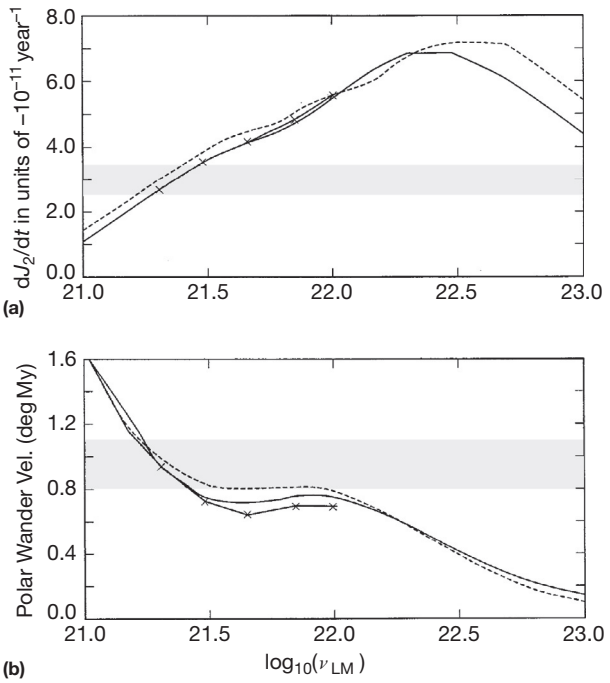

Figure 24 (a) $\dot{J}_2$ as a function of lower-mantle viscosity with the upper-mantle viscosity held fixed to the value of 10^{21} Pa s. (b) Same as (a) but for polar wander speed. In each frame, the hatched region represents the observationally constrained range based primarily upon data from the pre-1992 period. Note that the millennium timescale secular anomalies in the Earth's rotation are 'explained' as a consequence of the glacial isostatic adjustment process by the same model of the radial variation of mantle viscosity. Reproduced from Peltier WR and Jiang X (1996) Glacial isostatic adjustment and Earth rotation: Refined constraints on the viscosity of the deepest mantle. *Journal of Geophysical Research* 101: 3269–3290 (Correction, *Journal of Geophysical Research* 102: 10101–10103, 1997).

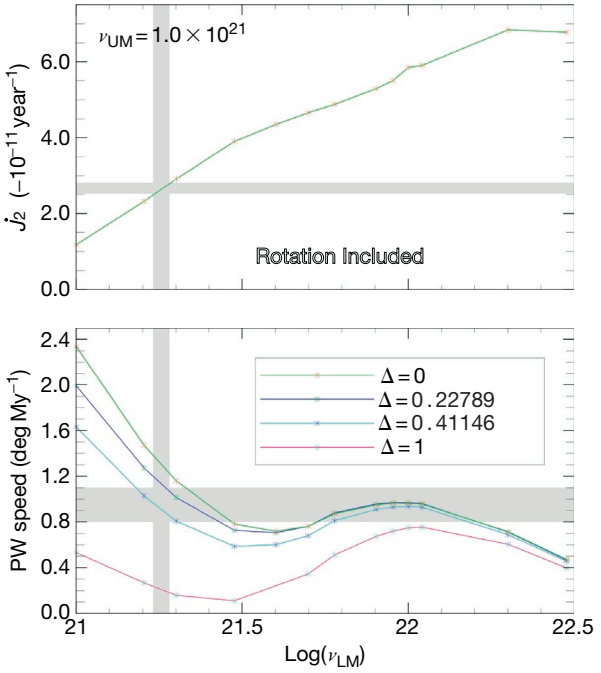

Figure 25 The earlier analysis shown in **Figure 24** as a function of the extent to which a difference between k_f and $k_2^T(s=0)$ is taken into account and is taken from the paper of Peltier and Luthcke (2009). The case $\Delta=0$ corresponds to the equivalent Earth model approach of Munk and MacDonald (1960) for which $k_f=k_2^T(s=0)$. The case $\Delta=1$ corresponds to a case in which the elastic lithosphere is assumed to maintain its global integrity in the limit $t\rightarrow\infty$. The additional cases both correspond to cases in which the infinite time limit of the elastic lithospheric thickness vanishes and in which either one or the other of the values of k_f shown in **Figure 7** is assumed. Notable is the fact that the finite infinite time elastic lithospheric thickness case is ruled out, whereas the zero infinite time thickness results continue to reconcile the data.

in which, aside from the surface load forcing associated with the Late Quaternary ice-age cycle, additional surface load forcing has been added to the model representing the modern global warming-induced land-ice melting that is currently ongoing in Greenland, Antarctica, and Alaska and that is directly constrained by analysis of the time-dependent gravity observations being provided by the GRACE satellite system. These GRACE-inferred melt rates have recently been reviewed in Peltier (2009) whose original analyses have confirmed the validity of the earlier results by Velicogna and Wahr (2006a,b) for Greenland and Antarctica but significantly reduced the inferred rate of melting from the high mountains of Alaska according to earlier analyses. The results from model A for $\dot{J}_2$ demonstrate that the influence of these additional sources of land-ice melting causes a marked reduction in $\dot{J}_2$ that appears to plausibly explain the strong reduction in the value of this parameter described in Roy and Peltier (2011). This is confirmed in **Figure 28** in the construction of which it is assumed that the base model accurately fits the pre-1992 observations and the anomalies associated with the melting of ice from these three polar ice-sheet catchments are simply added to the prediction of the base model. Although this additional forcing alone appears to fit the post-1992 shift in the value of $\dot{J}_2$ inferred by Roy and Peltier (2011), we will see in what follows that this explanation is seriously flawed. Not only does it not simultaneously fit the observed shift in polar wander speed and direction as will be clear by inspection of the data in the table but also critical features of the geoid height time dependence represented by the Stokes coefficients of degree 2 and order 1 are also violated.

9.09.5.3 Measurements of the Expected Quadrupolar 'Signature' of Rotational Feedback in Postglacial Sea-Level Histories

In order to adequately test the veracity of the theory that has been developed to compute the Earth's rotational response to the glaciation–deglaciation cycle and thereby to adequately test our understanding of the history of Earth's rotation on millennial timescales, the use of the global patterns of postglacial relative sea-level change predicted by the different versions of the calculation might be expected to be especially useful. As previously noted, these patterns are best illustrated by global predictions of the present-day rate of relative sea-level rise that would be expected to be observed as a secular rate of change on a tide gauge installed in a coastal location if the only contribution to relative sea-level history were the continuing impact of

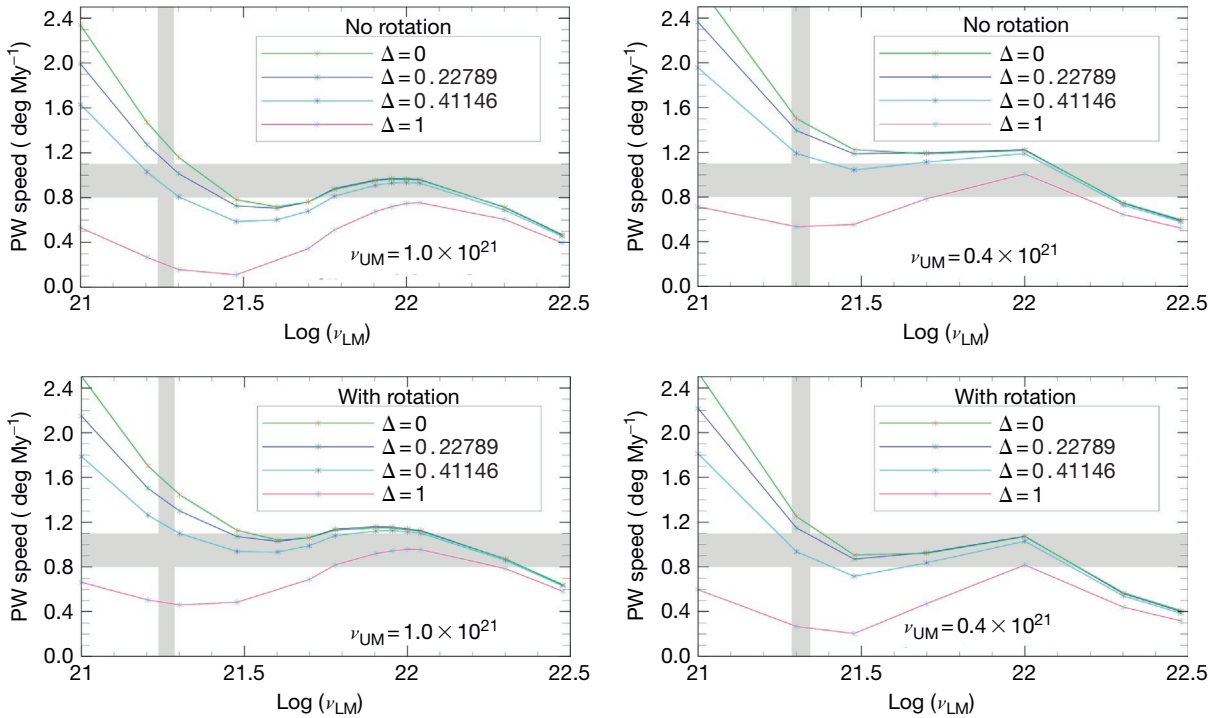

Figure 26 The results of analyses similar to those shown in the preceding text in **Figure 25** but solely for the polar wander speed datum. These results describe the sensitivity of the fits to the observation of polar wander speed in the pre-1990s era to two variations upon the basic calculation. These variations compare the sensitivity of the results to variations in the upper-mantle viscosity by changing the upper-mantle value from 1E21 to 0.4E21 Pa s and also to variations in the ocean component of the surface load by either including (with rotation) or excluding (no rotation) the redistribution of the water among and within the ocean basins due to the influence of rotational feedback.

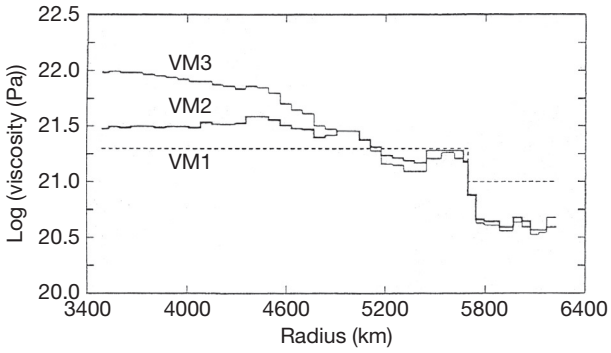

Figure 27 Viscosity models VM1, VM2, and VM3 originally inferred in Peltier (1994, 1996a,b,c) on the basis of full Bayesian inversions of a subset of the observational constraints pertaining to the GIA process. Model VM1 was the starting model employed to initiate the Bayesian inversion that employed the methodology of Tarantola and Valette (1982a,b). Control on the viscosity in the deepest mantle was provided solely by the rotational constraint based upon the observation of the parameter $\dot{J}_2$ as inferred by Cheng et al. (1989) in the analysis that delivered VM2 from the inversion. Model VM3 was obtained in an inversion that adjusted the observed value of $\dot{J}_2$ so as to allow for the influence of possible contamination due to the influence of modern climate change-induced forcing due to melting from either the Greenland or Antarctic ice sheets. These adjustments were based upon the assumption that one or the other or both of these ice catchments were contributing to the current rate of global sea-level rise at a rate in the range 1–1.5 mm year^{-1}.

the GIA process. **Figure 29** shows Mollweide projections of the global map of this prediction for the ICE-5G and ICE-6G models both including and excluding the impact of rotational feedback. These calculations have been made by solving the SLE using the 'full glacial cycle' methodology for incorporation of the influence of coastline migration discussed in Peltier (2005) and Peltier and Fairbanks (2006). Inspection of the figures for the ICE-5G (VM2) model reinforces the fact that the impact of rotational feedback is such as to superimpose upon the pattern predicted by this model with feedback, a modification that has the form of a spherical harmonic of degree 2 and order 1, a pattern of 'quadrupolar' form. This characteristic of the relative sea-level response to variations in the Earth's rotation was first demonstrated by Dahlen (1976) in the context of his analysis of the 'pole tide' raised in the oceans by the Chandler wobble of the Earth. Initial attempts to incorporate the influence of rotational feedback upon the variations of sea level caused by the GIA process were described by Milne and Mitrovica (1996) and Peltier (1998) who employed the theory of Peltier (1982) and Wu and Peltier (1984) to estimate the magnitude of the effect, analyses that initially suggested it to be small enough to be neglected. The fact that the influence of rotational feedback has this quadrupolar structure is a consequence of the dominance of the contribution due to the influence of TPW, as will be clear on the basis of inspection of eqns [13]. The ω_3 (nontidal acceleration of rotation-related) component of the perturbation to the angular velocity of the planet controls the impact upon sea-level

Table 2 List of the results for the predictions of the Earth's rotation observables for the models analyzed in this paper and the results for the two Stokes coefficients of degree 2 and order 1 in the analyses of GRACE time-dependent gravity data published by Peltier and Luthcke (2009)

Model	*PW speed deg 10^{-6} years*	*PW angle*	$\dot{J}_2 \times 10^{11}$	$\dot{C}_{21} \times 10^{11}$	$\dot{S}_{21} \times 10^{11}$
ICE-6G (VM5aD1)	1.03	−77.69	−3.25	−0.32	1.45
Model A = ICE-6G (VM5aD1) + Grn + Ant + AK	1.64	−57.76	+0.22	−1.24	2.00
Models consisting of model A augmented by melting in SA + Him + Cordillera					
Model B	0.67	−59.63	−1.46	−0.49	0.86
Model C	0.77	−65.36	−1.45	−0.46	1.03
Model D	0.77	−65.97	−1.30	−0.46	1.04
Model E	0.79	−68.43	−1.14	−0.41	1.08
Models differing from B–D only by radial viscosity model (VM5a rather than VM5aD1)					
ICE-6G (VM5a)	0.82	−77.89	−2.78	−0.25	1.16
Model A-VM5a	1.44	−55.15	0.48	−1.17	1.70
Model B-VM5a	0.48	−52.69	−1.10	−0.42	0.57
Model C-VM5a	0.57	−61.40	−1.09	−0.39	0.74
Model D-VM5a	0.57	−62.26	−0.95	−0.39	0.75
Model E-VM5a	0.59	−65.66	−0.80	−0.35	0.80
The aforementioned are to be compared with the following: post-1992 inferences of Roy and Peltier (2011)					
Roy and Peltier (2011)	0.50	−58.0	−0.90	−0.40	+0.60

Model A is model ICE-6G (VM5aD1) of Peltier and Drummond (2010) with modern land-ice melting rates for Greenland, Antarctica, and Alaska fixed to the values inferred from GRACE time-dependent gravity data by Peltier (2009). Models B, C, D, and E are characterized by the addition of rates of land-ice melting to those of model A for sources in the Andes, the Himalayas, and the Sierras. Results are also listed for models B, C, D, and E when viscosity model VM5aD1 is replaced by viscosity model VM5a. See the text for a detailed discussion of these results.

Reproduced from Peltier WR, Drummond R, and Roy K (2012) Comment on "Ocean mass from GRACE and glacial isostatic adjustment" by D.P. Chambers et al. *Journal of Geophysical Research: Solid Earth* 117: B11403, http://dx.doi.org/10.1029/2011JB008967.

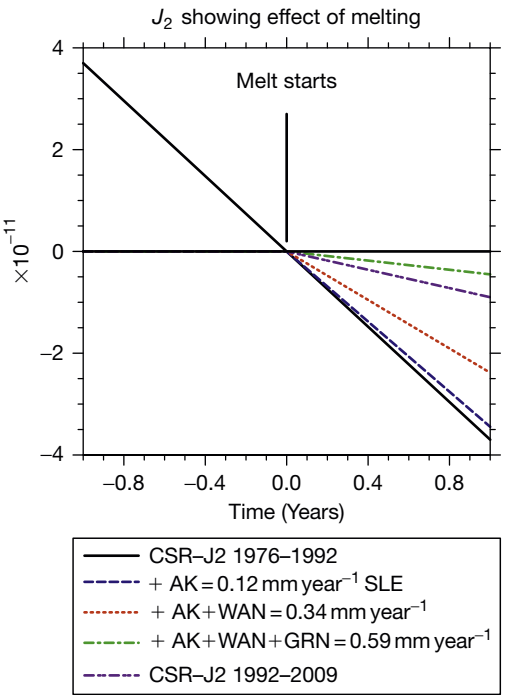

Figure 28 Based upon the assumption that a GIA model has been constructed that represents only ice-age influence and that fits the pre-1992 $\dot{J}_2$ constraint in this figure, this figure illustrates the impact to be expected upon $\dot{J}_2$ of adding the forcing associated with melting of the Greenland, Antarctic, and Alaskan accumulations of land ice as constrained by the GRACE inferences of Peltier (2009). Although this comparison suggests that the change in the secular rate $\dot{J}_2$ could be explicable solely in these terms, it is demonstrated in the succeeding text that this explanation is inadequate.

history of the GIA-induced change in the l.o.d.. The ω_1 and ω_2 perturbations, on the other hand, control the polar wander contribution, and it will be clear on the basis of eqns [13] that this will appear as a forcing of spherical harmonic degree 2 and order 1 form. Noticeable also on the basis of **Figure 29** is the fact that the magnitude of this impact is significantly more intense in the previous ICE-5G (VM2) model than it is in the more recent ICE-6G (VM5a) model, a consequence primarily of the fact that the degree 2 and order 1 Stokes coefficients for this model are larger than those for the ICE-6G (VM5a) model. This amplification of the values of these Stokes coefficients in the earlier model arose as a consequence of a fault associated with an issue fully discussed in Peltier et al. (2012) connected to the need to 'renormalize' the representation of the rotational feedback contribution to these coefficients. The difference in the magnitude of these coefficients for these two models can be exploited to examine the extent to which the magnitude of these Stokes coefficients impacts the fit to relative sea-level observations in certain regions of the Earth's surface. Since it is in the regions centered within the 4 'bull's-eyes' of the spherical harmonic degree 2 and order 1 quadrupole pattern that the influence of rotational feedback will be most apparent, it is in these regions that we should expect to find its consequences most clearly revealed.

The most important region in which such comparison is possible concerns the extremum in rotational feedback that is located on the southern tip of the South American continent (see **Figure 20** shown previously). Although the west coast of this continent is strongly impacted by the deformation associated with the subduction of the Nazca Plate, the east coastal margin is passive and therefore should provide an excellent region in which to attempt to measure, using postglacial histories of relative sea-level change, the impact of rotational

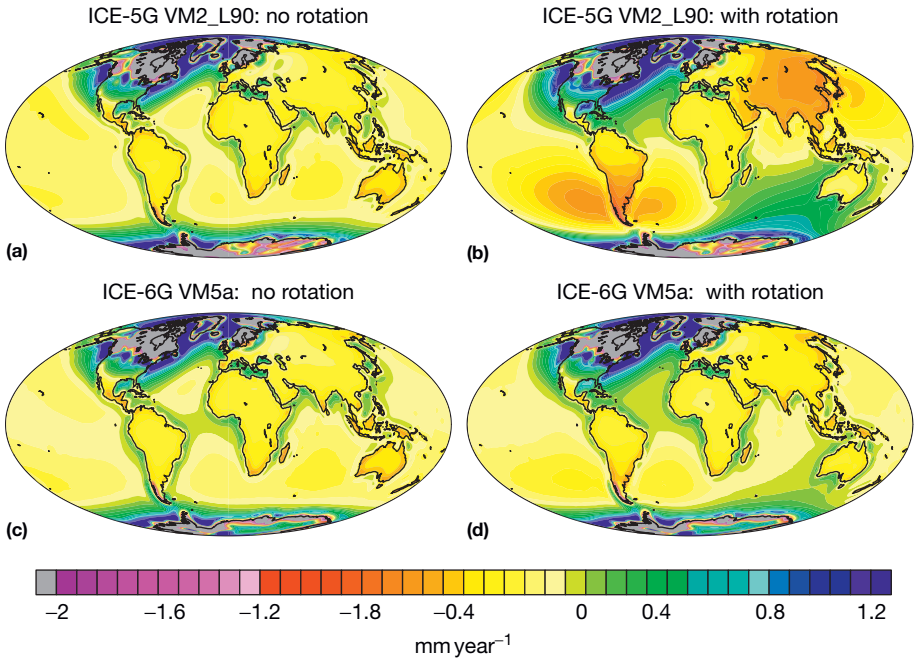

Figure 29 Comparison of the predictions of the ICE-5G (VM2) with those of ICE-6G (VM5a) models of the present-day rate of relative sea-level rise both including and excluding the influence of rotational feedback as described by the second term in the integrand of the triple convolution integral in eqn [10]. Noticeable by inspection of this figure is the fact that the influence of rotational feedback has the form of a spherical harmonic of degree 2 and order 1, which exists as a consequence of the dominant role played in the feedback process by the polar wander component of the rotational response to the GIA process (see eqns [36a] and [36b]). Also evident is the fact that this feedback is stronger in model ICE-5G (VM2) than it is in ICE-6G (VM5a). This is a consequence of the fact that the degree 2 and order 1 Stokes coefficients of the latter model are significantly smaller than those of the former, in fact by a factor of 2.51 as we will see in the succeeding text. Comparing this figure with the equivalent in Peltier (2007a,b) will demonstrate that the results for model ICE-6G (VM5a) are similar to those of the previous model ICE-4G (VM2) as the latter model is characterized by degree 2 and order 1 Stokes coefficients that are very close to those of the ICE-6G (VM5a) model.

feedback. Figure 30 shows a map of the South American continent, from Peltier (2005), on which, primarily, along the east coast passive continental margin, the locations are shown at which, based upon the compilation of relative sea-level histories in Rostami et al. (2000), radiocarbon-dated relative sea-level history information is available. When such data are used to compare with the predictions of the theory previously described, they must of course be transformed onto the calendar year timescale using the modern calibration procedure CALIB described by Stuiver and Reimer(e.g., 1993 and subsequent releases).

In Rostami et al. (2000), attention was drawn to the fact that there seemed to exist a systematic misfit of the theory for postglacial sea-level change based upon the ICE-4G (VM2) model without rotational feedback to the observed sea-level histories from this coastal region. The nature of this misfit, documented in Figure 11 of Rostami et al. (2000), involved the variation with latitude of the so-called mid-Holocene 'high stand' of the sea. The prediction of the amplitude of this high stand using the ICE-4G (VM2) model without feedback was that this amplitude should decrease with increasing south latitude, whereas the observation was that it actually increased very significantly, a qualitative difference easily resolved by the observational record if the data were being interpreted correctly. In Peltier (2002c), it was first demonstrated that the

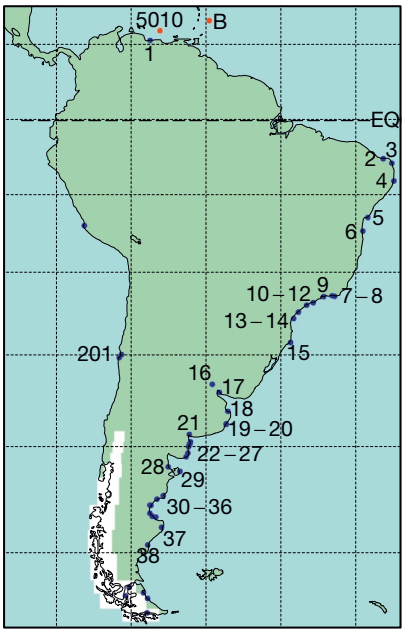

Figure 30 Location map for the South American sites from which radiocarbon-dated relative sea-level histories are available. Also shown in the figure is the LGM location of the Patagonian ice-sheet complex.

incorporation of rotational feedback into the theory would lead to the qualitative change in the nature of the prediction required to reconcile the observations, but significant discrepancies remained for the data from the southernmost section of the coast. More recently, Peltier (2005) has more fully exploited these observations and the ICE-4G (VM2) model predictions to argue that this data set could be invoked to demonstrate that the impact of rotational feedback upon RSL history predicted by the ICE-4G (VM2) model was approximately correct. In fact, the data–model comparisons presented in both Peltier (2002c) and Peltier (2005) were incomplete, as several of the most anomalous of the observations could not be reconciled.

The importance of including the ICE-5G calculations together with those for the ICE-6G model for present purposes is that the former model is characterized by an excessively large contribution from the degree 2 and order 1 Stokes coefficients as previously mentioned. This model may therefore be seen as a surrogate for models that share this characteristic. By comparing the predictions to South American east coast observations, we will be able to isolate the extent to which, as well as the sense in which, the magnitude of the degree 2 and order 1 Stokes coefficients directly impacts sea-level history in this critical region. Although we will not discuss this additional sensitivity here, the influence of a modest deviation from the 'equivalent Earth model' assumption of Munk and MacDonald (see Peltier and Luthcke (2009) for further discussion) is also of interest although, as explicitly demonstrated in Peltier and Luthcke (2009), this influence appears to be negligible in comparison with the more important influences under discussion.

Figure 31 presents model–data comparisons for postglacial relative sea-level history at 16 of the numbered sites from the east coast of South America, beginning at the northernmost site from coastal Venezuela and continuing southward through Brazil and Argentinean Patagonia towards Tierra del Fuego. For each site, the predictions for three different models are shown. These are for the ICE-5G (VM2) model that includes the influence of rotational feedback and for the ICE-6G (VM5a) model both including and excluding this influence. It will be important to note that the first site in the list, denoted NC Venezuela (Valastro et al., 1980), is the only site that is north of the equator (see **Figure 30**). This is important because the sign of the impact of rotational feedback changes across

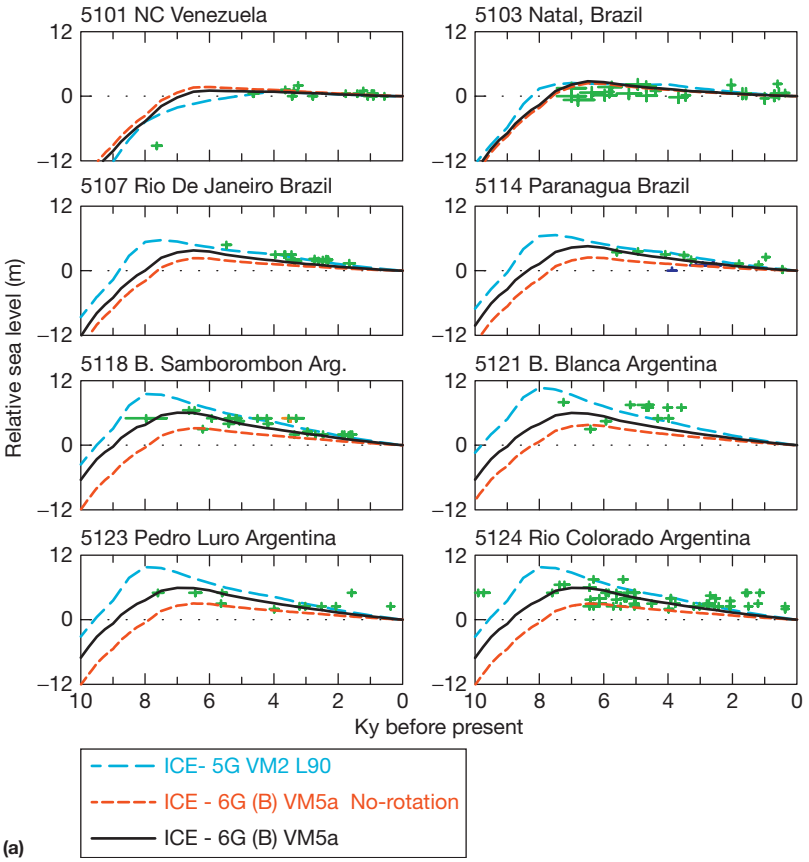

Figure 31 (a) Model–data intercomparisons for eight sites from the northern portion of the east coast of the South American continent. The last two digits of the site numbers correspond to the numbered locations in **Figure 30**. On each plate, the ^{14}C-dated sea-level index points are denoted by green crosses. RSL history predictions based upon eqn [10] are shown for three model variants, respectively, ICE-6G (VM5a) with rotational feedback (black), ICE-6G (VM5a) without rotational feedback (red), and ICE-5G (VM2) with rotational feedback (mauve). Notable based upon the comparisons at these north coastal sites is that the previous ICE-5G (VM2) model with rotational feedback has an excessive amplitude of this influence, whereas the ICE-6G (VM5a) model has a more modest rotational feedback effect, which is in much closer accord with the data. In the absence of rotational feedback, however, one cannot fit the observations of the mid-Holocene high stands of the sea that are recorded in this region.

(Continued)

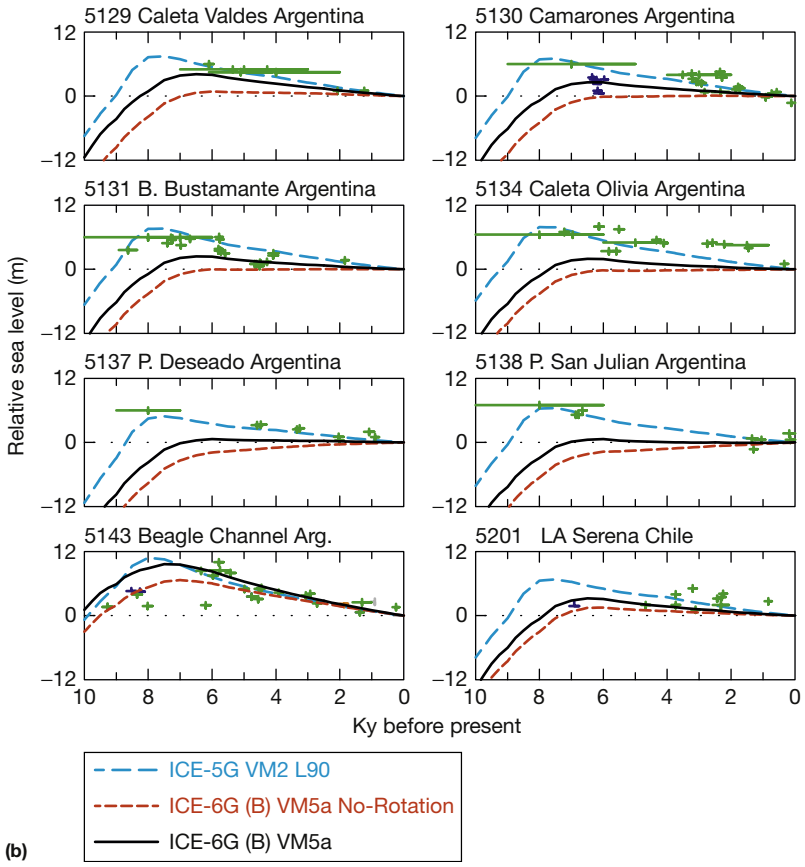

Figure 31, Cont'd (b) Same as (a) but for a set of eight sites from the southern (Patagonian) region of the east coast of the South American continent. At these locations, the results of the intercomparisons strongly conflict with those from the northern segment of the coast in strongly preferring the very large-amplitude rotational feedback effect over the weaker influence due to this cause that is embodied in the ICE-6G (VM5a) model and the precursor model ICE-4G (VM2).

this line of 0° latitude, as expected based upon the spherical harmonic degree 2 and order 1 form of the pattern of this influence. To the north of the equator, as will be clear by inspection of the comparisons at NC Venezuela, the impact of rotational feedback is to diminish the predicted elevation with respect to sea level throughout the Holocene interval from 10 ka onward. To the south of the equator, however, as the comparisons for the Natal, Brazil, site (Bezerra et al., 2003) show, the opposite is the case, as at this site, the impact of rotational feedback is such as to elevate the predicted sea levels for the Holocene epoch above that for which this influence is neglected entirely. Based upon the difference in the values of the degree 2 and order 1 Stokes coefficients for the ICE-5G and ICE-6G models as will be discussed in detail in the following section of this chapter, it will be clear that the influence of rotational feedback is expected to be weaker in ICE-6G (VM5a) than it is in ICE-5G (VM2). As will be evident by inspection of the complete set of comparisons shown in Figure 31, this hierarchy is preserved at all locations. Table 3 lists the references for the data from all of the sites for which data–model comparisons are being shown in this section.

Very clearly evident also, based upon the results shown in Figure 31, is the fact that exceptionally high 'stands' of the sea above present sea level are predicted and observed to obtain at sites along this coast during mid-Holocene time between 6000 and 8000 years before present. Although there is considerable scatter in the data at the sites from NC Venezuela to Rio Colorado, Argentina, for which comparisons are shown in Figure 31(a), it is nevertheless clear that the influence of rotational feedback is required in order for the model to adequately reconcile the data. In the absence of this influence, the amplitude of the recorded mid-Holocene high stands is insufficient. As discussed in detail in Rostami et al. (2000), most of the data from this set of locations are from the older literature, and therefore, a legitimate question exists concerning its quality. A general conclusion that nevertheless follows for the comparisons in Figure 31(a) is that the predictions of the previous ICE-5G (VM2) model of the amplitude of the mid-Holocene high stands at these locations are excessive. This is encouraging because we expect that the degree 2 and order 1 Stokes coefficients for the ICE-6G (VM5a) model are more accurate than those for the previous ICE-5G (VM2) model for the Holocene interval.

Considering next the comparisons for the collection of sites shown in Figure 31(b), the situation is reversed, in that it is only the very large-amplitude high stand predictions of the ICE-5G (VM2) model that are able to reconcile the data from these more southerly locations. Even for the more recently collected data from this region, however, significant issues are evident. Concerning the data from the set of locations between

Table 3 References for the data from the sites for which data–model intercomparisons are provided in this chapter

Site number	*Site name*	*References*
5101	NC Venezuela	Valastro et al. (1980)
5103	Natal, Brazil	Bezerra et al. (2003)
5107	Rio de Janeiro, Brazil	Martin et al. (1987), Fairbridge (1976), Delibrias et al. (1974), and Angulo and Lessa (1997)
5114	Paranaguá, Brazil	Angulo and Lessa (1997)
5118	B. Samborombón, Argentina	Codignotto et al. (1992)
5121	B. Blanca, Argentina	Codignotto et al. (1992)
5123	Pedro Luro, Argentina	Albero and Angiolini (1983, 1985)
5124	Rio Colorado, Argentina	Codignotto et al. (1992)
5129	Caleta Valdés, Argentina	Rostami et al. (2000), Codignotto et al. (1992), and Albero and Angiolini (1983)
5130	Camarones, Argentina	Rostami et al. (2000)
5131	B. Bustamante, Argentina	Rostami et al. (2000)
5134	Caleta Olivia, Argentina	Rostami et al. (2000)
5137	P. Deseado, Argentina	Rostami et al. (2000)
5138	P. San Julián, Argentina	Rostami et al. (2000)
5143	Beagle Channel, Argentina	Porter et al. (1984) and Morner (1991)
11105	Pt. Adelaide/ Gillman, Australia	Belperio et al. (2002)
11107	Pt. Wakefield, Australia	Belperio et al. (2002)
11109	Pt. Pirie (Spencer Gulf), Australia	Belperio et al. (2002)
11110	Redcliffe, Australia	Belperio et al. (2002)
11111	Franklin HB, Australia	Belperio et al. (2002)
11113	Ceduna, Australia	Belperio et al. (2002)
11115	Weiti River, New Zealand	Gibb (1986) and Schofield (1975)
111123	Blue Skin Bay, New Zealand	Gibb (1986)
9003	Nouakchott, Mauritania	Faure and Hebrard (1977)
9006	St. Louis, Senegal	Faure et al. (1980)
9022	Reunion	Camoin et al. (1977, 2004)
9023	Mauritius	Camoin et al. (1997)
11004	Shikoku island, Japan	Pirazzoli (1978)
11006	Kikaijima island, Japan	Pirazzoli (1978) and Sugihara et al. (2003)
11008	S. Okinawa island, Japan	Koba et al. (1982)
11010	Uotsuri island, Japan	Koba et al. (1982)

Caleta Valdes, Argentina, and P. San Julian, Argentina, all from Argentinean Patagonia, it will be evident that at several of these locations, only a single data point exits rather than a continuous relative sea-level history. At these locations, although the data are thought to have been carefully screened for quality (see discussion in Rostami et al. (2000)), it is clear on the basis of them that only the ICE-5G (VM2) model is able to reconcile the 6–8 m mid-Holocene high stands of the sea that are observed to exist in the time window between 6 and 8 thousand years before present. The ICE-6G (VM2) model, in the absence of rotational feedback, inevitably predicts that no such high stand should exist or, with feedback, that its amplitude is unacceptably small. The ICE-5G (VM2) model predicts a high stand amplitude that does fit these extremely high isolated RSL data points, but this model is known to be characterized by values of the degree 2 and order 1 Stokes coefficients that are now understood to be exaggerated by a factor of precisely 2.51 for viscosity model VM2 (see the detailed discussion in Peltier et al. (2012)). These analyses very strongly reinforce the conclusion in Peltier (2005, 2007) that the influence of rotational feedback is apparently crucial to understanding the relative sea-level history data from along this coast. However, neither the VM2 nor the VM5a viscosity model is characterized by Stokes coefficients of degree 2 and order 1 that are large enough to explain the data from the southernmost region of the coast. It remains an open question whether a further variation on the viscosity model or loading history will enable the correction of this characteristic misfit. We are also unable to rule out the possibility that the extremely large-amplitude isolated high stands inferred to exist at the Patagonian sites could correspond to storm beach deposits or to exist as a consequence of the influence of a marked changes in the (palaeo)tidal regime in the range of time during which the extreme changes in relative sea level were recorded (e.g., see Griffiths and Peltier (2009); Hill et al. (2011); and Hall et al. (2013); the latter papers provide analyses for the US east coast that take changes in tidal range into account in the interpretation of radiocarbon-dated RSL histories along this coast).

It is nevertheless the case that there is scatter in the data, and one might reasonably hope that there might exist data from other locations where the influence of rotational feedback is also expected to be strong that might be invoked to confirm (or to deny) the robustness of the conclusion that the influence of rotational feedback upon the GIA process is significant and is required to understand the available observational constraints. To this end, **Figure 32** shows a location map for 16 additional sites from other regions, for some of which, this influence is expected to be similarly evident. Eight of these sites are from the New Zealand–Australia region, for which comparisons with model predictions are shown in **Figure 33**. These sites are within the influence of the second southern hemisphere 'bull's-eye' of the spherical harmonic degree 2 and order 1 pattern that is produced by the influence of rotational feedback. The map in **Figure 32(c)** (in Mercator projection), upon which all of these additional positions are located, is that of the difference between the present-day rate of sea-level rise prediction for the ICE-6G (VM5a) model with rotation (shown previously in **Figure 32(a)**) and that obtained when this influence

is not included (shown in Figure 32(b)). The eight additional comparisons shown in Figure 34 are for sites of which 4 are from locations in the Indian Ocean or the west coast of Africa and 4 of which are from the third 'bull's-eye' located over the Japanese islands (see Figure 32(c)).

Inspecting first the comparisons shown in Figure 33 for sites in the Australia–New Zealand region will show that at all of these sites, there exists a striking anomaly between the predictions of the version of the ICE-6G (VM5a) model without rotational feedback and the predictions for either of the models in which this influence is included. In the absence of rotational feedback, the theory predicts that a mid-Holocene high stand of the sea should exist with an ~3 m amplitude. However, the data at all 8 locations show that no such feature is evident. At most of the locations for which results are shown in Figure 33, either of the two models with rotational feedback included significantly reduces the amplitude of this predicted feature (ICE-6G (VM5a)) or eliminates it entirely (ICE-5G (VM2)). Again, only the latter model with the excessive values of the degree 2 and order 1 Stokes coefficients fits the observations as was the case along the southeast coast of the South American continent. This set of comparisons is especially important because in this region, the sign of the feedback effect is predicted to be opposite to that operating over the South American continent. Nevertheless, the necessity of the operation of a strong influence of rotational feedback in order to fit the observational constraints remains clear.

The further model–data comparisons shown in Figure 34 include information from sites in which the sign of the influence of rotational feedback is the same as that that operates in the Australia–New Zealand region and sites in which the influence is qualitatively similar to that evident at locations along the southeast coast of the South American continent. Sites of the former type include those along the west coast of Africa (Nouakchott, Mauritania, and St. Louis, Senegal) and the others from the Indian Ocean (Réunion and Mauritius). Sites of the latter type from the islands of Japan include Shikoku island, Kikaijima island, S. Okamura island, and Uotsuri island. At the former locations, theory once more predicts that in the absence of rotational feedback, a mid-Holocene high stand of the sea should be observable. At these locations, however, no such high stand is evident. The addition of rotational feedback, of the excessively high strength embodied in ICE-5G (VM2), once more allows the model to fully reconcile the data, whereas although the predictions of the follow-on ICE-6G (VM5a) model demonstrate that there should be a nonnegligible impact of rotational feedback at these locations, the strength of the feedback appears to be weaker than required.

Turning next to the final set of four data–model comparisons shown in Figure 34, it will be clear that at each of the Japanese islands for which relative sea-level comparisons are shown, the model without rotational feedback predicts that no mid-Holocene high stand of the sea should be evident at any of these locations. Yet, the data in each case clearly reveal the presence of such a feature. As will be clear by inspection of this set of comparisons, the incorporation of the influence of rotational feedback suffices to reconcile the misfits of the theoretical predictions to the data that would otherwise exist for the ICE-5G (VM2) model in which this feedback is excessively

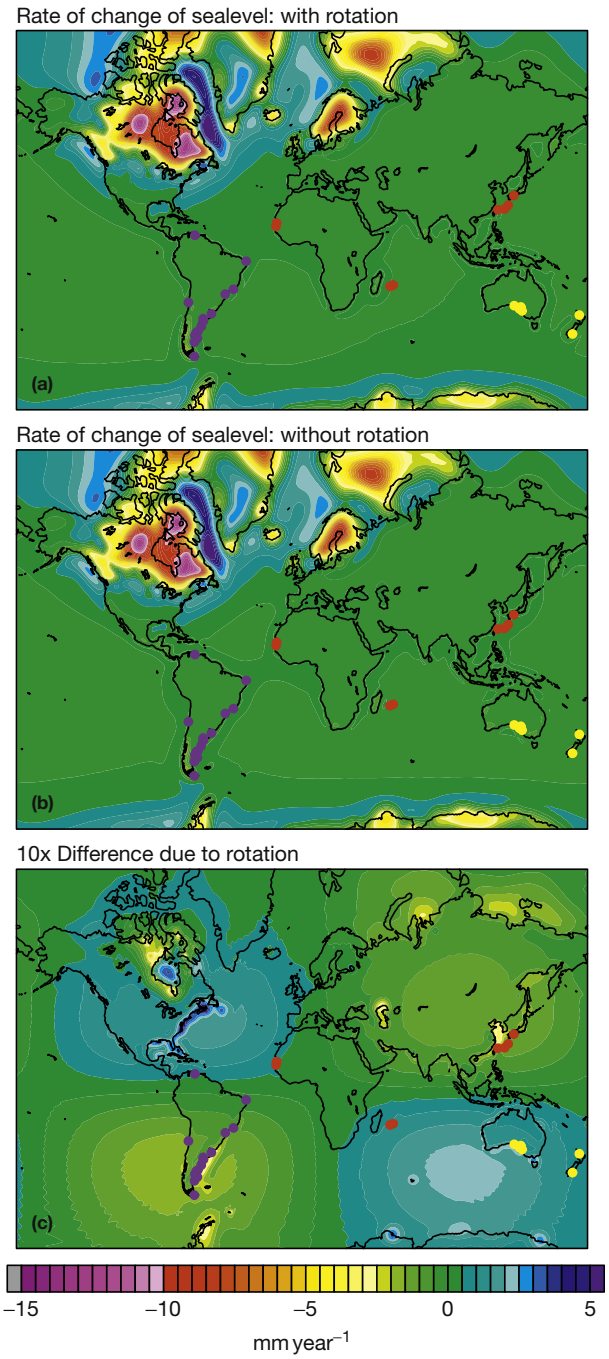

Figure 32 Mercator projections of the model-predicted present-day rate of relative sea-level rise for the ICE-5G (VM2) model both including (a) and excluding (b) the influence of rotational feedback. In (c), the difference between (a) and (b) is presented, demonstrating once more that the influence of the rotational feedback effect is dominantly of the form of a spherical harmonic of degree 2 and order 1. Superimposed upon each of the three plates of this figure are the locations of sites at which high-quality ^{14}C-dated RSL histories are available beyond those from the South American continent already discussed. The sites shown as yellow dots are located in a region (Australia–New Zealand) where the influence of rotational feedback is expected to have the opposite sign as the South American locations. At the sites shown as red dots, the effect is either expected to the same as in Australia–New Zealand (in the Indian Ocean or West Africa) or the same as in South America (Japanese islands).

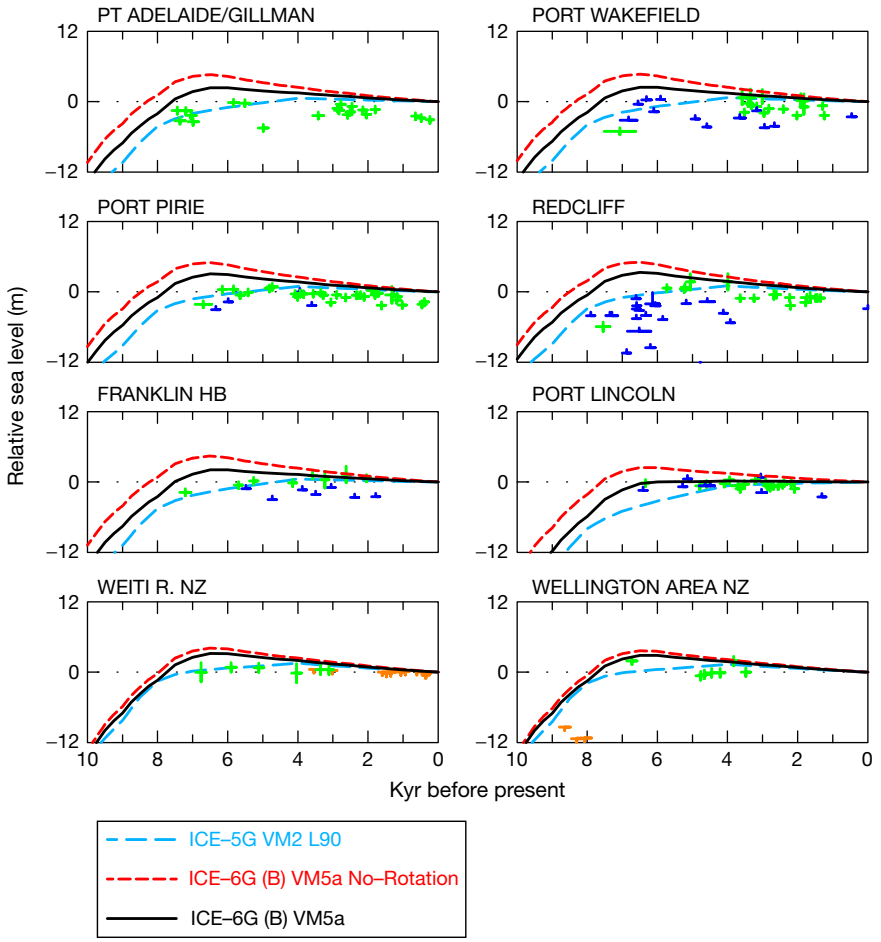

Figure 33 Same as **Figure 31(a)** but showing model–data comparisons for the Australia–New Zealand region. Inspection of these comparisons demonstrates that, as expected, the nature of the influence of rotational feedback is opposite to that observed at the South American locations. At these locations, the data once more appear to strongly prefer the model with the overly strong rotational feedback embodied in ICE-5G (VM2).

strong, but even in the ICE-6G (VM5a) model for which the feedback is weaker, it remains a nonnegligible influence.

On the basis of the totality of these comparisons, we may therefore conclude that there exists very strong evidence in the global record of postglacial sea-level history of the action of the influence of rotational feedback. However, the strength of this feedback in the new ICE-6G (VM5a) model of the GIA process appears to be somewhat weak, as it was in the precursor model ICE-4G (VM2). In fact, this is not surprising as the procedure employed to construct the ICE-4G (VM2) model did not suffer from the same technical flaw that arose in the course of the ICE-5G (VM2) reconstruction process. In the ICE-5G (VM2) model, however, in which the larger magnitude of the critical Stokes coefficients of degree 2 and order 1 was excessive for the VM2 viscosity profile, the strength of the required feedback appears to be just what is required to best fit the observations. It remains to be seen whether it will be possible to further refine the radial profile of mantle viscosity or the ice-sheet loading history in such a way as to increase the values of the Stokes coefficients for ICE-6G (VM5a) without violating additional constraints. That this could be possible follows from the fact that the rotational anomalies depend only upon the viscosity of the deepest mantle not upon the shallower structure to which relative sea-level histories are uniquely sensitive.

9.09.6 Grace Satellite Inferences of Geoid Height Time Dependence: The Combined Influences of Ice Age and Modern Land-Ice Melting

At several points in the previous section of this chapter, I have commented on the importance of the time-dependent geoid as a representation of the strength and spatial characteristics of the ongoing process of global GIA. With the launch of the GRACE satellites in March of 2002, it became possible to directly measure an approximation to this field globally and to begin to disentangle the contributions to it from ice-age-related GIA and from the modern climate change-related processes that also contribute. In this section of this chapter, my purpose is to review a series of recent results that have contributed to refining our understanding of geoid height time dependence and the approximation to it that the GRACE system is

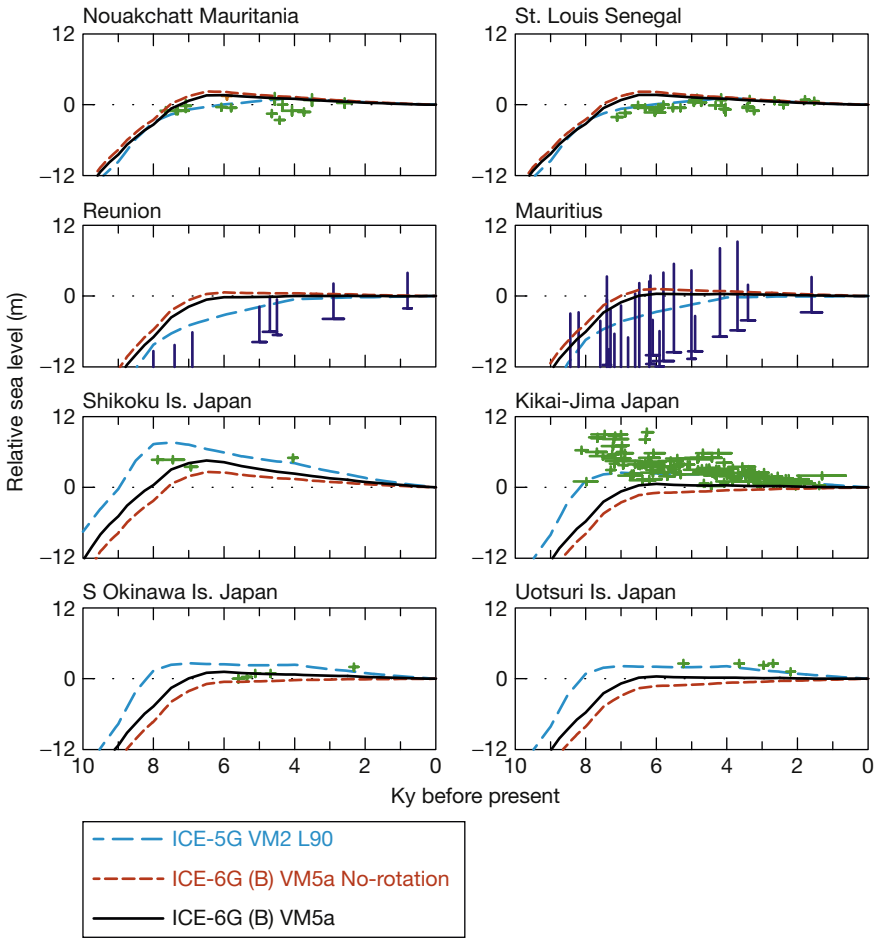

Figure 34 Same as for **Figure 31(a)** but showing model–data comparisons for both 'down sites' (Indian Ocean and West Africa) and 'up sites' (Japanese islands). For all sites, the sign of the rotational feedback effect is as expected and most data appear to prefer model ICE-5G (VM2), which embodies excessively strong rotational feedback.

actually able to observe, as these results are proving to be critical to our ability to make full use of the measurements, especially insofar as the extraction of modern climate change-related information is concerned.

To begin, it is important to be reminded of the formal definition of the geoid of classical geodesy as the surface of constant gravitational plus centrifugal potential that overlaps the surface of the sea in the absence of currents and tides. When we solve the sea-level equation [10] to obtain the history of relative sea-level change to be expected anywhere on the Earth's surface due to the time-dependent exchange of mass between the oceans and land-based ice sheets, the solution is explicitly constructed so as to ensure that the new position-dependent and time-dependent sea level at every instant of time lies on such a globally defined geoid. Although the gravitational plus centrifugal potential characteristic of this geoid varies with time as mass is exchanged between the oceans and the continents and as the rotational state of the planet evolves, the ocean surface by construction remains such an equipotential. Now, this representation through the SLE of the time-evolving geoid is an approximation for a number of reasons. First, it is based upon the assumption that the system is evolving sufficiently slowly that the quasistatic approximation that lies at the heart of the SLE is an adequate approximation. This neglects the dynamic processes that are actually responsible for redistributing the water among the ocean basins that is required to produce a sea surface that is in fact equipotential. Furthermore, of course, there will exist a steric impact upon sea level that also acts to raise or lower the level of the sea during the climate changes that are responsible for inducing the exchange of mass between the oceans and the continents. When we employ the solutions of the SLE based upon eqn [10] to predict sea-level history, we are assuming that the steric overprint upon the mass effect is sufficiently small as to be negligible. This issue has never been adequately explored but can be using an appropriately modified version of the SLE formalism coupled to a full glacial cycle integration of a modern coupled atmosphere–ocean climate model. Since current computational resources remain inadequate to the latter task, it will be some time before this might reasonably be attempted.

9.09.6.1 The Geoid Equation: Analytic Results for the Stokes Coefficients of Degree 2 and Order 1

Since the classical geoid is defined in terms of sea level, it should be clear that, notwithstanding the approximations

upon which the SLE is based, it must provide the basis for a prediction of its time dependence. If the geoid is to be observed from space, it is also clear that the sea level that it represents will be measured not with respect to the surface of the solid Earth but rather with respect to the planet's center of mass relative to which the orbit of an Earth satellite is represented. This shift of the datum with respect to which the evolving sea level is measured is easily accommodated in the SLE formalism. Using this apparatus, we may define the space–time evolution of the quasistatically evolving geoid as

$$G(\theta,\lambda,t)=\left[\int_{-\infty}^{t}\mathrm{d}\tau\iint_{\Omega}\mathrm{d}\Omega'\left\{L(\theta',\lambda',\tau)G_G^L(\phi,t-\tau)+\Psi^R(\theta',\lambda',\tau)_RG_G^T(\phi,t-\tau)\right\}+\left\{\frac{\Delta\Phi(t)}{g}\right\}\right] \quad [45]$$

In this equation, the geoid Green function for the surface load is

$$G_G^L(\phi,t)=\frac{a}{M_e}\sum_{l=0}^{\infty}\left(\delta(t)+k_l^L(t)\right)P_l(\cos\phi) \quad [46]$$

in which 'a' is the Earth's radius and M_e is the Earth's mass. The corresponding renormalized Green function for the impact upon the geoid associated with the changing rotation is, correspondingly,

$${}_RG_G^T(\phi,t)=\frac{1}{g}\sum_{l=0}^{\infty}\left(\delta(t)+k_l^T(t)\right)\frac{2l+1}{4\pi}P_l(\cos\phi) \quad [47]$$

in which 'g' is the acceleration of gravity at the Earth's surface and the factor $(2l+1)/4\pi$ is the renormalization factor previously discussed in connection with eqn [10]. The parameters $k_l^L(t)$ and $k_l^T(t)$ in eqns [40] and [47], as before, are the viscoelastic surface mass load and tidal potential load Love numbers, which enable the aforementioned Green functions, when convolved with the surface mass load and tidal potential load, respectively, to translate these applied 'forcings' into the impacts upon the surface gravitational plus centrifugal potential field (the geoid) due to both the instantaneous effect of the forcing and the induced internal redistributions of mass that it causes. Insofar as the geoid is concerned, however, these variations of potential are now measured with respect to the center of mass of the planet rather than with respect to the surface of the solid Earth. The only difference between a solution for relative sea-level history from eqn [10] and a solution for geoidal history from eqn [39] is therefore a shift in the local datum from the surface of the solid Earth in the former case to the center of mass in the latter case. The Green functions that appear in eqns [14] differ from those of eqns [46] and [47] only in that their expansions include additional contributions to the degree-dependent amplitudes that involve the negative of the appropriate Love number for radial displacement (see the succeeding text). The theory required to construct the time-dependent Love numbers was first articulated in Peltier (1974) and Peltier and Andrews (1976). In the Green function expression for the surface load, the addition theorem for spherical harmonics (e.g., Mathews and Walker, 1987) may be invoked to write

$$P_l(\cos\gamma)=\frac{1}{(2l+1)}\sum_{m=-l}^{+l}Y_l^{m\,*}(\Omega')\,Y_l^m(\Omega) \quad [48]$$

The issue as to whether the space-independent but time-dependent conservation of mass factor, $\Delta\Phi(t)/g$, which is clearly required in the SLE, should also appear in the geoid eqn [45] is an issue that was raised in Chambers et al. (2010) in connection with the use of the equation to compare GIA predictions of the time-dependent geoid with the GRACE satellite observations, and so, this term has been placed in brackets in eqn [45]. The term is of course required in the description of the true sea level-related geoid as discussed in detail in Peltier et al. (2012).

Although the space–time-dependent geoid may be computed directly from eqn [45], it may also be obtained by first solving the sea-level equation [10] to obtain the spherical harmonic expansion of the time-dependent relative sea-level history $S(\theta,\lambda,t)$. At every point on the surface, one may then compute its time derivative, $\dot{S}(\theta,\lambda,t)$ say. The time dependence of geoid height may then be obtained by next computing the radial displacement of the solid Earth, $R(\theta,\lambda,t)$ say. The latter calculation is performed by evaluating the triple convolution integral:

$$R(\theta,\lambda,t)=\int_{-\infty}^{t}\mathrm{d}t'\iint_{\Omega}\mathrm{d}\Omega'\left\{L(\theta',\lambda'',t')G_R^L(\phi,t-t')+\Psi^R(\theta',\lambda',t')_RG_R^T(\phi,t-t')\right\} \quad [49]$$

in which the Green functions for the radial displacement due to the surface mass load and due to the variation in the centrifugal potential are (Peltier, 1974; Peltier and Andrews, 1976)

$$G_R^L(\phi,t))=\frac{a}{M_e}\sum_{l=0}^{\infty}h_l^L(t)P_l(\cos\phi)$$

$${}_RG_R^T(\phi,t)=\frac{1}{g}\sum_{l=0}^{\infty}h_l^T(t)\frac{2l+1}{4\pi}P_l(\cos\phi) \quad [50a,b]$$

in which $h_l^L(t)$ and $h_l^T(t)$ are the surface mass load and tidal potential load Love numbers for radial displacement. Given $R(\theta,\lambda,t)$ from eqn [43], we may then compute its time derivative, $\dot{R}(\theta,\lambda,t)$ say. To determine the time dependence of geoid height, we may then simply compute, as originally discussed in Peltier (1999) (notwithstanding the issue connected with the time derivative of the mass conservation term in the SLE mentioned previously),

$$\frac{\mathrm{dGeoid}}{\mathrm{d}t}=\dot{S}(\theta,\lambda,t)+\dot{R}(\theta,\lambda,t) \quad [51]$$

Since both 'S' and 'R' and their time derivatives are known in terms of spherical harmonic expansions, eqn [51] also provides a spherical harmonic expansion for geoid height time dependence. In all previous calculations of this field by the Toronto group, the degree 2 and order 1 Stokes coefficients have been determined together with all other spherical harmonic coefficients directly from eqn [51]. The reader may well wonder why this two-step procedure was employed rather than working with eqn [45] for the geoid directly. The reason for this is simply that 'S' and 'R' and their time derivatives are all required for comparison with various observational

constraints. For example, 'S' is itself a relative sea-level history such as those discussed in the previous section of this chapter that may be compared to an observed history at any position on Earth's surface from which data are available, whereas $\dot{S}$ for the present day is a rate of relative sea-level rise that may be employed to correct a modern tide gauge measured rate for the influence of the GIA process. Similarly, $\dot{R}$ may be employed to compare with a GPS-measured rate of radial displacement of the Earth's solid surface, whereas R defines the instantaneous variation in the radius of the solid Earth (i.e., the time-dependent depression or uplift of the crust).

Figure 35 shows examples of the global fields $\dot{S}$, $\dot{R}$, and dGeoid/dt for the version of the same ICE-6G (VM5aD1) model employed to construct one of the polar wander paths shown in Figure 11. Clearly evident by inspection of Figure 35 is the fact that the field of geoid height time dependence contains a large-amplitude degree 2 and order 1 component due to the influence of rotational feedback, which has been discussed at length in previous sections of this chapter. One of the four extrema of this pattern is centered upon the east coast of the continental United States as is also evident in previous graphics including Figure 32. The second is that centered on the southern tip of the South American continent mentioned previously in connection with our discussion of South American east coast sea-level records. In the recent papers by Horton et al. (2009) and Engelhart et al. (2010, 2011), analyses have focused upon the extent to which relative sea-level data from the US east coast were impacted by the rotational feedback process, adding additional insight to that provided by the discussion in the previous section.

9.09.6.2 The Exact Geoid and the Approximation to It Observable by GRACE

Our further interest in this subsection is to provide exact analytic expressions for the degree 2 and order 1 Stokes coefficients that govern the degree of dominance of the degree 2 and order 1 overprint on the geoid height time dependence evident in Figure 35. The analysis to follow is original to Peltier et al. (2012) (see the supplementary material that accompanied that paper). To begin, we express the surface mass load in a spherical harmonic expansion in terms of a surface mass load

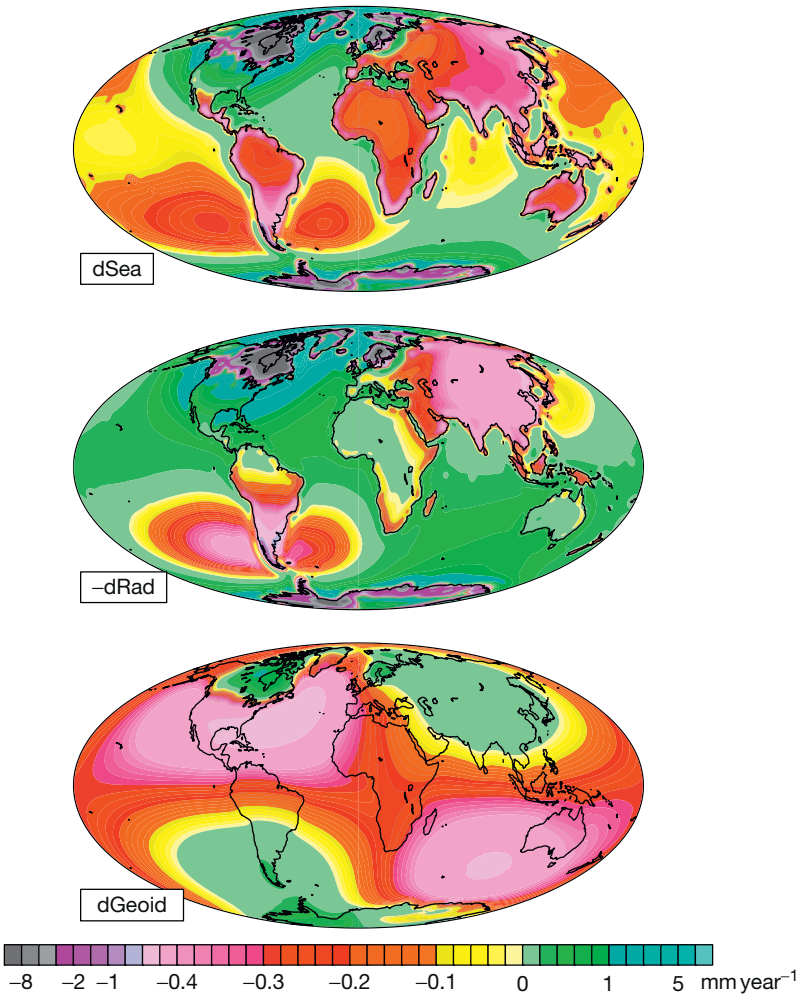

Figure 35 Model ICE-6G (VM5a) results for the present-day rate of relative sea-level rise (dSea), the present-day rate of radial displacement of the Earth's crust (dRad), and the present-day rate of change of geoid height (dGeoid). Notable is the fact that dRad is negatively correlated with dSea. dGeoid is simply the sum of dSea and dRad.

density $\nu(\theta,\lambda,t)$, which includes both the ice component and the bathymetry component such that

$$L(\theta,\lambda,t)=a^2\sum_{l=0}^{\infty}\sum_{m=-l}^{+l}\nu_{lm}(t)Y_l^m(\Omega) \qquad [52]$$

in which the spherical harmonics are as in Peltier et al. (2012). If the Earth were entirely rigid, this time-dependent surface mass load would correspond to variations of the elements of the moment of inertia tensor as follows:

$$\begin{aligned}I_{ij}^{\text{Rigid}}(t)&=\int\nu(\theta,\lambda,t)\left(a^2\delta_{ij}-x_ix_j\right)a^2\mathrm{d}\Omega,\ \nu(\theta,\lambda,t)\\&=\sum_{l=0}^{\infty}\sum_{m=-l}^{+l}\nu_{lm}(t)Y_l^m(\theta,\lambda)\\&\quad x_x=a\sin\theta\cos\lambda,\ x_y=a\sin\theta\sin\lambda,\ x_z=a\cos\theta,\\&\quad \mathrm{d}\Omega=\sin\theta\mathrm{d}\theta\mathrm{d}\lambda\end{aligned} \qquad [53a]$$

So that

$$\begin{aligned}I_{xz}^{\text{Rigid}}-iI_{yz}^{\text{Rigid}}&=-a^4\iint_{\Omega}\nu(\theta,\lambda,t)\sin\theta\cos\theta e^{-i\lambda}\mathrm{d}\Omega\\&=-a^4\iint_{\Omega}\nu(\theta,\lambda,t)\left[\sqrt{2/15}\overline{P}_2^1(\cos\theta)\right]e^{-i\lambda}\mathrm{d}\Omega\\&=-\sqrt{2/15}a^4\sum_{l=0}^{\infty}\sum_{m=-l}^{+l}\nu_{nm}(t)\iint_{\Omega}Y_l^m(\Omega)Y_2^{1^*}(\Omega)\mathrm{d}\Omega\\&=-4\pi a^4\sqrt{2/15}\sigma_{21}\end{aligned} \qquad [53b]$$

And thus,

$$4\pi a^4\nu_{21}(t)=-\sqrt{15/2}\left[I_{xz}^{\text{Rigid}}-iI_{yz}^{\text{Rigid}}\right] \qquad [53c]$$

For the total inertia components, we have, as discussed in detail previously, $I_{xz}^{\text{Tot}}=I_{xz}^{\text{Load}}+I_{xz}^{\text{Rot}}$. A similar expression holds for I_{yz}^{Tot}. We may rewrite the geoid equation [39] in two distinct ways, either as a sum of parts that derive from a spherical harmonic expansion in terms of complex spherical harmonics or in the form of an expansion in terms of real spherical harmonics, the latter form being that in which the conventional Stokes coefficients appear directly, as follows:

$$\begin{aligned}G(\theta,\lambda,t)&=G^{\text{Load}}(\theta,\lambda,t)+G^{\text{Rot}}(\theta,\lambda,t)\\&=\sum_{l=0}^{\infty}\sum_{m=-l}^{+l}G_{lm}Y_l^m(\theta,\lambda)\end{aligned} \qquad [54a]$$

or

$$G(\theta,\lambda,t)=a\sum_{l=0}^{\infty}\sum_{m=0}^{+l}[C_{lm}\cos(m\lambda)+S_{lm}\sin(m\lambda)]P_{lm}(\cos\theta) \qquad [54b]$$

By investigating the first two terms (load and rot) of the geoid function, equivalent contributions to the Stokes coefficients $C_{21}^{\text{Load}}, C_{21}^{\text{Rot}}$, and $S_{21}^{\text{Load}}, S_{21}^{\text{Rot}}$ can be obtained. This simply involves multiplication of eqn [54a] by the spherical harmonic $Y_2^{1^*}(\theta,\lambda)$, followed by the application of the orthogonality relation of the spherical harmonics themselves to determine a posteriori expressions for C_{21} and S_{21}. Since this procedure eliminates any influence of the space-independent mass conservation term from either of these expressions, insofar as these Stokes coefficients are concerned, this term has no influence.

We proceed, in what follows, to document the expressions for the two Stokes coefficients that are obtained by following this procedure and will deal separately with the contributions from the load and from the varying rotation, beginning with the former.

9.09.6.2.1 The load contribution

We obtain the load component of the space–time dependence of geoid height as

$$\begin{aligned}G^{\text{Load}}(\theta,\lambda,t)&=\int_{-\infty}^{t}d\tau\iint_{\Omega}\mathrm{d}\Omega'\left\{L(\theta',\lambda',\tau)G_G^L(\theta',t-\tau)\right\}\\&=\frac{a}{M_e}a^2\int_{-\infty}^{t}\mathrm{d}\tau\sum_{l=0}^{\infty}\sum_{m=-l}^{+l}\frac{4\pi}{(2l+1)}\sigma_{lm}(\tau)\\&\quad\left\{\delta(t-\tau)+k_l^L(t-\tau)\right\}Y_l^m(\Omega)\end{aligned} \qquad [55]$$

where we have employed the addition theorem for spherical harmonics (eqn [48]) and the orthogonality relation among spherical harmonics to eliminate the surface integral. Carrying the temporal convolution integral through this expression then delivers

$$\begin{aligned}G^{\text{Load}}(\theta,\lambda,t)&=\frac{1}{M_e}\sum_{l=0}^{\infty}\sum_{m=-l}^{+l}\frac{4\pi a^3}{(2l+1)}\\&\quad\{\nu_{lm}(t)+\int_{-\infty}^{t}\nu_{lm}(\tau)k_l^L(t-\tau)\}Y_l^m(\theta,\lambda)\end{aligned} \qquad [56]$$

We may extract the degree 2 and order 1 term from this equation by the application of the orthogonality condition once more, which leads to the following expression:

$$G_{21}^{\text{Load}}=\frac{1}{M_ea}\frac{4\pi a^4}{5}\left\{\nu_{21}+k_2^L{*}\nu_{21}\right\} \qquad [57]$$

Using the results in Section 9.09.3.5 transforms this expression into one involving the 'rigid' contributions to the moment of inertia tensor and thence to the total load components of the moment of inertia tensor as

$$\begin{aligned}G_{21}^{\text{Load}}&=\frac{-1}{M_ea}\sqrt{\frac{3}{10}}\left\{\left[I_{xz}^{\text{Rigid}}-iI_{yz}^{\text{Rigid}}\right]+k_2^L{*}\left[I_{xz}^{\text{Rigid}}-iI_{yz}^{\text{Rigid}}\right]\right\}\\&=\frac{-1}{M_ea}\sqrt{\frac{3}{10}}\left[I_{xz}^{\text{Load}}-iI_{yz}^{\text{Load}}\right]\end{aligned} \qquad [58]$$

Expressed in terms of the Stokes coefficients, this is equivalent to

$$\begin{aligned}\left[C_{21}^{\text{Load}},S_{21}^{\text{Load}}\right]&=g_1\left[\frac{I_{xz}^{\text{Load}}}{(C-A)},\frac{I_{yz}^{\text{Load}}}{(C-A)}\right]\ \text{where}\ g_1\\&=-\sqrt{\frac{3}{5}}\left[\frac{(C-A)}{M_ea^2}\right]\end{aligned} \qquad [59]$$

9.09.6.2.2 The rotational contribution

This is the most important part of this analysis. In parallel with eqn [55], we may write

$$G^{Rot}(\theta,\lambda,t) = \int_{-\infty}^{t} d\tau \iint_{\Omega} d\Omega'\ \Psi^{R}(\theta',\lambda',\tau)\ {}_{R}G_{G}^{T}(\phi,t-\tau) \quad [60]$$

where Ψ^R is defined in eqns [13]. We again invoke the addition theorem to expand the tidal Green function in reducing eqn [60], but now, the appearance of the renormalization factor in the definition of the Green function eliminates the factor $4\pi/(2l+1)$ that would otherwise appear. Taking this into account, eqn [60] may be expanded as

$$\begin{aligned} G_{21}^{\mathrm{Rot}} &= \frac{1}{g}\int_{-\infty}^{t}\left\{\delta(t-\tau)+k_2^T(t-\tau)\right\}\Psi_{21}(\tau)\mathrm{d}\tau \\ &= -\frac{\Omega^2 a^2}{g}\sqrt{\frac{1}{30}}\left\{\left[m_x(t)-im_y(t)\right]+k_2^{T}*\left[m_x(t)-im_y(t)\right]\right\} \\ &= -\frac{\Omega^2 a^2}{g}\sqrt{\frac{1}{30}}\left\{\frac{\left[I_{xz}^{\mathrm{Tot}}-iI_{yz}^{\mathrm{Tot}}\right]}{(C-A)}+k_f\frac{\left[I_{xz}^{\mathrm{Rot}}-iI_{yz}^{\mathrm{Rot}}\right]}{(C-A)}\right\} \end{aligned} \quad [61]$$

where Ψ_{21} is taken from eqn [13], and the results of **Section 9.09.3.5** are used to obtain the final line in eqn [61]. Invoking the known relationships between the coefficients in the expansion of a field in terms of real spherical harmonics and those in the expansion of the same field in complex spherical harmonics, as in the preceding text, we have

$$\left[C_{21}^{\mathrm{Rot}},S_{21}^{\mathrm{Rot}}\right] = g_2\left[\frac{\left(I_{xz}^{\mathrm{Rot}}+I_{xz}^{\mathrm{Tot}}/k_f\right)}{(C-A)},\frac{\left(I_{yz}^{\mathrm{Rot}}+I_{yz}^{\mathrm{Tot}}/k_f\right)}{(C-A)}\right]$$

$$\text{where } g_2 = -\frac{\Omega^2 a k_f}{3g}\sqrt{\frac{3}{5}} \quad [62]$$

As discussed in Peltier et al. (2012), the $\delta(t-\tau)$ term in eqn [55] should not appear in eqn [61] if the purpose of the GIA-predicted geoid is to be compared with observations being provided by the GRACE satellites as an Earth-orbiting satellite makes measurements from an inertial frame of reference and is therefore incapable of observing an impact upon the geoid that is derivative of the direct effect of the inertial force that this term represents. However, since the physical geoid is related to sea level and since the ocean is attached to the rotating Earth, the water in the ocean basins does feel the centrifugal force and there is a component of the physical geoid that GRACE is unable to observe. As we will see, the fact that GRACE observes only an approximation to the geoid defined in terms of sea level introduces a difference between the inferred Stokes coefficients for the actual geoid such that the latter are larger than the former by a factor of ~2.

9.09.6.2.3 The total degree 2 and order 1 Stokes coefficients

Therefore, according to the SLE, $\dot{C}_{21},\dot{S}_{21}$ are related to the products of inertia in the following way:

$$\begin{aligned} \dot{C}_{21} &= g_1\left(\frac{I_{xz}^{\mathrm{Load}}}{(C-A)}\right)+g_1\left(\frac{I_{xz}^{\mathrm{Rot}}}{(C-A)}\right)+\frac{g_2}{k_f}\left(\frac{I_{xz}^{\mathrm{Tot}}}{(C-A)}\right) \\ \dot{S}_{21} &= g_1\left(\frac{I_{yz}^{\mathrm{Load}}}{(C-A)}\right)+g_2\left(\frac{I_{yz}^{\mathrm{Rot}}}{(C-A)}\right)+\frac{g_2}{k_f}\left(\frac{I_{yz}^{\mathrm{Tot}}}{(C-A)}\right) \end{aligned} \quad [63a,b]$$

where the constants of combination in the aforementioned expressions are

$$g_1 = -\sqrt{\frac{3}{5}}\frac{(C-A)}{M_e a^2}\ g_2 = -\sqrt{\frac{1}{15}}\frac{a\Omega_o^2 k_f}{g} \quad [64]$$

The expression for the C_{21} coefficient that follows from the SLE-based geoid eqn [39] is then

$$C_{21} = \left(g_1+\frac{g_2}{k_f}\right)\left(\frac{I_{xz}^{\mathrm{Load}}}{(C-A)}\right)+\left(g_1+\frac{g_2}{k_f}\right)\left(\frac{I_{xz}^{\mathrm{Rot}}}{(C-A)}\right) \quad [65]$$

This expression may be reduced considerably by noting that the ratio g_1/g_2 is simply

$$\begin{aligned} \frac{g_1}{g_2} &= +\sqrt{\frac{3}{5}}\frac{(C-A)}{M_e a^2}\sqrt{\frac{15}{1}}\frac{g}{a\Omega^2 k_f} \text{ but } g=\frac{M_e G}{a^2} \\ \frac{g_1}{g_2} &= +3\frac{(C-A)}{M_e a^3\Omega^2}\frac{1}{k_f}\frac{M_e G}{a^2} \\ \text{and } k_f &= \frac{3G}{a^5\Omega^2}(C-A) \\ \text{so } \frac{g_1}{g_2} &= 1 \\ \text{and } C_{21} &= g_1\left(1+\frac{1}{k_f}\right)\left(\frac{I_{xz}^{\mathrm{Load}}}{(C-A)}+\frac{I_{xz}^{\mathrm{Rot}}}{(C-A)}\right) \end{aligned} \quad [66]$$

with a correspondingly simple result holding for S_{21}. Since the factor $(1+1/k_f)=2.06$ if k_f is taken to be ~0.94, this explains the flaw in the arguments of Chambers et al. (2010) as to the basis on which one should be able to determine the values of the degree 2 and order 1 Stokes coefficients directly from the time dependence of the products of inertia alone.

Insofar as model-predicted values of the individual Stokes coefficients based upon these formulae are concerned, these are as follows for the actual physical geoid when this is defined as the surface of constant gravitational potential that overlaps the surface of the sea in the absence of tides and currents. The results for the ICE-5G (VM2) model are

$$\left(\dot{C}_{21},\dot{S}_{21}\right) = (-0.50,+2.59)E-11\,\mathrm{year}^{-1} \quad [67]$$

Eliminating the $\delta(t-\tau)$ term in eqn [55] and therefore reducing the factor $1+1/k_f$ to unity, the values of these Stokes coefficients for the same model that GRACE would be expected to observe if the GIA process was the only process contributing to these coefficients become

$$\left(\dot{C}_{21},\dot{S}_{21}\right) = (-0.24,+1.24)E-11\,\mathrm{year}^{-1} \quad [68]$$

each of the coefficients therefore being further reduced by a factor of ~2.06. It is also worth noting the values for these Stokes coefficients quoted in the recent paper by Cheng et al. (2011) who acknowledged these as being provided by Wahr as

$$\left(\dot{C}_{21},\dot{S}_{21}\right) = (-0.2,+1.2)E-11\,\mathrm{year}^{-1} \quad [69]$$

These numbers are sufficiently close to those in eqn [37] to suggest that they have also been based upon use of the full ICE-5G (VM2) model of Peltier (2004). It is also important to note that the values being circulated are clearly not based upon the use of the formulation of the rotational response theory advocated in Mitrovica et al. (2005), which would reduce them to a further significant degree if it were assumed that the elastic thickness of a globe encircling lithosphere remained finite in

the limit of infinite time in response to tidal forcing. I view this modification to the 'traditional' form of the rotational response theory with skepticism for the reasons discussed in Peltier and Luthcke (2009) and Peltier et al. (2012).

It will be clear on the basis of the compilation of the GRACE-inferred values of the Stokes coefficients from **Table 2** of Peltier and Luthcke (2009) that neither of these sets of values is particularly close to the theoretically predicted values for the ICE-5G (VM2) model noted in the preceding text. Recapitulating the results listed in this table in Peltier and Luthcke (2009) for the purpose of comparison to those in the preceding text, we have

$$\begin{array}{lll} \text{GSFC}_\text{V}05 & \dot{C}_{21} = -1.65E-11\,\text{year}^{-1} & \dot{S}_{21} = +1.76E-11\,\text{year}^{-1} \\ \text{GSFC}_\text{V}06 & \dot{C}_{21} = -1.47E-11\,\text{year}^{-1} & \dot{S}_{21} = +1.76E-11\,\text{year}^{-1} \\ \text{GSFC}_\text{V}07 & \dot{C}_{21} = -1.68E-11\,\text{year}^{-1} & \dot{S}_{21} = +2.67E-11\,\text{year}^{-1} \\ \text{CSR} & \dot{C}_{21} = -1.80E-11\,\text{year}^{-1} & \dot{S}_{21} = +1.18E-11\,\text{year}^{-1} \\ \text{GFZ} & \dot{C}_{21} = -1.23E-11\,\text{year}^{-1} & \dot{S}_{21} = +0.28E-11\,\text{year}^{-1} \end{array} \quad [70]$$

where GSFC stands for the Goddard Space Flight Center and CSR stands for the Center for Space Research (both are US analysis centers) and GFZ stands for the GFZ German Research Centre in Potsdam. Comparison of these results based upon the 'observations' to those from either version of the theoretical model listed in eqns [36] and [37] will show that the differences are as large as those identified for the earlier less accurate version of the ICE-5G (VM2) model in Peltier and Luthcke (2009). That the accuracy of these GRACE inferences of the degree 2 and order 1 Stokes coefficients should be seen as highly compromised will be clear on the basis of the estimates that follow directly from the recent GRACE epoch analysis of the rotational observables published in Roy and Peltier (2011) that were discussed in **Section 9.09.4.3**. Given the results of this original analysis of the polar wander process in the post-1992 period, based upon the use of a modern Earth orientation data set, applying the results of that section, we obtain

$$\left(\dot{C}_{21}, \dot{S}_{21}\right) = (-0.40, +0.60)E-11\,\text{year}^{-1} \quad [71]$$

which we will take to be the most accurate observations available in what follows. These may be compared to the appropriate version of the model-based results in eqn [63] where it will be seen that there exist substantial differences. There is a factor of 2 difference in $\dot{C}_{21}$ with the observed value being higher than the model-predicted value. There is also a difference in the values of $\dot{S}_{21}$ with the model-predicted value being higher by a factor of 2 than the observed value. In Peltier and Luthcke (2009), it was hypothesized that discrepancies of this kind should be explicable in terms of modern land-ice melting, perhaps augmented (in our current view) by additional forcing due to changing storage of water on the continents. We turn to the construction of a preliminary test of the plausibility of this hypothesis in what follows.

9.09.6.3 GRACE Estimates of the Modern Rate of Land-Ice Melting

Support has recently been forthcoming for the plausibility of this hypothesis in the previously discussed paper by Roy and Peltier (2011). These analyses demonstrate that, beginning in the early 1990s, a decade prior to the launch of GRACE, both of the rotational observables began to deviate sharply from their previously established and Late Quaternary ice-age-controlled rates of secular variation. Of particular interest for present purposes is the fact that the observed rate of polar wander was significantly reduced and the direction shifted significantly to the east of the pre-1990s direction.

Although a refined forward model of the combined influence of the Late Quaternary ice-age cycle and modern land-ice melting will clearly be required to provide definitive proof or refutation of the land-ice melting hypothesis, we have constructed a preliminary forward model that includes the effect of modern land-ice melting and will employ this to fit the post-1992 rotational observations of Roy and Peltier (2011). In order to provide a clear demonstration of the quality of the model that has been most recently developed to serve as basis for such analysis, it is important to first document the fact that, in regions on the Earth's surface that are not influenced by modern land-ice melting but were strongly influenced by ancient ice age, the GIA model is able to make an accurate prediction of the modern hydrology-corrected GRACE observations. To this end, I show in **Figure 36(a)** comparison of the raw and surface hydrology-corrected Grace observations to the predictions of both the ICE-5G (VM2) model of Peltier (2004) and the newly developed ICE-6G (VM5a) model. Several important conclusions follow from the results shown in this figure. First, it will be noted that the correction of the raw GRACE data for the influence of surface hydrologic (groundwater storage) variations is important. Our implementation of this correction is based upon the Global Land Data Assimilation System (GLDAS; Rodell et al., 2004). This correction transforms the raw field into one characterized by a double-bull's-eye pattern with two extrema that straddle present-day Hudson Bay. Comparison of this corrected field to the predictions of the ICE-5G (VM2) model shows that, although the spatial location and amplitude of the GIA-predicted signal are reasonably accurate, this model does not predict the observed double-bull's-eye structure that is characteristic of the hydrology-corrected observations (a caveat is in order here in that the most recent analyses of the GRACE data discussed in Peltier et al. (2014) have shown that the absence of the double-bull's-eye structure from the raw GRACE data arises as a consequence of the application of the correlated error filter that was a necessary step in the data analysis procedure when only a few years of data were available. Given the extended number of years of data now available, this step is no longer necessary, and when it is eliminated, the two bull's-eyes appear in the raw data prior to the application of the hydrological correction). The predictions for the newly constructed ICE-6G (VM5a) model, however, successfully capture this double-bull's-eye structure, and so, this model is a marked improvement over ICE-5G (VM2). This model, the construction of which is fully described in Peltier et al. (2014), has been developed on the basis of the application of a refinement procedure based solely upon the use of GPS observations of vertical motion of the crust. In this procedure, the misfits of the GIA-predicted present-day rates of vertical motion to the GPS observations originally documented in Argus and Peltier (2010) were employed to adjust the thickness versus time history of the Laurentide ice sheet so as to eliminate the misfits to the observations that were characteristic of the ICE-5G (VM2) predictions. The GRACE observations were not themselves

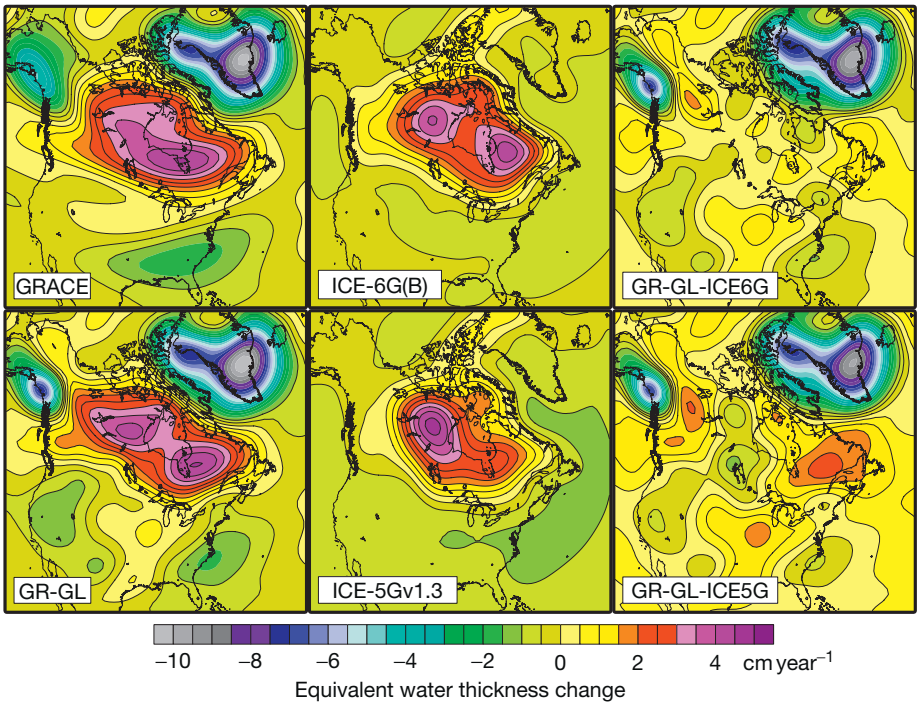

Figure 36 An analysis of the time-dependent gravity observations being provided by the GRACE satellites over the North American continent. The raw GRACE data are denoted 'GRACE,' while the result of filtering of these data to eliminate the influence of surface hydrology is denoted 'GRACE–GLDAS' in which GLDAS stands for the global surface hydrology data set of Rodell et al. (2004). GIA predictions are shown both for the ICE-5G (VM2) model and for the newly constructed ICE-6G (VM5a) model. The latter fields have been stripped of their degree 2 and order 1 Stokes coefficients as have the GRACE and GRACE–GLDAS fields so as to eliminate any ambiguity that might be attributed to the magnitude of the degree 2 and order 1 Stokes coefficients. Also shown are the differences between the two GIA model predictions and the GRACE–GLDAS field. The latter figures illustrate the extent to which the GIA models are able to annihilate the hydrology-corrected GRACE observations. Evident is the fact that the ICE-6G (VM5a) model provides a much improved fit to the observations as it fully explains the 'double-bull's-eye' form of the observations, whereas the ICE-5G (VM2) model does not. Over North America, the adjustment of the Laurentide ice loading history was adjusted to eliminate the misfits to the GPS observations of the ICE-5G (VM2) model identified in Argus and Peltier (2010). The differences between the hydrology-corrected GRACE field and the GIA models isolate the signals over both Greenland and Alaska that are related to global warming-induced land-ice melting.

employed to refine the model. Since the Laurentide ice-sheet complex was by far the most significant at the LGM, the fact that the new ICE-6G (VM5a) model provides such an excellent fit to these observations must be seen to provide a useful independent check on its quality. It should also be noted that in this comparison, the degree 2 and order 0 and the degree 2 and order 1 geoid coefficients are included but the observed coefficients are taken to be equal to those inferred on the basis of the Roy and Peltier (2011) analyses.

Table 2, the first two rows of which were previously discussed in Section 9.09.4.3, lists results for the rotational observables for a series of models of glaciation history including model ICE-6G (VM5aD1) of Peltier and Drummond (2010), which contains no modern land-ice melting and which is one of the models employed for the purpose of previous discussion in this chapter. This model reasonably well fits the pre-1992 values of the nontidal acceleration and the speed and direction of polar wander as previously commented. However, as also noted in the table, it significantly misfits the degree 2 and order 1 Stokes coefficient $\dot{S}_{21}$.although the result for the $\dot{C}_{21}$ coefficient is close to that observed according to the Roy–Peltier inference that is listed in the last row of the table based upon the discussion in the previous subsection. The next model for which results are also listed is for a model denoted 'A' in which only the influence of land-ice melting at the poles is included. These polar sites of regional melting include Alaska, Antarctica, and Greenland, with the rates of melting in each of these regions fixed to those inferred by Peltier (2009) on the basis of GRACE observations. These melting rates (in global sea-level rise equivalents) are 0.12 mm year^{-1} for Alaska, 0.34 mm year^{-1} for Antarctica, and 0.59 mm year^{-1} for Greenland. The influence of modern land-ice melting is added to model ICE-6G (VM5aD1), which includes only the influence of the Late Quaternary ice-age cycle. Inspection of the results for the complete set of rotational observables in this table demonstrates that neither the polar wander speed and direction, nor the $\dot{J}_2$ observation, nor the Stokes coefficients are well fit by this model. This is in spite of the fact that, if one were to

focus solely upon the impact on the nontidal acceleration-related $\dot{J}_2$ parameter and consider only the perturbation to the inferred pre-1992 rate of Roy and Peltier (2011), one would obtain the result shown in the previously discussed **Figure 28** for the perturbation due to the collective effect of all three regions of land-ice melting. Results similar to those in **Figure 28** were recently published in Nerem and Wahr (2011), who apparently believed these to fully explain the shift in the $\dot{J}_2$ observable first identified and ascribed to land-ice melting in Roy and Peltier (2011); but see also Cox and Chao (2002) and Dickey et al (2002). What Nerem and Wahr seem to have missed, however, is that when the influence is added to that of a model that reasonably well fits the pre-1992 values for the rotational observables, the misfits to polar wander speed and direction thereby induced are unacceptable. This fact was fully discussed previously but it is worth reiterating here. Especially important for present purposes, however, is the further increase in the misfits to the Stokes coefficients associated with the parent ice-age-only model ICE-6G (VM5aD1). The observed post-1992 shift in the secular rate of change in the nontidal acceleration cannot therefore be explained by the melting of polar ice from Greenland, Alaska, and Antarctica alone, as the other rotational constraints are then violated.

It is important to note that in these calculations, the full gravitationally self-consistent form of the SLE including rotational feedback has been employed to compute the impact upon all of the rotational observables. Figure 3 of Peltier et al. (2012) illustrates the most important consequence of polar land-ice melting in this regard, in terms of what might be referred to as the 'opposite hemisphere effect.' This figure from that paper shows the results for the sea-level rise that would be caused by the melting of all of the ice on either Greenland or West Antarctica over a period of a century. Notable is the fact that sea-level falls in the immediate vicinity of the land mass from which ice has disappeared and rises dramatically in the opposite hemisphere. This effect was first explored in some of the earliest work involving the use of the SLE formalism (Clark, 1976; Clark and Lingle, 1977). It is crucial to understanding the sea-level teleconnection involved in which the meltwater pulse 1B event due to melting of land ice from Antarctica causes a nonmonotonic rise of sea level at sites once covered by the Scottish ice-sheet complex in the opposite hemisphere.

Returning now to the discussion of the data in **Table 2**, this table also shows results for eight additional models, the first four of which are denoted B, C, D, and E. For these models, additional sources of land-ice melting have been included in the calculation for three of the primary regions in which this process is occurring according to the tabulation in Dyurgerov (2010). These three locations include the mountains of South America, the Himalayan mountains of Asia, and the mountains of western North America, which appear clearly defined in **Figure 37** where they are seen to be the regions of highest topographic relief on the planet. The high topography melt rates assumed for these models are based upon simple scans of hypothetical rates of melting at each of these additional locations in such a way as to test whether it would be possible to fit the new values for the rotational observables inferred by Roy and Peltier (2011) by appropriate choices for them. As shown in the table for models B, C, D, and E, these values of the post-1992 rotational observables are indeed somewhat better fit by these models. Furthermore, as inspection of the results in the table will show, the misfits to the Stokes coefficients estimated on the basis of Roy–Peltier data have also been reduced. The results for the final set of four models in the table are for a simple variation upon models B, C, D, and E in which the radial viscosity profile VM5aD1 is simply replaced by viscosity profile VM5a, which is a simple multilayer approximation to model VM2. For these additional models, the rates of melting are kept fixed to the values assumed for models B, C, D, and E, which are, for the mountains of South America, the Himalayas, and western North America, in global sea-level rise equivalent terms, respectively, 0.72, 0.42, and 0.45 mm year^{-1} for model B; 0.72, 0.37, and 0.47 mm year^{-1} for model C; 0.67, 0.47, and

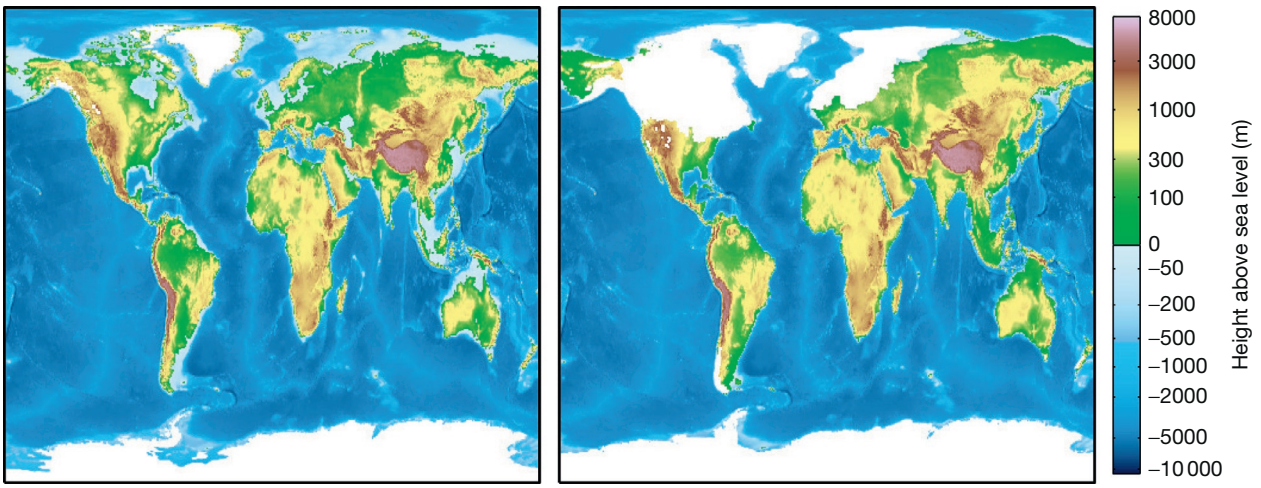

Figure 37 Comparison of surface topography of the non-ice-covered regions of the Earth's surface under modern and LGM surface conditions. Once more, the oceans are depicted in terms of the depth-averaged Brunt–Väisälä frequency. The highest topography regions in this figure, namely, the Himalayas, the Andes, and the North American Cordillera, are the locations at which it is assumed that significant land-ice melting is occurring for the purpose of analyzing the plausibility of the modern land-ice melting hypothesis of Peltier and Luthcke (2009) as an explanation of the rotational data of Roy and Peltier (2011).

0.49 mm year^{-1} for model D; and finally 0.65, 0.47, and 0.50 mm year^{-1} for model E. The final set of four models clearly deliver a very significant further improvement of the quality of fit to the rotational observables and therefore further reduce the misfits to the Roy and Peltier inferred values of the Stokes coefficients. For several of these additional models, the fits are in fact excellent. It is extremely important to note that the total rates of land-ice melting, in eustatic sea-level rise equivalent terms, for models B, C, D, and E, when the contributions from Greenland, Antarctica, and Alaska are included, are respectively, 2.63, 2.60, 2.63, and 2.67 mm year^{-1}. These net rates are in reasonable accord with the constraint on the net rate of global sea-level rise measured by the altimetric satellites Topex/Poseidon and Jason-1/-2 when further adjusted for the steric contribution, a contribution that Cazenave et al. (2009) had inferred to be ~0.37 mm year^{-1} for the GRACE era based upon their analysis of ARGO float data. Church et al (2011), however, had recently quoted a much larger preferred value for the steric contribution of 0.88 ± 0.33 mm year^{-1} and a significantly higher value for the rate of absolute sea-level rise when tide gauge data are employed to augment the basic altimetric observations. It is clear that no consensus has yet emerged on the important issue of sea-level rise budget closure.

My intention in presenting the results of the previously described simple models, based upon the original discussion in Peltier et al. (2012), is nevertheless not to present a fully satisfactory refined model for the melting of small glaciers and ice caps (GICs) but simply to demonstrate that the physical impact of this process could not be ruled out as a possible explanation of any misfit of the ice-age-only model of continental deglaciation to the geoid Stokes coefficients of degree 2 and order 1. Of course, this specific model might be thought to be entirely ruled out based upon the very large geoid anomalies that it predicts over the mountainous regions (not shown), which have no counterpart in the GRACE-observed field of geoid height time dependence. Whether these geoid anomalies could be masked to some (perhaps significant) degree by the continuing uplift of the mountains is an issue that remains to be adequately explored. Furthermore, there clearly exist additional regions of land-ice melting that must be contributing to the current input of freshwater into the global oceans, and their contributions have yet to be inferred with sufficient accuracy. In the next section of this chapter, we shift our focus to additional aspects of the Earth's rotational history, aspects that involve not the planets intrinsic rotation but rather its orbital rotation around the Sun.

9.09.7 The Impact of Variations in the Geometry of the Earth's Orbit Around the Sun upon Climate System Evolution

In the previous sections of this chapter, the focus has been fixed upon the history of the Earth's rotation as observed in the body-fixed coordinate system, the terrestrial fame, in which the anomalies in the variations in the l.o.d. and polar motion are most usefully described. Equally important aspects of the evolution of Earth's rotation, however, are those that are most usefully described in the celestial frame provided by the field of stars of our own and more distant galaxies. In this celestial frame of reference, the orbit of the Earth in its rotation around the Sun is observed to be characterized by subtle time dependence in its geometry. These variations are due to the action of gravitational n-body effects in the solar system that cause the ellipticity of the otherwise Keplerian elliptical orbit to vary with time and similarly impose subtle time dependence upon orbital obliquity, that is to say upon the angle that the spin axis makes with the plane of the ecliptic (see **Figure 38**). As it happens, this aspect of the history of the Earth's rotation exerts a profound effect upon low-frequency climate variability and in particular is the ultimate cause of the Late Quaternary ice-age cycle that has been the focus in several of the preceding sections of this chapter. This so-called astronomical theory of the ice ages, due originally to Milankovitch (e.g., 1940), was finally verified as essentially correct in the seminal paper by Hays et al. (1976) that was based upon the analysis of oxygen-isotopic data from deep-sea sedimentary cores such as the ODP Site 677 data from the Panama Basin shown previously in **Figure 5** and which was analyzed in detail in Shackleton et al. (1990). The origins of the particular time series shown in this figure are in fact extremely important, from the perspective of both our understanding of the Late Pleistocene ice-age cycle and our appreciation of the crucial role that the history of the Earth's rotation has played in our understanding of the detailed characteristics of the process of plate tectonics itself.

Prior to the analysis presented in the Shackleton et al. paper, it had been widely believed, based upon Potassium–Argon dating of the age of the most recent Brunhes–Matuyama reversal of the polarity of Earth's magnetic field, that this event had occurred ~730 000 years before present. This assumed age was, until the appearance of this paper, universally employed in the construction of the chronology of all of the deep-sea

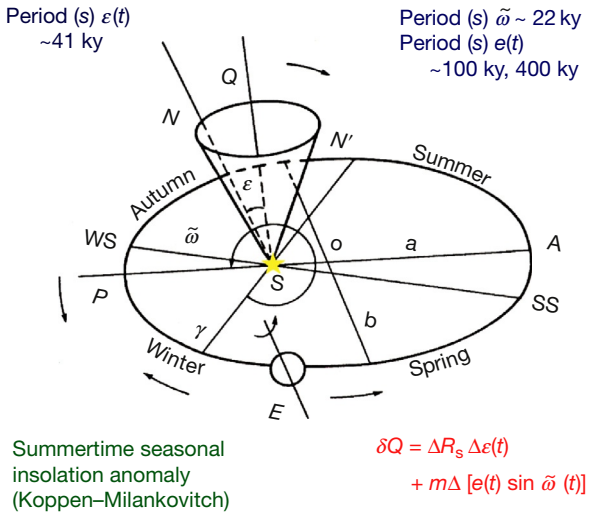

Figure 38 Geometry of the Earth's orbit around the Sun depicting the present positions of the apogee and the perigee, as well as the summer and winter solstices and the spring and autumn equinoxes. The tilt of the spin axis with respect to the plane of the ecliptic is represented by the parameter 'ε,' whereas the eccentricity of the orbit is represented by the parameter 'e.' As a consequence of the influence of the precession of the spin axis in space, the position of the equinoxes and solstices rotates around the orbital ellipse with a period of ~22 000 years.

sedimentary cores that were employed as constraints upon the understanding of climate system processes over the Pleistocene epoch. This date was also employed to constrain the speeds with which oceanic plates were assumed to 'spread' away from oceanic ridge crests in response to the underlying mantle convection process. The history of the process that led to our present understanding that the age of this critical control point for planetary chronology was 780 000 years rather than 730 000 years is important from the perspective of our appreciation of the role that the Earth's rotation history plays in our understanding of the system and so is worth reviewing in some detail.

9.09.7.1 The Astronomical Imprint on Oxygen-Isotopic Records from Deep-Sea Sedimentary Cores

Basic to this understanding is an appreciation of the extent to which modern astrophysical theory has been successful in the reconstruction of the evolving geometry of the Earth's orbit around the Sun over the past several million years of Earth history. Early work on this problem was reviewed and significantly extended by Laskar (1988) who employed a mixture of analytic and numerical techniques to demonstrate that it was possible to perform stable integrations of the geometry of the orbit that extended in excess of several million years into the past. These reconstructions were tested by performing brute force initial value integrations, starting from a modern ephemeris, of the system of gravitational n-body equations governing the evolution of the entire solar system, a system of equations that included an accounting for tidal interactions among the planets and their satellites and for relativistic effects. The results of such brute force integrations were first described in an important paper by Quinn et al. (1991). These analyses demonstrated that the solution of Laskar (1988) was highly accurate and could therefore be employed with confidence to accurately predict the variation of the strength of the solar insolation received by the Earth in the course of its orbit around the Sun as a function of time and as a function of latitude. Earlier predictions of these variations produced by Berger (e.g., 1978) were thereby shown to become inaccurate prior to ~ 1 million years before present. The numerical reconstructions of the evolving geometry of the Earth's orbit consist of predicted time series for the evolution of orbital ellipticity and orbital obliquity. From these quantities, one may compute the latitude-dependent summertime seasonal anomaly in solar insolation received at the top of the atmosphere that is presumed to drive the glaciation–deglaciation process according to the Koppen–Milankovitch hypothesis on the basis of the expression

$$\delta Q(\theta, t) = \Delta R_s(\theta)\Delta\varepsilon(t) + m(\theta)\Delta\left[e(t)\sin\left(\tilde{\omega}t\right)\right] \qquad [72]$$

in which $\delta Q(t)$ is the deviation, in watts per square meter, of the insolation received at the surface of the Earth during the summer season relative to the average of summer insolation over, say, the timescale of the entire 900 000-year period during which the 100 000-year ice-age cycle has been an active element of climate system evolution. The first recognition of the existence of the essentially 100 000 year periodic ice-age cycle was recorded in the paper of Broecker and van Donk (1970). The latitude dependence of the summertime seasonal insolation anomaly is introduced through the quantities $\Delta R_s(\theta)$ and $m(\theta)$, whereas the time dependence is governed by the variation in orbital obliquity $\Delta\varepsilon(t)$ and time-dependent eccentricity of the orbit $e(t)$, which enters the expression for the insolation anomaly only through a modulation of the influence of orbital precession, which occurs at an angular frequency $\tilde{\omega}$ due to the same oblateness of the figure of the Earth that is modulated so effectively by the ice-age cycle to produce variations in the l.o.d. This phenomenon of orbital precession is caused by the action of the gravitational field of the Sun upon the oblate form of the planet whose spin axis is tilted with respect to the ecliptic plane. Figure 39 illustrates the variation with time of the individual elements that appear in eqn [72] in the preceding text, whereas Figure 40 shows the actual distribution of the received insolation over the surface of the Earth as a function of latitude and time of year, both for the present day and for the deviations from this distribution at several fiducial times over the most recent 100 000-year cycle of Late Pleistocene glaciation. Inspection of the distribution of the anomaly for 116 000 years before present at the onset of the most recent of these cycles of continental ice-sheet expansion demonstrates that this event was in fact apparently triggered by a high-latitude summertime seasonal insolation anomaly of magnitude in excess of 60 $\mathrm{W\,m^{-2}}$, in accord with expectations based upon the Milankovitch hypothesis. At LGM itself, the deviation of the insolation regime from that characteristic of present climate was actually rather small. During the mid-Holocene interval centered upon 6 ka, the nature of the insolation forcing was such that the northern-hemisphere continents would have been anomalously warm during the summer season, thus explaining the increased intensity of the summer monsoon circulations that were characteristic of the atmospheric general circulation at that time. Figure 41 compares the power spectrum of the oxygen isotope anomaly from deep-sea core ODP Site 677 to the power spectrum of the summertime seasonal insolation anomaly at 60° N latitude for both the first and last million years of the Pleistocene epoch. Inspection of this intercomparison will show that the power in the insolation forcing at the 100 000-year period on which the continental ice sheets expand and contract is negligible. The implications of this comparison are profound as it provides a direct demonstration of the intensity of the nonlinearity of the climate system that is involved in converting the incoming insolation signature into the climate response. It is only through the action of such nonlinearity that the system may feel the effect of the 100 000-year modulation of the influence upon received insolation due to the effect of orbital precession that arises from the variation of orbital eccentricity. Precisely what the origin is of this nonlinearity remains a subject of intense debate, but it may be connected to the cause of the covariation of atmospheric carbon dioxide with continental ice volume that is so clearly revealed in the Vostok ice core from the continent of Antarctica (e.g., see Jansen et al. (2007) for a detailed discussion of the ice core records and Shackleton (2000) for a discussion of the phase relationships between the atmospheric carbon dioxide record and the ice-volume record.

9.09.7.2 'Orbital Tuning' and the Age of the Brunhes–Matuyama Geomagnetic Polarity Transition

Given this background, we may proceed to consider the analyses that led to the redating of the oxygen-isotopic record from ODP Site 677 that has played such an

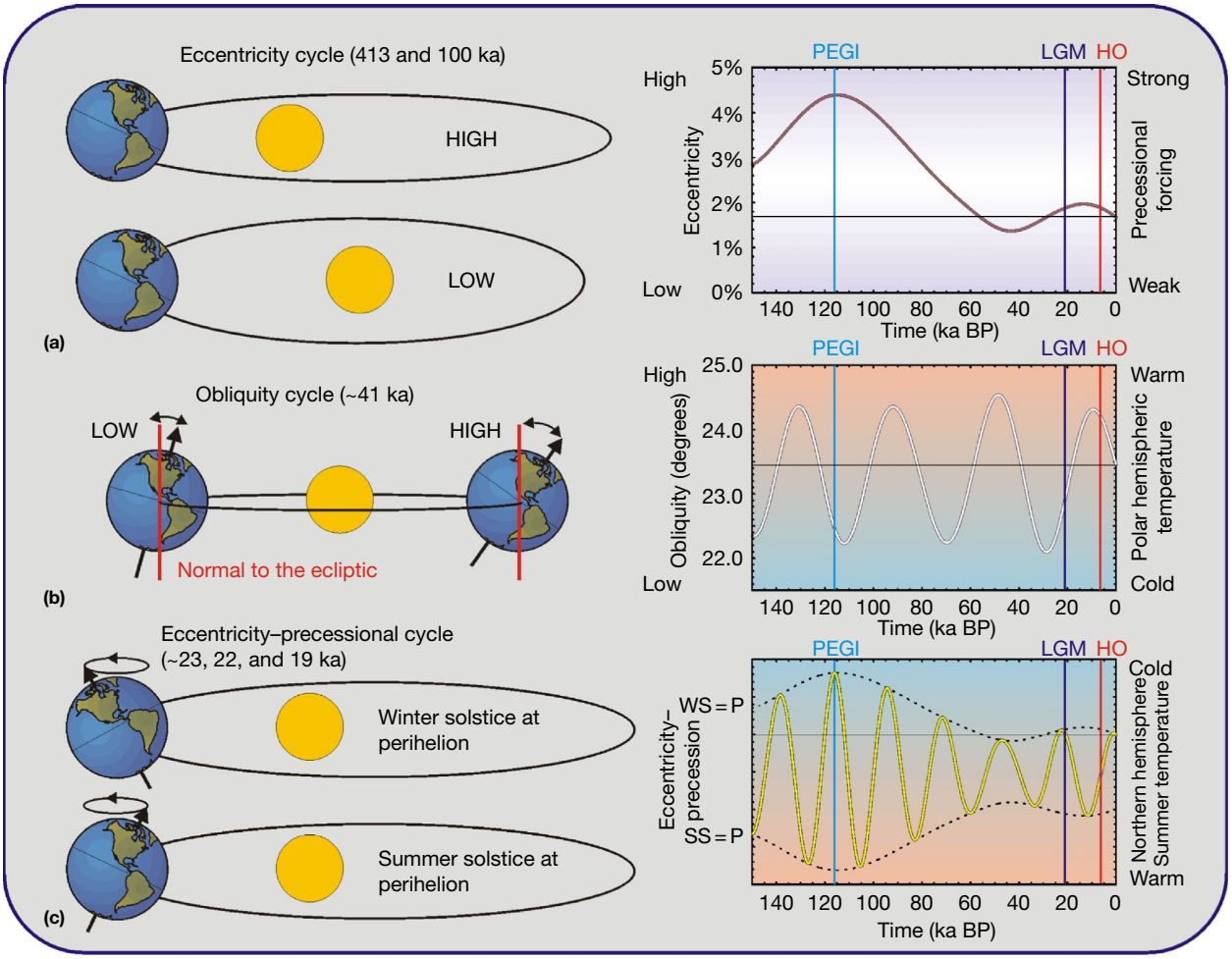

Figure 39 Evolution with time, over the most recent 100 000-year cycle of Late Pleistocene climate variability, of the parameters that control the variation of the solar insolation received at the top of the atmosphere.

important role in revising our understanding of the Pleistocene timescale. Figure 43 shows the original depth versus timescale that was originally ascribed to this core by Shackleton (personal communication in 1988 when the data were passed to the present author for analysis). Notable is the 'dogleg' in this relationship that is apparently near the then assumed age of 730 000 years of the Brunhes–Matuyama transition that was widely accepted as correct at that time. Based upon the assumption of the validity of the Milankovitch hypothesis, the depth–age relationship for this core was refined in Toronto by applying the following strategy. First, the relationship between depth in the core and calendar year age was refined by applying a band pass filter to the isotopic time series with a central frequency equal to that of the obliquity timescale of 41 000 years, and the depth–time relationship was adjusted iteratively so as to maximize the coherence between the astronomical forcing at this period and the ice-volume response. Next, the same process was applied to the variability in the eccentricity–precession band in which the modulation of the precession effect due to the eccentricity variation occurs. Once more, the age–depth relationship was adjusted in order to optimize the coherence between astronomical signal and ice-volume response. The frequency-domain form of the band pass filters employed in this analysis together with the power spectrum of the oxygen isotope time series is shown in Figure 42. The process of refinement of the age–depth relationship was continued by returning to the obliquity band and then returning to the eccentricity–precession band until an entirely stable result was obtained. The new age–depth relationship for the 677 core is also shown in Figure 42 as the dashed line labeled model II where it is observed to correspond to a very nearly linear relationship between depth and age, suggesting that in fact, the sedimentation rate at this site had been very nearly constant throughout the entire Pleistocene interval. The initial depth–age model provided to the author by N. J. Shackleton is shown as model IV. The models denoted I and III on the figure are intermediate results obtained in the iterative sequence of steps in the 'orbital tuning' process. The quality of the fits between the astronomical forcing and ice-volume response records in the two pass bands employed in the application of this methodology is shown in Figure 44(a) and 44(b), respectively, where a very nearly precise agreement was obtained (see Peltier (1996a) in which the

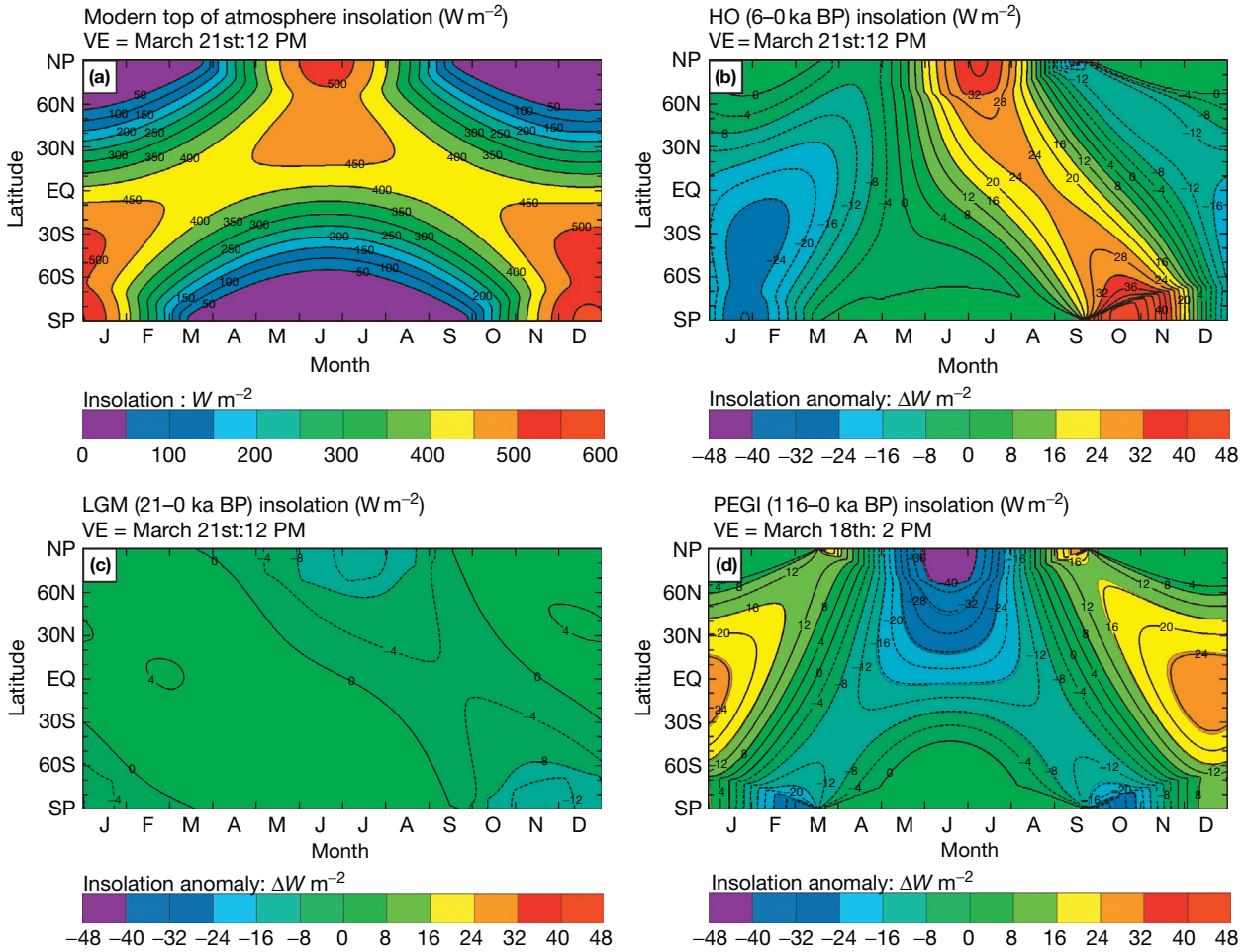

Figure 40 Distribution of solar insolation received at the top of the atmosphere as a function of time of year and latitude for three different epochs. (a) shows the present-day distribution, whereas (b)–(d) respectively show the deviation from the modern distribution for the mid-Holocene warm period at 6000 years before present, for Last Glacial Maximum at ~21 000 years before present, and for the end of the Eemian interglacial at 116 000 years before present, the time during which the extremely strong negative summertime seasonal insolation anomaly existed that was responsible for the onset of the most recent 100 000-year glacial cycle.

original results that led to the paper by Shackleton et al. (1990) were eventually first published).

This analysis suggested that there must have been an error in the previously accepted age of the Brunhes–Matuyama transition in the polarity of the Earth's magnetic field, with the actual age of the transition being very close to 780 000 years rather than to the originally assumed age of 730 000 years, a difference of ~7% or 50 000 years. In the paper by Shackleton et al. (1990), the initial Toronto result was checked against a large number of other oxygen-isotopic records from deep-sea cores and found to be reproducible in every instance. Very soon after the appearance of the Shackleton et al. publication and in response to it, the age of the Brunhes–Matuyama transition was redated using the argon 39–argon 40 method by Baksi (1992) whose analysis immediately confirmed the validity of the new age for this most recent polarity transition in the Earth's magnetic field, an age that had been determined by the application of the 'orbital tuning' methodology. It should be clear that this combination of results has served to fully verify the validity of our present understanding of the Late Pleistocene ice-age cycle as being caused by the history of the variations in the geometry of the Earth's rotation around the Sun.

9.09.8 The Earth's Rotation Variations, Mantle Convective Mixing, and Plate Tectonics-Related Processes

On the ultra-long timescales on which the planet evolves thermally, it remains very useful to continue to discuss the variations in the Earth's intrinsic rotational state in terms of variations in the l.o.d and variations of the position of the poles with respect to a body-fixed coordinate system. On such long timescales, the mantle convection process leads to a continuous reorganization of the land-sea distribution as the continents are caused to 'drift' over the surface of the Earth. Because this drift is associated with changes in all of the elements of the moment of inertia tensor of the planet, in consequence, a reaction of the rotational state in both l.o.d. and polar motion

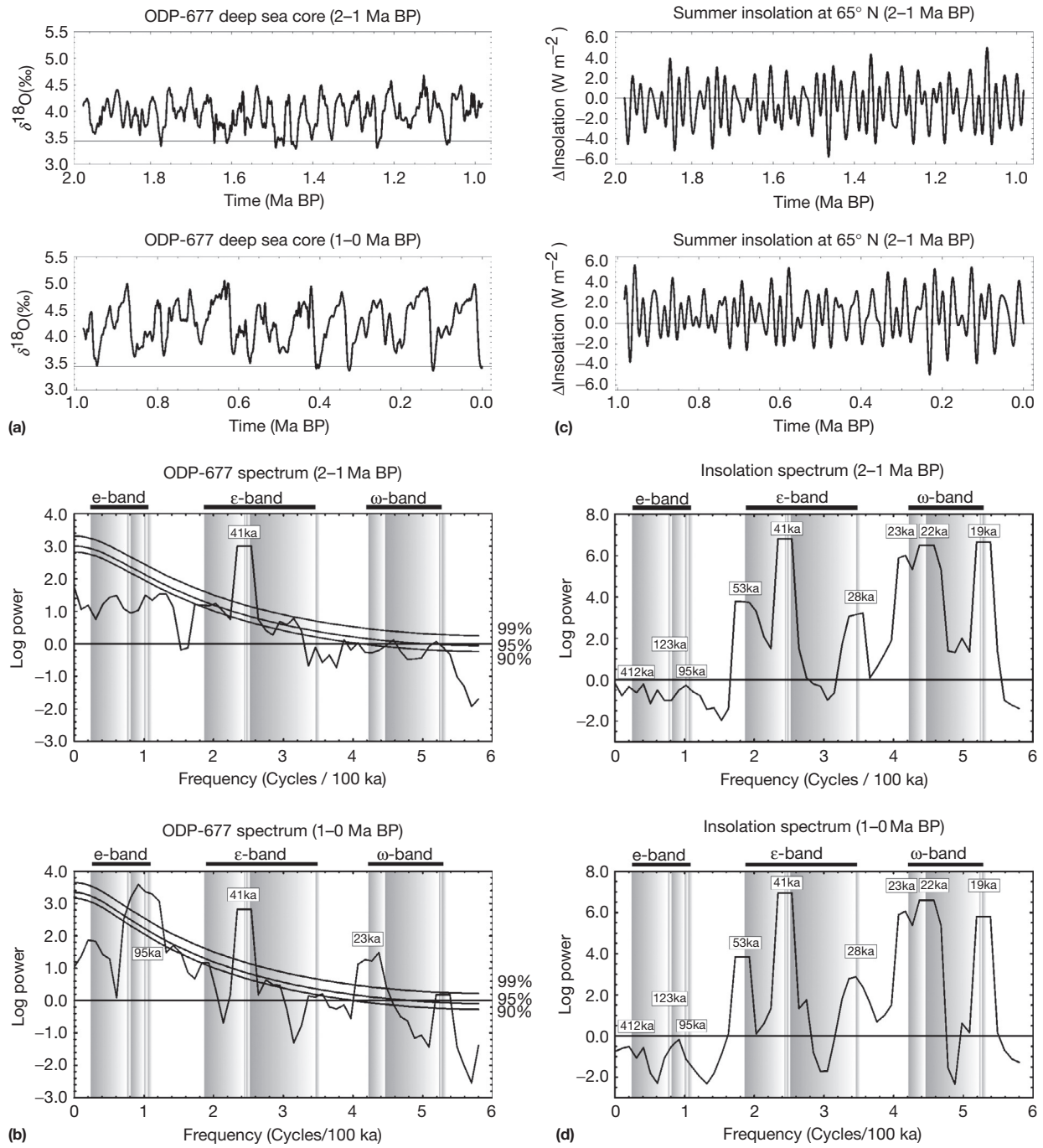

Figure 41 Intercomparison of the oxygen-isotopic time series from ODP Site 677 and its power spectrum to the time series and power spectrum of the solar insolation forcing for both the first and last million years of these records. Notable is the extremely weak insolation forcing at the period of 100 000 years, which is the period at which the climate system response is strongest.

is produced. At least equally important from the former perspective, however, are the changes in the l.o.d. that occur as an indirect consequence of the continuous rearrangement of the continent ocean distribution. This additional physical effect acts through the dissipation of the tides raised in the oceans, primarily by the gravitational attraction of the Moon, which is the origin of the tidal deceleration of rotation previously discussed. In what follows, I will provide a brief discussion of the current state of understanding of each of these additional sources of rotational excitation, beginning with the latter.

9.09.8.1 Tidal Despinning of the Earth's Rate of Axial Rotation: Tidal Rhythmites and the l.o.d.

Although space limitations mitigate against providing a detailed review of this important very long-timescale

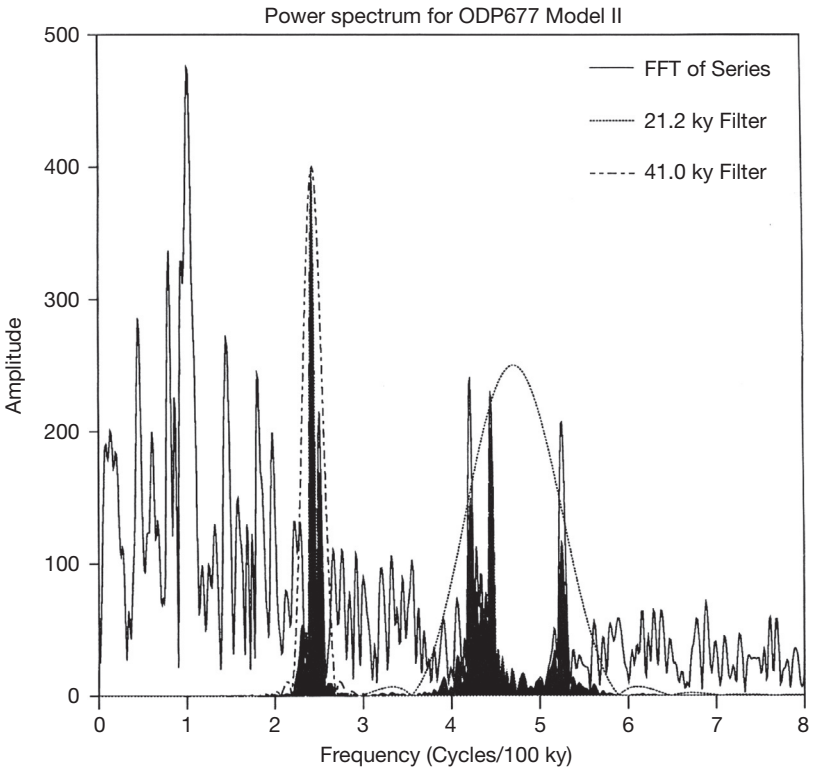

Figure 42 Frequency-domain forms of the band pass filters employed in the Toronto application of the orbital tuning methodology to the $\delta^{18}O$ record from ODP Site 677.

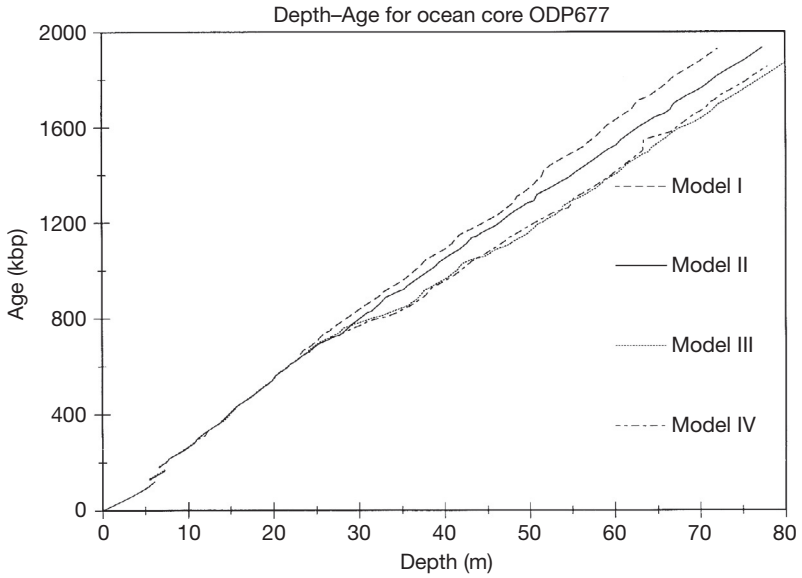

Figure 43 Oxygen-isotopic record from ODP Site 677 as originally provided by N. J. Shackleton to the writer in 1988 on the depth versus timescale constrained to fit the assumed age of 730 000 years of the Brunhes–Matuyama geomagnetic reversal. Notable in the original record is the 'dogleg' that was forced to occur in the depth–time relationship by virtue of this assumption. Also shown in the figure are the revised depth–time relationships deduced by 'orbital tuning' of this record that was accomplished at the University of Toronto and that led to the prediction of the necessity of revising the age of this geomagnetic reversal.

mechanism through which highly significant secular changes in the l.o.d. occur, namely, through the action of ocean tidal friction alone, it will be important to at least record the fact that such changes are large and that there exist extremely useful observations that can be brought to bear upon the problem. Although the problem of the ocean tides has a long and distinguished history of investigation in the geophysical sciences, it remains an active area of investigation as a consequence of

the need to develop a much more detailed understanding of tidal dissipation. This dissipation acts through two distinct mechanisms, namely, through bottom friction and through the dissipation associated with the breaking of the internal tide that is generated by the interaction of the barotropic tide with bottom topography in the stably stratified abyssal ocean (e.g., see Griffiths and Peltier (2008, 2009) and Salehipour et al (2013)). As a consequence of the action of both contributions to the net dissipation, the tidal bulge in the oceans raised by the gravitational attraction of the Moon is phase-delayed, and so, the spin angular momentum of the planet is subjected to a net torque, which decreases the rotation rate (see **Figure 45**).

Because of the dominant control that the semidiurnal M_2 tide in the oceans exerts upon coastal marine sedimentologic processes, it has been possible on the basis of the study of 'tidal rhythmites' to infer what the l.o.d. has been at certain epochs in the distant past. For example, in Williams (1997, 1998, 2000), analyses are described of South Australian sequences for the Late Neoproterozoic (~620 million years before present, near the time of the Marinoan glaciation) that indicate a rotational state characterized by 13.1 ± 0.1 synodic (lunar) months per year, 400 ± 7 solar days per year, and a l.o.d. of 21.9 ± 0.4 h. **Figure 46**, from Williams (1998), shows an example of the subtle banding characteristic of the rhythmites of the Elatina Formation. He also inferred on the basis of these data a mean rate of lunar recession since that time of 2.17 ± 0.31 cm year^{-1}, slightly more than half the present-day rate of lunar recession of 3.82 ± 0.07 cm year^{-1} obtained on the basis of lunar laser ranging, as discussed previously in **Section 9.09.4.1** of this chapter. **Figure 47** illustrates the manner in which the sedimentary sequences in the rhythmite may be translated into information that can be interpreted quantitatively to infer these numerical results. Similar data from earlier epochs are also discussed in Williams (2000) review paper and are illustrated in **Figure 48**, which suggest that a close approach of the Moon to the Earth would not have occurred during the entire Proterozoic aeon (2450–620 Ma). These results are clearly important for our understanding of the origin of the Moon and of the processes that control tidal friction. The current configuration of the ocean basins is such

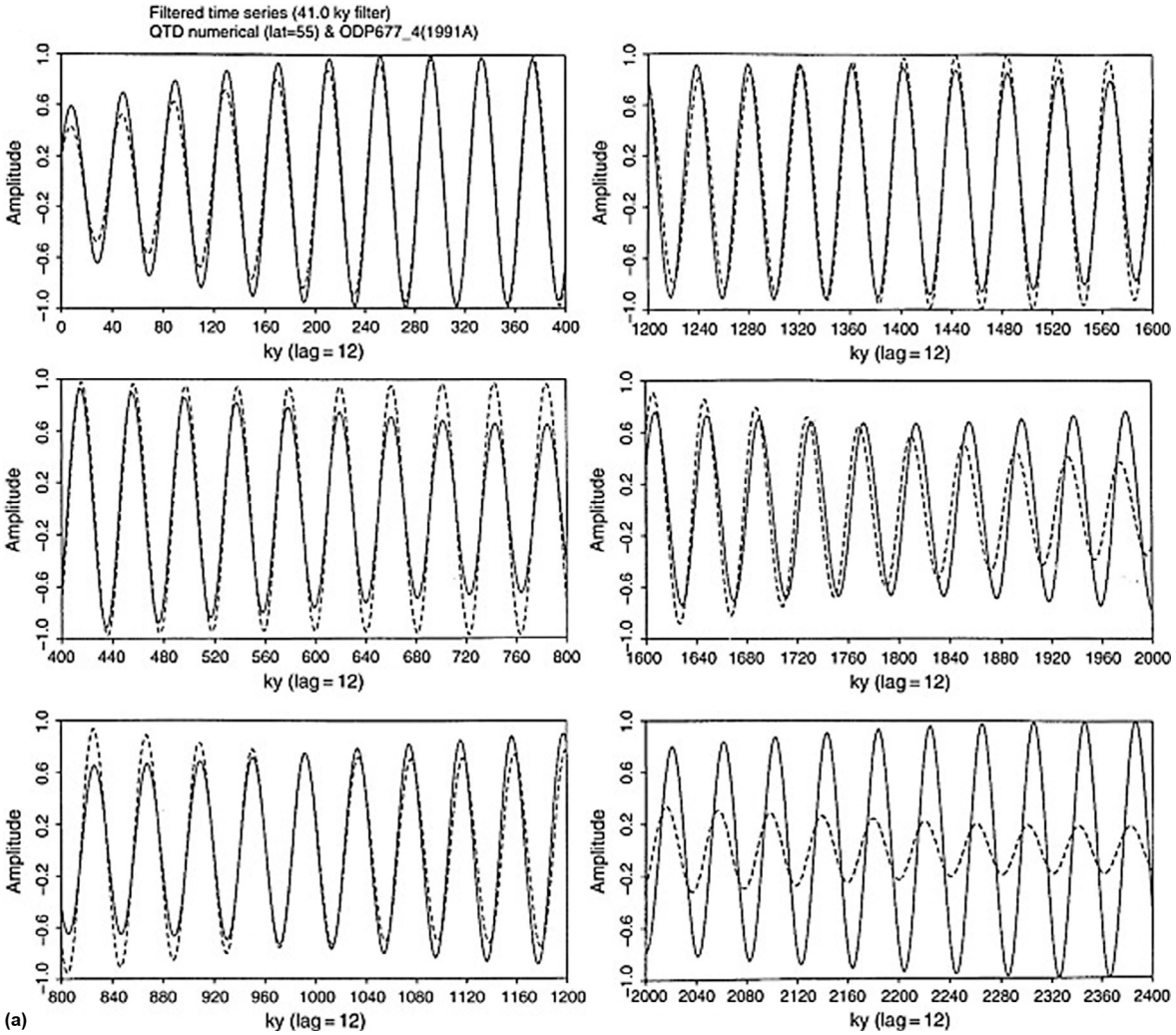

Figure 44 (a) Coherence between the astronomical forcing at the period of 41 000 years and the oxygen-isotopic variability at the same period after orbital tuning at the University of Toronto.

(Continued)

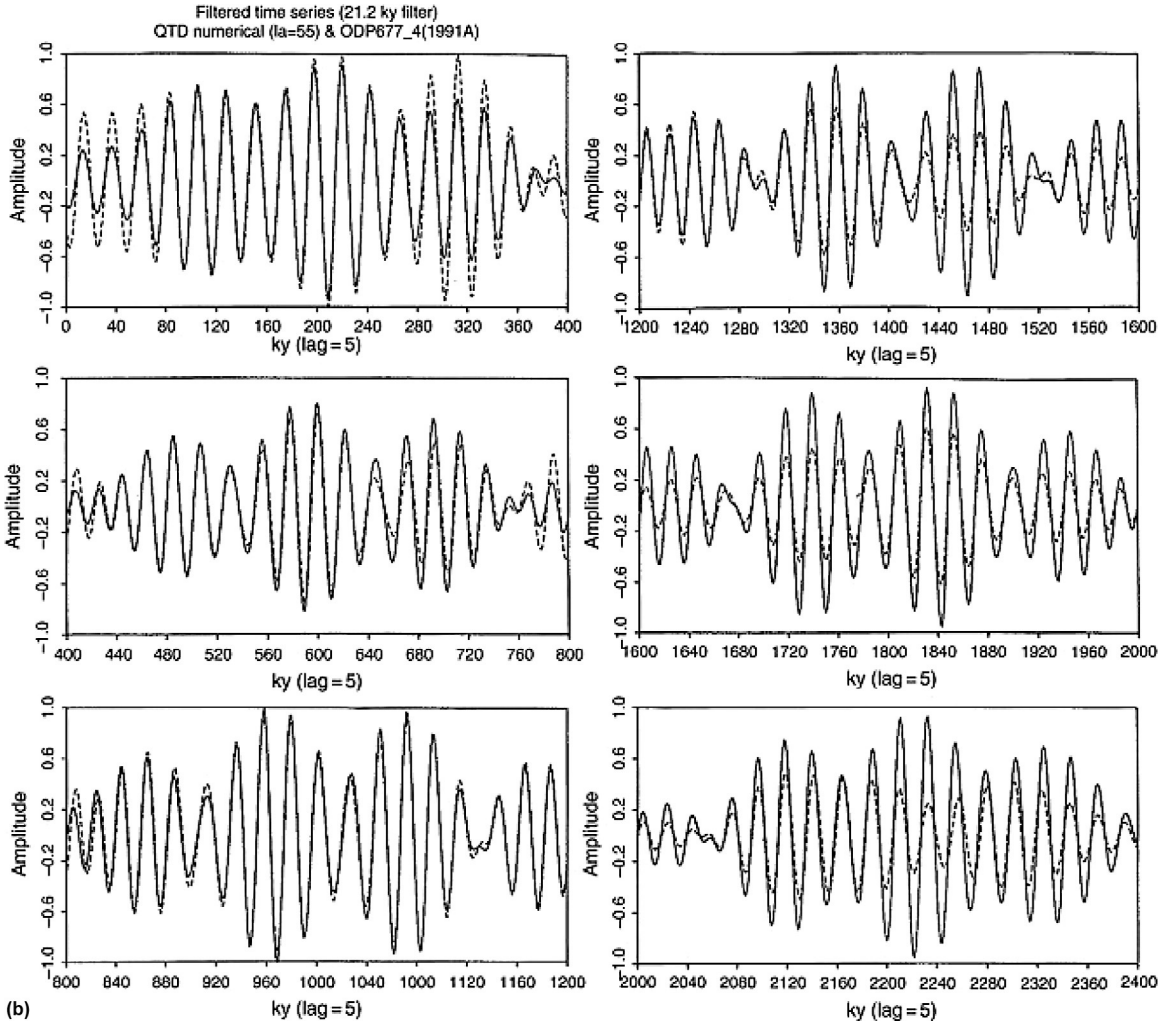

Figure 44, Cont'd (b) Same as **Figure 31(a)** but showing the coherence in the eccentricity–precession band between astronomical forcing and oxygen-isotopic (climate) response. This is the original work that led to the results reported in Shackleton et al. (1990).

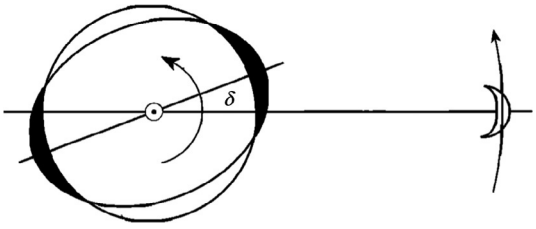

Figure 45 Schematic diagram illustrating the relationship between the tidal bulges in the oceans raised by the gravitational attraction of the Moon and the line joining the centers of mass of the Earth and Moon. The dissipation of ocean tidal energy both due to bottom friction and due to the dissipation of the internal tide leads to a phase lag of the tide and thereby to a torque that acts so as to diminish the rate of axial rotation of the planet and thereby to an increase with time of the l.o.d.

that tidal friction is considerably larger than it has been over much of the geologic past as a consequence of the fact that the ocean basins are currently of a spatial scale such that a near-resonant condition exists between the normal modes of the ocean basins and the tidal forcing insofar as the dominant M_2 tide is concerned. The interested reader will find a highly informative discussion of the tides as free oscillations of the ocean basins in Platzman (1971). This is a fascinating subject about which there is a great deal yet to be learned.

9.09.8.2 Polar Wander and the Impact of Excess Oblateness due to Mantle Convection

On the longest timescales of hundreds of millions of years on which the thermal evolution and internal structure of the Earth are governed by the mantle convection process, debate continues concerning the issue as to whether the relative latitudinal positions of the continents and the variations of their positions through time are to be ascribed solely to the action of the mantle convection-driven process of continental drift and the TPW of the axis of rotation that is expected to accompany it. If it were possible for the relative positions of the continents with respect to the axis about which the planet rotates to be spontaneously modified by a TPW event unrelated to mantle convective mixing, then it would be possible to misinterpret paleomagnetic inferences of paleolatitude as

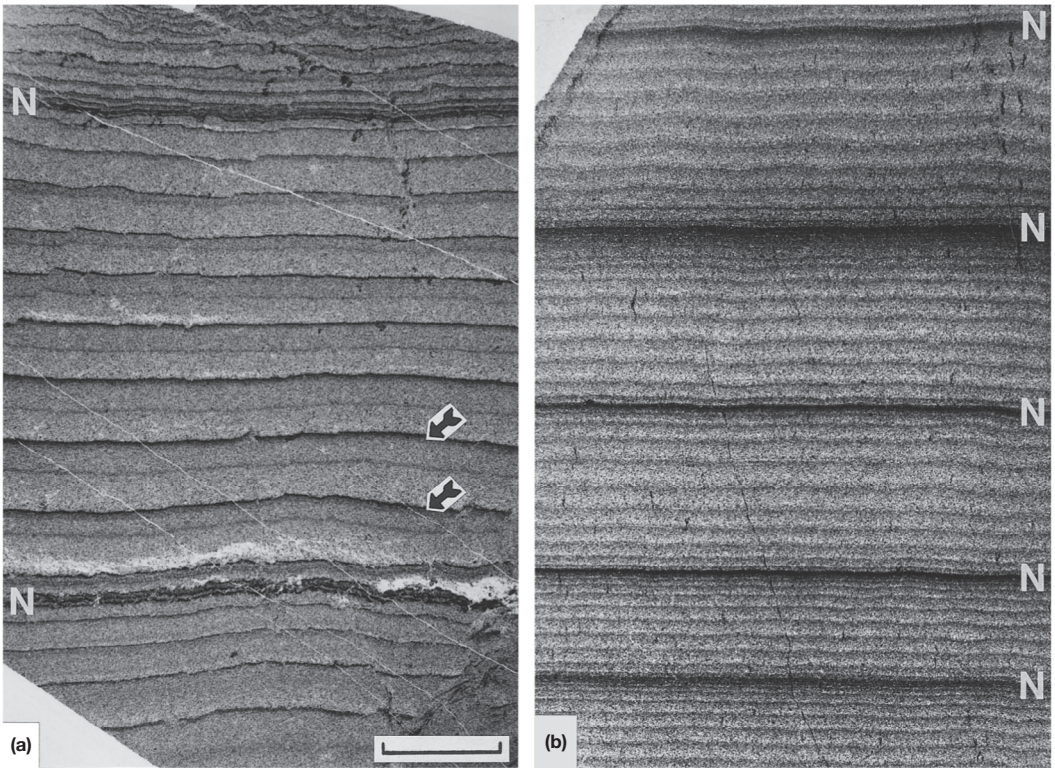

Figure 46 A typical section of tidal rhythmite from the Elatina sedimentary formation of Australia. The banding of the sediments may be interpreted in terms of the variability with time of the amplitude of the ocean tide as Earth executes a single period in its annual orbit around the Sun and the orientation of the Moon with respect to the Earth also varies simultaneously. Reproduced from Williams GE (1997) Precambrian length of day and the validity of tidal rhythmite paleotidal values. *Geophysical Research Letters* 24(4): 421–424.

arising solely due to the action of the convection process when in fact, these were due to the influence of TPW induced by some other causes. The recent resurgence of interest in TPW has come to be focused upon the possibility of occurrence of a so-called inertial interchange instability (e.g., Fisher, 1974; Goldreich and Toomre, 1969; Kirschvink et al., 1997) during which, as a consequence of the axis of greatest moment of inertia being 'suddenly' (on geologic timescales) changed, the geographic positions of the continents with respect to the rotation pole would be subject to a rapid secular shift.

On such long timescales, the issue arises once more as to whether the magnitude of the equatorial bulge represented by the fluid Love number k_f should be taken to be adequately explained by the viscoelastic field theory of Peltier (1974) in which the EQM assumption of Munk and MacDonald (1960) is invoked or whether one must allow for the existence of a bulge whose amplitude is inflated by the convection process by an amount similar to that that is apparently characteristic of the present day, as previously discussed in **Section 9.09.3.5**. Although it has been demonstrated explicitly that the impact of this influence is small insofar as the GIA prediction of polar wander speed and direction for the Late Pleistocene ice-age cycle are concerned (**Section 9.09.5.2**), on the much longer timescales associated with the mantle convection process, the impact of an equatorial bulge of amplitude larger than predicted by $k_2^T(s=0)$ in the limit of zero lithospheric thickness could be much more significant. Here, it will suffice to provide only commentary on a series of recently published or completed analyses.

In Peltier et al. (2007) and Liu and Peltier (2010, 2011), a series of analyses of the snowball Earth events that are hypothesized to have dominated the climate of the Neoproterozoic aeon (e.g., Hoffman and Schrag (2000, 2002)) have been produced. In Peltier et al. (2007), a feedback mechanism was suggested that could have prevented the occurrence of the deep glaciations that some have imagined have occurred, a mechanism that was further explored in the aforementioned Liu and Peltier (2010, 2011) contributions. More recently, further analyses have been performed in Liu and Peltier (2013a,b) to directly investigate the variations in global sea level that would have accompanied these severe glaciation events. Because the timescale of these events is such that they are expected to have lasted at least several million years, they have provided an extremely useful means of investigating the TPW that would have been induced by such a long-timescale surface loading event. For the purpose of these analyses, the version of the SLE formalism described in **Section 9.09.3.5** was employed, which enables a direct assessment of the extent to which such a surface ice-sheet loading event might be expected to produce a significant wander of the rotation pole. These analyses demonstrate that if the excess ellipticity that existed during the glaciation process was of the same order as exists at present, then the excess bulge would have been sufficient to prevent any significant TPW from occurring. Of course, we have no way of knowing whether

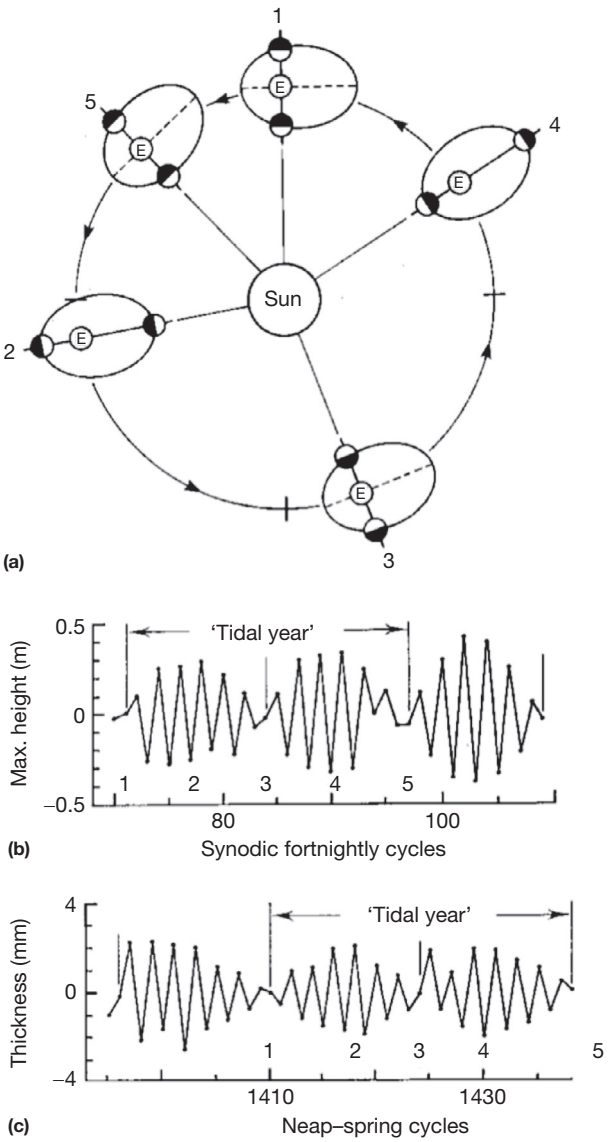

Figure 47 The manner in which the thickness of individual sedimentary bands in the rhythmite shown in **Figure 46** is interpreted in terms of the variations of tidal amplitude between 'spring' and 'neap.' Also shown is the relationship between these phases of the tide and the orbits of the Earth and Moon. Reproduced from Williams GE (2000) Geological constraints on the Precambrian history of Earth's rotation and the Moon's orbit. *Reviews of Geophysics* 38: 37–59.

the modern circumstance is at all characteristic of that that existed in this period of the distant past.

There does exist, however, one potential phenomenon that has been suggested to be a characteristic of the mantle convection process that could, at least in principle, exert 'coherent control' upon the Earth's rotation on a relatively short timescale and which is derivative of the mantle convection process itself. This is the so-called avalanche effect discussed at length by Peltier and Solheim (1992), by Solheim and Peltier (1994a,b), and more recently in Shahnas and Peltier (2010), an effect upon the temporal variability of the convection process that is controlled by the action of the phase transition from spinel to a mixture of perovskite and magnesiowüstite that exists at 660 km depth and which separates the so-called transition zone of the mantle above this level from the lower mantle beneath. The avalanche effect is found to be strong in models of the mantle convection process in which the effective viscosity of the planetary mantle is sufficiently low, as it is in the VM2 and VM5a models that have been developed on the basis of fits to observations of the GIA process discussed in the previous sections of this chapter (see **Figure 27**). Peltier (1998) had argued that this model, or a close relative derived on the basis of analyses of the GIA process, may be equally applicable on the much longer timescale characteristic of convection in the Earth's mantle, although this issue remains a subject of active debate.

Insofar as effort is concerned to confirm the possibility that IITPW may have occurred in the past, a primary era of the Earth history that has been suggested as a candidate has been the early Cambrian period (Kirschvink et al., 1997). Of course, this is an extraordinarily important period of time from the perspective of Earth evolution in general and biological evolution in particular and from the perspective of tectonophysics. From the perspective of biological evolution, it was the time of especially rapid biological diversification that occurred during the so-called Cambrian Explosion of Life. From the perspective of tectonophysics, it was a time immediately following the final phase of the Neoproterozoic breakup of the supercontinent of Rodinia during which the previously discussed series of especially severe episodes of global glaciation are believed to have occurred (e.g., Hoffman and Schrag, 2000, 2002; Kirschvink, 1992). These hypothesized glaciation events have been termed 'snowball glaciations' during which it is imagined that the surface of the Earth may have become entirely ice-covered, the oceans by a thick veneer of sea ice, and the continents by thick continental ice sheets such as those that were confined primarily to the north polar regions during times of ice-age maxima within the Pleistocene era. Although the plausibility of occurrence of the 'hard snowball' state envisioned by these authors has been questioned (e.g., Hyde et al, 2000; Liu and Peltier, 2010, 2011; Peltier et al., 2004, 2007), there is no doubt that the period of transition between the Neoproterozoic and the Cambrian eras, a transition that occurred ~541 million years ago, was a time in Earth history during which plausibly large variations in the elements of the moment of inertia tensor of the planet could have occurred. Not only was the process of mantle convection highly disturbed during the process of the rifting and dispersal of Rodinia, but also there were highly significant exchanges of mass occurring between the oceans and the highly glaciated continents at the end of the final Neoproterozoic snowball event. Li et al. (2004) had in fact proposed that the inferred equatorial location of this supercontinent during the earliest (Sturtian) episode of intense Neoproterozoic glaciation could have arisen as a consequence of a complete 90° inertial interchange instability event during which the supercontinent was shifted from the pole to the equator. It may therefore be the case that the Sturtian ice mass was not emplaced on the supercontinent while it was at the equator but rather when it was in the initial polar location. This is an idea that is suggested as a possibility by the Li et al. analysis of the paleomagnetic data but that was not explicitly envisioned by them.

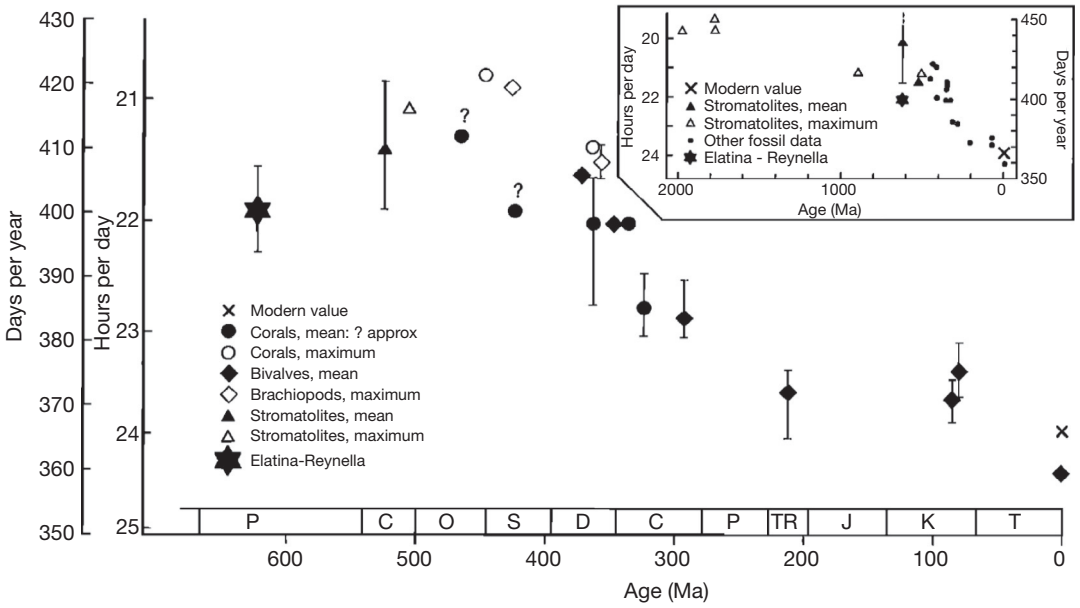

Figure 48 A relatively complete collection of estimates of the variations in the l.o.d. that have been derived from various paleontological proxy data aside from tidal rhythmites. Reproduced from Williams GE (2000) Geological constraints on the Precambrian history of Earth's rotation and the Moon's orbit. *Reviews of Geophysics* 38: 37–59.

Figure 49 illustrates the temporal interrelationships that existed in the Earth system during this critical period in Earth history between the tectonophysical events associated with the mantle convection process and the events that were simultaneously occurring in surface climate variability. The climate-related signal shown in this time series is for the carbon isotopic anomaly denoted $\delta^{13}C$, which is measured in carbonate rocks on land such as those from Namibia, which constitute the type section for much of the work that has been accomplished in support of the snowball Earth hypothesis (Hoffman and Schrag, 2000). The importance of this isotopic measurement derives from the fact that it is strongly influenced by photosynthetic activity as an isotopic fractionation occurs such that the organic matter produced in photosynthesis is enriched in ^{12}C relative to the heavier isotope ^{13}C. A time when the $\delta^{13}C$ that is measured in carbonate rocks that were precipitated from the ocean is high therefore corresponds to a time of high photosynthetic biological productivity. This is because such episodes correspond to times, as indicated on the figure, when the rate of burial of the organic matter produced in photosynthesis is significantly elevated, leaving behind an ocean that is enriched in ^{13}C. The sharp minima that are observed to characterize the time series shown in Figure 49 have therefore been taken to correspond to times in Earth history of intense 'snowball' glaciation during which photosynthetic activity was either sharply diminished or eliminated altogether as would have been the case during a 'hard snowball' event. Also indicated in Figure 49 is the timing of the episodes of intense tectonic activity that would have been associated with the breakup of the supercontinents of Rodinia and, much later during the Carboniferous period, Pangaea. The period of transition between the Neoproterozoic and the Cambrian that Kirschvink has suggested as a possible time of occurrence of an inertial interchange instability event was therefore a time of profound change in Earth history, perhaps the most important such period since the birth of the planet from the primitive solar nebula.

In an attempt to establish the early Cambrian IITPW hypothesis of Kirschvink et al. (1997) as viable, Mound et al (1999) performed a calculation of the expected impact of such an event upon relative sea-level history. Their idea was to see whether observations of relative sea-level history over timescales of millions of years might be employed as a means of determining whether an IITPW event had occurred and the analyses presented were interpreted to imply that the hypothesis not only was viable but also was supported by their initial analysis of the observational constraints they described. An important issue concerning the validity of these analyses concerns the strong dependence of the results obtained upon the thickness of the lithosphere assumed to be characteristic of the Maxwell viscoelastic model employed for the purpose of analyzing the sea-level response to the rotational excitation. Their assumption in this analysis was that the lithosphere could be treated as a complete 'unbroken-by-plate-tectonics' elastic shell over the tens of millions of years during which the IITPW event was imagined to occur. Their results, however, also suggested a very strong dependence upon the thickness assumed such that the response rapidly diminished as the assumed thickness of the lithosphere was reduced. In Sections 9.09.3 and 9.09.5 of this chapter, the question as to how the thickness of the lithosphere was to be treated, insofar as the computation of the rotational response to surface glaciation and deglaciation is concerned, was discussed in detail. There, it was suggested that appropriate treatment of the stabilizing influence of the Earth's equatorial rotational bulge required that the properties of the Maxwell viscoelastic models employed should be such that, although it would be

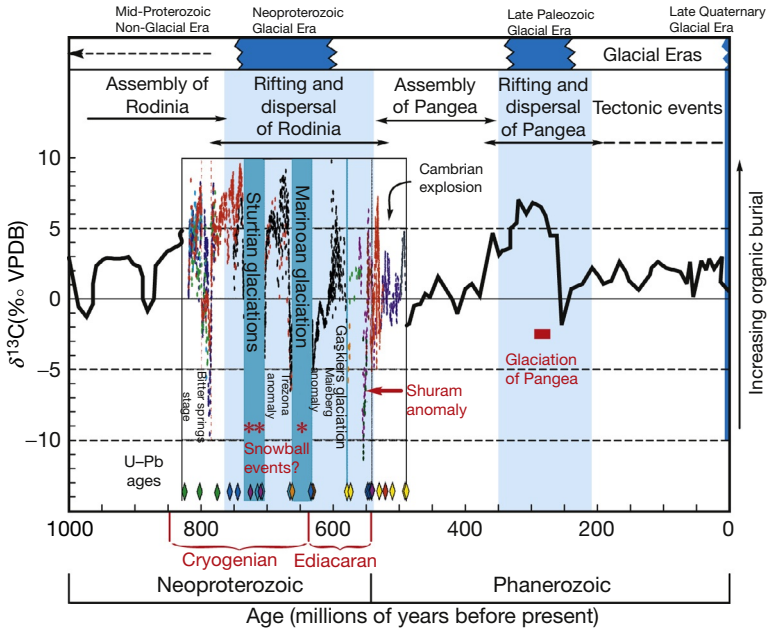

Figure 49 The variation of carbon isotopes, denoted $\delta^{13}C$, over the last 1.6 Ga of the Earth history shown together with the times of occurrence of periods of significant continental glaciation and the times of creation and destruction of supercontinents that accompany the so-called Wilson cycle. The $\delta^{13}C$ time series is from Kauffman (1997) and Hoffman and Schrag (2000), whereas the inset for the Neoproterozoic aeon is based upon the composite data set from Halverson et al. (2005). This figure was originally published in Peltier et al. (2007).

necessary to include any difference between k_f and $k_2^T(s=0)$, this difference should be that appropriate to the limit in which the thickness of the elastic lithosphere is taken to vanish in order that the calculation of the rotational response to the glaciation–deglaciation process produces physically reasonable results. As mentioned in the preceding text in commenting upon the recent results of Liu and Peltier (2013a,b), on the longest timescales, the theory of Peltier and Luthcke (2009) predicts a strong impact of any excess equatorial bulge even in the limit that this excess is taken to be that arising when the elastic thickness of the lithosphere is taken to vanish. It is interesting that the Mound et al. (1999) test of the IITPW hypothesis was not made using this form of the theory but rather a form in which the finite strength of the lithosphere was assumed to persist in the long-timescale limit. This issue should not be taken to rule out the possibility of occurrence of IITPW, however, only to question the validity of the proposed test of the hypothesis in terms of long-timescale variations of relative sea level. It may in fact be possible during a period of rapid reorganization of the convection process, when the strong correlation that exists under modern plate tectonic conditions between plate boundaries and deep mantle upwellings and downwellings may no longer obtain. In such conditions, an influence of finite lithospheric thickness may therefore have existed in which case the Mound et al. results could be applicable.

In searching for a sufficiently intense process of reorganization of the convective circulation that might be responsible for an IITPW event, such as that suggested by Kirschvink to have occurred in the Early Cambrian or Li et al. in the Neoproterozoic, I would be inclined to focus upon the times of occurrence of events related to the supercontinent cycle such as the rifting process during which an initially compact supercontinent is fragmented following the occurrence of 'avalanche' events during which the convective circulation may have made a rather sudden transition from a state of whole mantle flow to a state of layered convection (e.g., see Peltier (1996c) for a review). Peltier et al. (1997) had in fact suggested a close linkage between the so-called Wilson cycle of supercontinent creation and destruction and the continuously recurrent 'avalanche effect' that some detailed fluid mechanical models of the convection process have predicted (e.g., Solheim and Peltier, 1994a,b). Such models do apparently predict the inferred timescale of several hundred million years that appears to separate the times in Earth history during which supercontinents existed. That timescale is most visibly evident in histograms of the sample density of continental rocks of a given age as a function of their age. Such suggestions of the mechanism that could underlie these most dramatic events that may have occurred in the history of the Earth's rotation must remain a subject of speculation in search of firm quantitative justification.

References

Albero MC and Angiolini FE (1983) INGEIS Radiocarbon Laboratory dates I. *Radiocarbon* 25: 831–842.

Albero MC and Angiolini FE (1985) INGEIS Radiocarbon Laboratory dates II. *Radiocarbon* 27: 315–337.

Angulo RJ and Lessa GC (1997) The Brazilian sea level curves: A critical review with emphasis on the curves from Paranagua and Cananeia regions. *Geology* 140: 141–166.

Argus DF, Blewitt G, Peltier WR, and Kreemer C (2011) Rise of the Ellsworth Mountains and parts of the East Antarctic coast observed with GPS. *Geophysical Research Letters* 38: L16303. http://dx.doi.org/10.1029/2011GL048025,2011.

Argus DF and Gross RS (2004) An estimate of motion between the spin axis and the hotspots over the past century. *Geophysical Research Letters* 31: L06614. http://dx.doi.org/10.1029/2004GL019657.

Argus DF and Peltier WR (2010) Constraining models of postglacial rebound using space geodesy: A detailed assessment of model ICE-5G (VM2) and its relatives. *Geophysical Journal International* 181: 607–723. http://dx.doi.org/10.1111/j.1365-246X.2010.

Argus DF, Peltier WR, Drummond R, and Moore AW (2014) The Antarctic component of postglacial rebound model ICE-6G_C (VM5a) based upon GPS positioning, exposure age dating of ice thickness and relative sea level histories. *Geophysical Journal International* 198: 537–563.

Argus DF, Peltier WR, and Watkins MM (1999) Glacial isostatic adjustment observed using very long baseline interferometry and satellite laser ranging geodesy. *Journal of Geophysical Research* 104: 29077–29093.

Baksi AK (1992) $^{40}Ar/^{39}Ar$ dating of the Brunhes-Matuyama geomagnetic field reversal. *Science* 256: 356–359.

Belperio AP, Harvey N, and Bousman RP (2002) Spatial and temporal variability in the Holocene sea-level record of the South Australian coastline. *Sedimentary Geology* 150: 153–169.

Berger A (1978) Long-term variations of daily insolation and Quaternary climatic changes. *Journal of the Atmospheric Sciences* 35: 2362–2367.

Berger A, Imbrie J, Hays JD, Martinsen DG, et al. (1984) In: Berger A, et al. (eds.) The Orbit Theory of Pleistocene Climate: Support from a Revised Chronology of the Marine $\delta^{18}0$ Record in Milankovitch and Climate, pp. 269–306. Norwell, MA: D. Reidel.

Bezerra F, Barreto A, and Sugio K (2003) Holocene sea-level history on the Rio Grande do Norte State coast, Brazil. *Marine Geology* 196: 73–89.

Broecker WS and Van Donk J (1970) Insolation changes, ice volumes, and the $\delta^{18}0$ record in deep sea cores. *Reviews of Geophysics and Space Physics* 8: 169–198.

Butterworth S (1930) Theory of filter amplifiers. *Experimental Wireless and the Wireless Engineer* 7: 536–541.

Calaya MA, Wahr JM, and Bryan FO (1999) Climate-driven polar motion. *Journal of Geophysical Research* 104: 12813–12829.

Camoin GF, Monataggioni LF, and Braithwaite CJR (1984) Late glacial to postglacial sea levels in the Western Indian Ocean. *Marine Geology* 206: 119–146.

Camoin GF, Colonna M, Montaggioni LF, Casanova J, Faure G, and Thomassin BA (1997) Holocene sea level changes and reef development in the southwestern Indian Ocean. *Coral Reefs* 16: 247–259.

Carter WE, Robertson DS, Pyle TE, and Diamante J (1986) The application of geodetic radio interferometric surveying to the monitoring of sea level. *Geophysical Journal of the Royal Astronomical Society* 87: 3–13.

Cazenave A, Dominh K, Guienhut S, et al. (2009) Sea level budget over 2003-2008: A re-evaluation from GRACE space gravimetry, satellite altimetry and Argo. *Global and Planetary Change* 65: 83–88. http://dx.doi.org/10.1016/gloplacha.2008.10.004.

Chambers DP, Wahr J, Tamisiea ME, and Nerem RS (2010) Ocean mass from GRACE and glacial isostatic adjustment. *Journal of Geophysical Research* 115: B11425. http://dx.doi.org/10.1029/2010JB007530.

Chandler SC (1891) On the variation of latitude, I. *Astronomical Journal* 11: 59–61.

Chao BF and Gross RS (1987) Changes in the Earth's rotation and low-degree gravitational field induced by earthquakes. *Geophysical Journal of the Royal Astronomical Society* 91: 569–596.

Chao BF, O'Conner WP, Chang ATC, Hal DK, and Foster JL (1987) Snow load effect on the Earth's rotation and gravitational field, 1979-1985. *Journal of Geophysical Research* 92: 9415–9422.

Cheng MK, Eanes RJ, Shum CK, Schutz BE, and Tapley BD (1989) Temporal variations in low degree zonal harmonics from Starlette orbit analysis. *Geophysical Research Letters* 16: 393–396.

Cheng M, Ries JC, and Tapley BD (2011) Variations in Earth's figure axis from satellite Laser ranging and GRACE. *Journal of Geophysical Research* 116: B01409. http://dx.doi.org/10.1029/2010JB000850.

Cheng M and Tapley BD (2004) Variations in the earth's oblateness during the past 28 years. *Journal of Geophysical Research* 109: B09402. http://dx.doi.org/10.1029/2004JB003028.

Church JA, White NJ, Konikow LF, et al. (2011) Revisiting the earth's sea-level and energy budgets from 1961-2008. *Geophysical Research Letters* 38: L18601. http://dx.doi.org/10.1029/2011GL048794.

Clark JA (1976) Greenland's rapid postglacial emergence: A result of ice-water gravitational attraction. *Geology* 4: 310–312.

Clark JA, Farrell WE, and Peltier WR (1978) Global changes in postglacial sea levels: A numerical calculation. *Quaternary Research* 9: 265–287.

Clark JA and Lingle CS (1977) Future sea level changes due to West Antarctic ice-sheet fluctuations. *Nature* 269: 206–209.

Clark PU, Mitrovica JX, Milne GA, and Tamasea ME (2002) Sea level finger printing as a direct test of the source of meltwater pulse 1a. *Science* 295: 2438–2441.

Codignotto JD, Kokott RR, and Marcomini SC (1992) Neotectonism and sea-level changes in the coastal zone of Argentina. *Journal of Coastal Research* 8: 125–133.

Cox CM and Chao BF (2002) Detection of a large scale mass redistribution in the terrestrial system since 1998. *Science* 297: 831–833.

Dahlen FA (1976) The passive influence of the oceans upon the rotation of the Earth. *Geophysical Journal of the Royal Astronomical Society* 46: 406–663.

Dahlen FA and Smith ML (1975) The influence of rotation on the free oscillations of the Earth. *Philosophical Transactions of the Royal Society of London, Series A* 267: 583–629.

Dalmau W (1997) Critical remarks on the use of medieval eclipse records for the determination of long-term changes in the Earth's rotation. *Surveys in Geophysics* 18: 213–223.

Daly L and Le Goff M (1996) An updated and homogeneous world secular variation database. Part 1. Smoothing of the archaeomagnetic results. *Physics of the Earth and Planetary Interiors* 93: 159–190.

Deblonde G and Peltier WR (1991) A one dimensional model of continental ice-volume fluctuations through the Pleistocene: Implications for the origin of the mid-Pleistocene climate transition. *Journal of Climate* 4: 18–34.

Deblonde G and Peltier WR (1993) Late Pleistocene ice-age scenarios based upon observational evidence. *Journal of Climate* 6: 709–727.

Delibrias G and Laborel J (1971) Recent variations of the sea level along the Brazilian coast. *Quaternia* 14: 45–49.

Dickey JO, Marcus SL, de Viron O, and Fukumori I (2002) Recent Earth oblateness variations: Unravelling climate and postglacial rebound effects. *Science* 298: 1975–1977.

Dickman SR (1977) Secular trend of the Earth's rotation pole: Consideration of motion of the latitude observatories. *Geophysical Journal of the Royal Astronomical Society* 57: 41–50.

Domack E, Duran D, Leventer A, et al. (2005) Stability of the Larsen B ice shelf on the Antarctic Peninsula during the Holocene epoch. *Nature* 436: 681–685.

Dunberry M and Bloxham J (2006) Azimuthal flows in the Earth's core and changes in length of day at millennial timescales. *Geophysical Journal International* 165: 32–46.

Dyurgerov MB (2010) Reanalysis of Glacier Changes from the IGY to the IPY, 1960–2008. Publication 108. Data on Glaciological Studies, 116 pp, Moscow.

Dyurgerov MB and Meier MF (2005) Glaciers and the changing Earth system: A 2004 snapshot. *Occassional Paper No. 58*. Institute of Arctic and Alpine Research, University of Colorado, Boulder, Colorado.

Dziewonski AM and Anderson DL (1981) Preliminary reference Earth model. *Physics of the Earth and Planetary Interiors* 25: 297–356.

Engelhart SE, Horton BP, Douglas BC, Peltier WR, and Tornqvist TE (2010) Spatial variability of Late Holocene and 20th century sea-level rise along the Atlantic coast of the United States. *Geology* 37: 1115–1118. http://dx.doi.org/10.1130/G30360A.1.

Engelhart SE, Peltier WR, and Horton BP (2011) Holocene relative sea level changes and glacial isostatic adjustment of the U.S. Atlantic coast. *Geology* 39: 751–754. http://dx.doi.org/10.1030/G31857.1.

Fairbanks RG (1989) A 17,000 year glacio-eustatic sea level record:influence of glacial melting rates on the Younger Dryas event and deep ocean circulation. *Nature* 342: 637–642. http://dx.doi.org/10.1038/342637a0.

Fairbridge RG (1976) Shellfish-eating preceramic indians in coastal Brazil. *Science* 191: 353–359.

Farrell WE (1972) Deformation of the Earth by surface loads. *Reviews of Geophysics* 10: 761–797.

Farrell WE and Clark JA (1976) On postglacial sea level. *Geophysical Journal of the Royal Astronomical Society* 46: 647–667.

Faure H, Fontes JC, Hebrasd L, Monteillet J, and Pirazolli PA (1980) Geoidal changes and shore-level tilt along Holocene estuaries: Senegal River area, West Africa. *Science* 210: 421–423.

Faure H and Hebrard L (1977) Variations des lignes de ravages au Senegalet au Mauritania au cours de l'Holocene. *Studia Geologica Polonica* 52: 143–157.

Fisher D (1974) Some more remarks on polar wandering. *Journal of Geophysical Research* 79: 4041–4045.

Gegout P and Cazanave A (1991) Geodynamic parameters derived from 7 years of laser data on LAGEOS. *Geophysical Research Letters* 18: 1739–1742.

Gibb JG (1986) A New Zealand regional Holocene eustatic sea-level curve and its application to determination of vertical tectonic movements. *Royal Society of New Zealand Bulletin* 24: 377–395.

Gold T (1955) Instability of the Earth's axis of rotation. *Nature* 175: 526–529.

Goldreich P and Toomre A (1969) Some remarks on polar wandering. *Journal of Geophysical Research* 74: 2555–2567.

Griffiths SD and Peltier WR (2008) Mega-tides in the glacial ocean and rapid climate change. *Geophysical Research Letters* 35: L08605 http://dx.doi.org/10.10292008GL033263.

Griffiths SD and Peltier WR (2009) Modeling of polar ocean tides at the Last Glacial Maximum: Amplification, sensitivity, and climatological implications. *Journal of Climate* 22(11): 2905–2924. http://dx.doi.org/10.1175/2008JCLI2540.1.

Gross RS (1986) The influence of earthquakes on the Chandler wobble during 1977-1983. *Geophysical Journal of the Royal Astronomical Society* 85: 161–177.

Gross RS (2000) The excitation of the Chandler wobble. *Geophysical Research Letters* 27: 2329–2342.

Gross R and Poutanen M (2009) Geodetic observations of glacial isostatic adjustment: Understanding glacial isostatic adjustment: A joint DynaQlim/GGOS Workshop, Espo, Finland, 22–26 June 2009. *EOS* 90(41): 356.

Gross RS and Vondrak J (1999) Astrometric and space-geodetic observations of polar wander. *Geophysical Research Letters* 26: 2085–2088. http://dx.doi.org/10.1029/1999GL900422.

Hall GF, Hill DF, Horton BP, Engelhart SE, and Peltier WR (2013) A high resolution study of tides in Delaware Bay: Past conditions and future scenarios. *Geophysical Research Letters* 40: 338–342. http://dx.doi.org/10.1029/2012GL054675.

Halverson GP, Hoffman PF, Schrag DP, Maloof AC, Rice A, and Hugh N (2005) Toward a Neoproterozoic composite carbon-isotopic record. *GSA Bulletin* 117: 1181–1207.

Hays JD, Imbrie J, and Shackleton NJ (1976) Variations in the earth's orbit: Pacemaker of the ice-ages. *Science* 194: 1121–1132.

Hide R, Birch NT, Morrison LV, Shea DJ, and White AA (1980) Atmospheric angular momentum fluctuations an changes in the length of the day. *Nature* 286: 114–117.

Hill D, Griffiths S, Peltier WR, Horton BP, and Tornquist TE (2011) High resolution numerical Modeling of tides in the Western Atlantic, Gulf of Mexico and Caribbean during the Holocene. *Journal of Geophysical Research: Oceans* 116: C10014. http://dx.doi.org/10.1029/2010JC006896.

Hoffman PF and Schrag DF (2000) Snowball Earth. *Scientific American* 282: 68–75.

Hoffman PF and Schrag DA (2002) The snowball Earth hypothesis: testing the limits of global change. *Terra Nova* 14: 129–155.

Hongre L, Hulot G, and Khoklov A (1998) An analysis of the geomagnetic field over the past 2000 years. *Physics of the Earth and Planetary Interiors* 106: 311–335.

Horton BP, Peltier WR, Culver SJ, et al. (2009) Holocene sea level changes along the North Carolina coastline and their implications for glacial isostatic adjustment models. *Quaternary Science Reviews* 28: 1725–1736. http://dx.doi.org/10.1016/j.quascirev.2009.02.002.

Hyde WT, Crowley TJ, Baum SK, and Peltier WR (2000) Neoproterozoic "snowball Earth" simulations with a coupled climate/ice sheet model. *Nature* 405: 425–430.

Jansen E, Overpeck J, Briffa KR, et al. (2007) Palaeoclimate. In: Solomon S, Qin D, Manning M, Chen Z, Marquis M, Averyt KB, Tignor M, and Miller HL (eds.) *Climate Change 2007: The Physical Science Basis. Contribution of Working Group I to the Fourth Assessment Report of the Intergovernmental Panel on Climate Change*, pp. 433–497. Cambridge: Cambridge University Press.

Jault D and Le Mouel J-L (1993) Circulation in the liquid core and coupling with the mantle. In: Singh RP, Feissel M, Tapley BD, and Shum CK (eds.) *Observations of Earth from Space. Advances in Space Research*, vol. 13. Oxford: Pergamon (11)221–233.

Kauffman AJ (1997) An ice age in the tropic. *Nature* 386: 227–228.

Kirschvink JL (1992) Late Proterozoic low-latitude global glaciation: The snowball Earth. In: Schopf JW and Klein C (eds.) *The Proterozoic Biosphere, a Multidisciplinary Study*, pp. 51–52. Cambridge: Cambridge University Press.

Kirschvink JL, Ripperdan RL, and Evans DA (1997) Evidence for a large-scale reorganization of Early continental masses by inertial interchange true polar wander. *Science* 277: 541–545.

Koba M, Nakata T, and Takahashi T (1982) Late Holocene eustatic changes deduced from geomorphological features and their C-14 dates in the Ryukyu Islands, Japan. *Palaeogeography, Palaeoclimatology, Palaeoecology* 39: 231–260.

Korte M and Constable C (2003) Continuous global geomagnetic field models for the past 3000 years. *Physics of the Earth and Planetary Interiors* 140: 73–89.

Krabil W, Abdalati W, Frederick E, et al. (2000) Greenland Ice Sheet: High elevation balance and peripheral thinning. *Science* 289: 428–430.

Kuehne J and Wilson CR (1991) Terrestrial water storage and polar motion. *Journal of Geophysical Research* 96: 4337–4345.

Lambeck K (1980a) Changes in length-of-day and atmospheric circulation. *Nature* 286: 104–105.

Lambeck K (1980b) *The Earth's Variable Rotation: Geophysical Causes and Consequences*. New York: Cambridge University Press, 449 pp.

Lambeck K (2002) Sea level change from mid-Holocene to recent time: An Australian example with global implications. In: Mitrovica JX and Vermeersen LA (eds.) *Ice Sheets, Sea Level and the Dynamics of the Earth*, *AGU Monographs*, vol. 29, pp. 33–50.

Lambeck K and Chappell J (2001) Sea level change through the last glacial cycle. *Science* 292(5517): 679–686.

Laskar J (1988) Secular evolution of the solar system over 10 million years. *Astronomy and Astrophysics* 198: 341–362.

Li ZX, Evans DAD, and Zhang S (2004) A 90 degree spin on Rodinia: possible causal links between the Neoproterozoic supercontinent, superplume, true polar wander and low latitude glaciation. *Earth and Planetary Science Letters* 220: 409–421.

Liu Y and Peltier WR (2010) A carbon cycle coupled model of Neoproterozoic glaciation. Part I: Influence of continental configuration on the formation of a "soft snowball" *Journal of Geophysical Research: Atmospheres* 115: D17111. http://dx.doi.org/10.1029/2009JD013082.

Liu Y and Peltier WR (2011) A carbon cycle coupled model of Neoproterozoic glaciation. Explicit carbon cycle with stochastic perturbations. *Journal of Geophysical Research: Atmospheres* 116: D02125. http://dx.doi.org/10.1029/2010JD015128.

Liu Y and Peltier WR (2013a) Sea level variations during snowball Earth formation (Part 1): Preliminary analysis. *Journal of Geophysical Research*, *Solid Earth* 118: 4410–4424. http://dx.doi.org/10.1002/jgrb.50293,2013.

Liu Y and Peltier WR (2013b) Sea level variations during snowball earth formation (Part 2): The influence of rotational feedback. *Journal of Geophysical Research: Solid Earth* 118: 4425–4445. http://dx.doi.org/10.1002/jgrb.50294,2013.

Liu Y, Peltier WR, Yang J, and Vettoretti G (2013) The initiation of Neoproterozoic "snowball" climates in CCSM3: The influence of paleocontinental configuration. *Climate of the Past* 9: 2555–2577.

MacKintosh A, Golledge N, Domack E, et al. (2011) Retreat of the Antarctic ice sheet during the last glacial termination. *Nature Geoscience* 4: 195–2002. http://dx.doi.org/10.1038/ngeo1061.

Mackintosh AN, Verleyen E, O'Brien PE, et al. (2013) Retreat history of the East Antarctic ice sheet since Last Glacial Maximum. *Quaternary Science Reviews* 33: 1–21.

Markowitz W (1960) Latitude and longitude and the secular motion of the pole. *Methods and Techniques in Geophysics*, vol. 1, 325–361.

Martin L, Sugio K, Flexor JM, Dominguez JML, and Bittencourt ACSP (1987) Quaternary evolution of the central part of the Brazilian coast, the role of relative sea-level variation and of shoreline drift. In: *Quaternary Coastal Geology of West Africa and South America. UNESCO Reports in Marine Science 43,* pp. 97–145.

Mathews J and Walker RL (1987) *Mathematical Methods of Physics*, 2nd edn. New York: Benjamin.

Mikhailov AA (1971) On the motion of the Earth's poles. *Astronomicheskii Zhurnal* 48: 1301–1304.

Milankovitch M (1940) Canon of Insolation and the Ice Age Problem. Royal Serbian Academy, Special Publications, vol. 132, Section on Math and Natural Sciences, vol. 33, Belgrade (in German, translated by the Israeli Translation Services).

Milne GA and Mitrovica JX (1996) Post-glacial sea level change on a rotating Earth: First results from a gravitationally self-consistent sea-level equation. *Geophysical Journal International* 126: F13–F20.

Mitrovica JX and Peltier WR (1991) On postglacial sea level over the equatorial ocean. *Journal of Geophysical Research* 96: 20053–20071.

Mitrovica JX, Wahr J, Matsuyama I, and Paulson A (2005) The rotational stability of an ice-age Earth. *Geophysical Journal International* 161: 491–506.

Morner NA (1991) Holocene sea level changes in the Tierra del Fuego region. *Boletim IG-USP. Publicação Especial No. 8*, Sao Paulo.

Morrison LV (1973) Rotation of the Earth and the constancy of G. *Nature* 241: 519–520.

Morrison LV and Stephenson FR (2001) Historical eclipses and the variability of the Earth's rotation. *Journal of Geodynamics* 32: 247–265.

Mound JE, Mitrovica JX, Evans DAD, and Kirschvink JL (1999) A sea-level test for inertial interchange true polar wander events. *Geophysical Journal International* 136: F5–F10.

Muller RA and Stephenson FR (1975) The acceleration of the Earth and Moon from early observations. In: Rosenburg GD and Runcorn SK (eds.) *Growth Rhythms and History of the Earth's Rotation*, pp. 459–534. New York: John Wiley.

Munk WH and MacDonald GJF (1960) *The Rotation of the Earth*. New York: Cambridge University Press.

Nakiboglu SM (1982) Hydrostatic theory of the Earth and its mechanical implications. *Physics of the Earth and Planetary Interiors* 28: 302–311.

Nakiboglu SM and Lambeck K (1980) Deglaciation effects on the rotation of the Earth. *Geophysical Journal of the Royal Astronomical Society* 62: 49–58.

Nakiboglu SM and Lambeck K (1981) Deglaciation related features of the Earth's gravity field. *Tectonophysics* 72: 289–303.

Nerem RS and Wahr J (2011) Recent changes in the Earth's oblateness driven by Greenland and Antarctica Mass loss. *Geophysical Research Letters* 38(13): L13501. http://dx.doi.org/10.1029/2011GL047879.

Newton RR (1972) *Medieval Chronicles and the Rotation of the Earth*. Baltimore: Johns Hopkins University Press.

Oba T and Irino T (2012) Sea level at the Last Glacial Maximum, constrained by oxygen isotopic curves of planktonic foraminifera in the Japan Sea. *Journal of Quaternary Science* 27(9): 941–947. http://dx.doi.org/10.1002/jqs.2585.

Peltier WR (1974) The impulse response of a Maxwell Earth. *Reviews of Geophysics and Space Physics* 12: 649–669.

Peltier WR (1976) Glacial isostatic adjustment, II: The inverse problem. *Geophysical Journal of the Royal Astronomical Society* 46: 669–706.

Peltier WR (1982) Dynamics of the ice-age Earth. *Advances in Geophysics* 24: 1–146.

Peltier WR (1983) Constraint on deep mantle viscosity from LAGEOS acceleration data. *Nature* 304: 434–436.

Peltier WR (1985) The LAGEOS constraint on deep mantle viscosity: Results from a new normal mode method for the inversion of viscoelastic relaxation spectra. *Journal of Geophysical Research* 90: 9411–9421.

Peltier WR (1994) Ice-age paleotopography. *Science* 265: 195–201.

Peltier WR (1996a) Physics of the ice-age cycle. In: Duplessy J-C (ed.) *Long Term Climate Variations*, pp. 453–481. Berlin: Springer-Verlag Inc.

Peltier WR (1996b) Mantle viscosity and ice-age ice-sheet topography. *Science* 273: 1359–1364.

Peltier WR (1996c) Phase transition modulated mixing in the mantle of the Earth. *Philosophical Transactions of the Royal Society A* 354: 1425–1447.

Peltier WR (1998) Postglacial variations in the level of the sea: Implications for climate dynamics and solid-Earth geophysics. *Reviews of Geophysics* 36: 603–689.

Peltier WR (1999) Global sea level rise and glacial isostatic adjustment. *Global and Planetary Change* 20: 93–123.

Peltier WR (2002a) Comments on the paper of Yokoyama et al. (2000) entitled "Timing of the last glacial maximum from observed sea level minima" *Quaternary Science Reviews* 21: 409–414.

Peltier WR (2002b) One eustatic sea level history, Last Glacial Maximum to Holocene. *Quaternary Science Reviews* 21: 377–396.

Peltier WR (2002c) Global glacial isostatic adjustment: paleogeodetic and space-geodetic tests of the ICE-4G (VM2) model. *Journal of Quaternary Science* 17: 491–510.

Peltier WR (2004) Global glacial isostasy and the surface of the ice-age Earth: The ICE-5G(VM2) model and GRACE. *Annual Review of Earth and Planetary Sciences* 32: 111–149.

Peltier WR (2005) On the hemispheric origins of meltwater pulse 1a. *Quaternary Science Reviews* 24: 1655–1671.

Peltier WR (2007a) Postglacial coastal evolution: Ice-Earth-Ocean interactions in a period of rapid climate change. In: Harff J, Hay WW, and Tetzlaff DM (eds.) *Coastline Changes: Interrelation of Climate and Geological Processes*. Boulder, CO: The Geological Society of America Inc, Geological Society of America Special Paper 426.

Peltier WR (2007b) History of Earth rotation. In: Schubert G (ed.) *Volume 9 of "The Treatise on Geophysics"*, pp. 243–293. Oxford, UK: Elsevier Press.

Peltier WR (2009) Closure of the budget of global sea level rise over the GRACE era: The importance and magnitudes of the required corrections for global glacial isostatic adjustment. *Quaternary Science Reviews* http://dx.doi.org/10.1016/j.quascirev.2009.04.004.

Peltier WR and Andrews JT (1976) Glacial isostatic adjustment I: the forward problem. *Geophysical Journal of the Royal Astronomical Society* 46: 605–646.

Peltier WR, Argus DF, and Drummond R (2014) Space geodesy constrains Ice-Age terminal deglaciation: The ICE-6G (VM5a) model. *Journal of Geophysical Research: Solid Earth*.

Peltier WR, Butler S, and Solheim LP (1997) The influence of phase transformations on mantle mixing and plate tectonics. In: Crossley DJ (ed.) *Earth's Deep Interior*, pp. 405–430. Amsterdam: Gordon and Breach Publishers Inc.

Peltier WR and Drummond R (2010) Deepest mantle viscosity: Constraints from earth rotation anomalies. *Geophysical Research Letters* 37: L12304. http://dx.doi.org/10.1029/2010GL043219.

Peltier WR, Drummond R, and Roy K (2012) Comment on "Ocean mass from GRACE and glacial isostatic adjustment" by D.P. Chambers et al. *Journal of Geophysical Research, Solid Earth* 117: B11403. http://dx.doi.org/10.1029/2011JB008967.

Peltier WR and Fairbanks RG (2006) Global glacial ice-volume and Last Glacial Maximum duration from an extended Barbados Sea Level record. *Quaternary Science Reviews* 25: 3322–3337.

Peltier WR, Farrell WE, and Clark JA (1978) Glacial isostasy and relative sea-level: A global finite element model. *Tectonophysics* 50: 81–110.

Peltier WR and Jiang X (1996) Glacial isostatic adjustment and Earth rotation: Refined constraints on the viscosity of the deepest mantle. *Journal of Geophysical Research* 101: 3269–3290 (Correction, 1997, *Journal of Geophysical Research* 102: 10101–10103).

Peltier WR, Liu Y, and Crowley JW (2007) Snowball Earth prevention by dissolved organic carbon remineralization. *Nature* 450: 813–818, http://dx.doi.org/10.1038.Nature06354,2007.

Peltier WR and Luthcke SB (2009) On the origins of earth rotation anomalies: New insights on the basis of both "paleogeodetic" data and Gravity Recovery and Climate Experiment (GRACE) data. *Journal of Geophysical Research: Solid Earth* 114: B11405. http://dx.doi.org/10.1029/2009JB006352.2009.

Peltier WR, Shennan I, Drummond R, and Horton B (2002) On the postglacial isostatic adjustment of the British Isles and the shallow viscoelastic structure of the Earth. *Geophysical Journal International* 148: 443–475.

Peltier WR and Solheim LP (1992) Mantle phase transitions and layered chaotic convection. *Geophysical Research Letters* 19: 321–324.

Peltier WR and Solheim LP (2004) The climate of the Earth at Last Glacial Maximum: Statistical equilibrium state and a mode of internal variability. *Quaternary Science Reviews* 23: 335–357.

Peltier WR, Tarasov L, Vettoretti G, and Solheim LP (2004) Climate dynamics in deep time: Modeling the "snowball bifurcation" and assessing the plausibility of its occurrence. In: Jenkins G, McMennamin MAS, McKay CP, and Sohl L (eds.) *The Extreme Proterozoic: Geology, Geochemistry, and Climate*. *AGU Monograph*, vol. 146, pp. 107–124. Washington, DC: AGU Press.

Pirazzoli PA (1978) High stands of Holocene sea level in Northwest Pacific. *Quaternary Research* 10(1): 1–29.

Platzman GW (1971) Ocean tides and related waves. In: Reid WH (ed.) *Mathematical Problems in the Geophysical Sciences*. *Inverse Problems, Dynamo Theory and Tides*, vol. 2. Providence Rhode Island: American Mathematical Society.

Ponte RM, Stammer D, and Marshall J (1998) Oceanic signals in observed motions of the Earth's pole of rotation. *Nature* 391: 476–479.

Porter SC, Stuiver M, and Heusser CJ (1984) Holocene sea level changes along the Strait of Magellan and Beagle Channel, Southernmost South America. *Quaternary Research* 22(1): 59–67.

Proverbio E and Queseda V (1974) Secular variation in latitudes and longitudes and continental drift. *Journal of Geophysical Research* 79: 4941–4943.

Quinn TR, Tremaine S, and Duncan M (1991) A three million year integration of the Earth's orbit. *Astronomical Journal* 101: 2287–2305.

Ratcliff JT and Gross RS (2010) Combinations of Earth orientation measurements: SPACE2009, COMB2009 and POLE2009. Jet propulsion Laboratory Pbl. 10-22, 29 pp., Pasedena, CA.

Rochester MG and Smiley DE (1965) Geomagnetic core-mantle coupling and the Chandler wobble. *Geophysical Journal of the Royal Astronomical Society* 10: 289–315.

Rodell M, Houser PR, Jambor U, et al. (2004) The global Ly Greenland and data assimilation system. Bull. *American Meteorological Society* 85: 381–391.

Rostami K, Peltier WR, and Mangini A (2000) Quaternary marine terraces, sea level changes and uplift history of Patagonia, Argentina: Comparisons with predictions of the ICE-4G (VM2) model of the global process of glacial isostatic adjustment. *Quaternary Science Reviews* 19: 1495–1525.

Roy K and Peltier WR (2011) GRACE era secular trends in Earth rotation parameters: A global scale impact of the global warming process? *Geophysical Research Letters* 38: L10306. http://dx.doi.org/10.1029/2011GL047282.2011.

Rubincam DR (1984) Postglacial rebound observed by LAGEOS and the effective viscosity of the lower mantle. *Journal of Geophysical Research* 89: 1077–1087.

Sabadini R and Peltier WR (1981) Pleistocene deglaciation and the Earth's rotation: implications for mantle viscosity. *Geophysical Journal of the Royal Astronomical Society* 66: 553–578.

Salehipour H, Stuhne GD, and Peltier WR (2013) A higher order discontinuous Galerkin, global shallow water model: global ocean tides and aquaplanet benchmarks. *Ocean Modelling* 69: 93–107.

Sauriau A and Cazanave A (1985) Re-evaluation of the seismic excitation of the Chandler wobble from recent data. *Earth and Planetary Science Letters* 75: 410–416.

Schofield JC (1975) Sea-level fluctuations cause periodic post-glacial progradation, South Kaipara Barrier, North Island, New Zealand. *New Zealand Journal of Geology and Geophysics* 18: 295–316.

Shackleton NJ (1967) Oxygen isotope analysis and Pleistocene temperatures re-addressed. *Nature* 215: 15–17.

Shackleton NJ (2000) The 100,000 year ice-age cycle identified and found to lag temperature, carbon dioxide, and orbital eccentricity. *Science* 289: 1897–1902.

Shackleton NJ, Berger A, and Peltier WR (1990) An alternative astronomical calibration of the lower Pleistocene timescale based upon ODP 677. *Transactions of the Royal Society of Edinburgh: Earth Sciences* 81: 251–261.

Shackleton NJ and Opdyke ND (1973) Oxygen isotope and paleomagnetic stratigraphy of equatorial Pacific core V28-238: Oxygen isotope temperatures and ice volumes on a 10^5-year time scale. *Quaternary Research* 3: 39–55.

Shahnas H and Peltier WR (2010) Layered convection and the impacts of the Perovskite-post Perovskite phase transition on mantle dynamics under isochemical

conditions. *Journal of Geophysical Research: Solid Earth* 115: B11408. http://dx.doi.org/10.1029/2009JB007199.
Solheim LP and Peltier WR (1994a) Avalanche effects in phase transition modulated thermal convection: A model of earth's mantle. *Journal of Geophysical Research* 99: 6997–7018.
Solheim LP and Peltier WR (1994b) 660 km phase boundary deflections and episodically layered isochemical convection. *Journal of Geophysical Research* 99: 15861–15875.
Stephenson ER and Morrison LV (1995) Long term fluctuations in the earth's rotation: 700 B.C. to A.D. 1990. *Philosophical Transactions of the Royal Society of London, Series A: Mathematical, Physical and Engineering Sciences* 351: 165–202.
Stuiver M and Reimer PJ (1993) Extended ^{14}C data base and revised calib. 3.0 ^{14}C age calibration program. *Radiocarbon* 35: 215–230.
Sugihara K, Nakamori T, Iryu Y, Sasakai K, and Blanchon P (2003) Holocene sea-level change and tectonic uplift deduced from raised reef terraces, Kikai-jima, Ryukyu Islands, Japan. *Sedimentary Geology* 159: 5–25.
Tapley BD, Bettadpur JC, Ries JC, Thompson PF, and Watkins M (2004) GRACE measurements of mass variability in the Earth system. *Science* 305: 503–505.
Tarantola A and Valette B (1982a) Inverse problems = quest for information. *Journal of Geophysics* 50: 159–170.
Tarantola A and Valette B (1982b) Generalized nonlinear inverse problems solved using the least squares criterion. *Reviews of Geophysics* 20: 219–232.
Tarasov L and Peltier WR (2002) Greenland glacial history and local geodynamic consequences. *Geophysical Journal International* 150: 198–229.
Tarasov L and Peltier WR (2005) Arctic freshwater forcing of the Younger-Dryas cold reversal. *Nature* 435: 662–665.
Tarasov L and Peltier WR (2006) A calibrated deglacial chronology for the North American continent: Evidence of an Arctic trigger for the Younger-Dryas event. *Quaternary Science Reviews* 25: 659–688.
Thomas R, Frederik E, Krabill W, Manizade S, and Martin C (2006) Progressive increase in ice loss from Greenland. *Geophysical Research Letters* 33: L10503. http://dx.doi.org/10.1029/2006GL026075.
Valastro S Jr., Davis EM, Vallrela AG, and Ekland-Olson C (1980) University of Texas at Austin radiocarbon dates XIV. *Radiocarbon* 22: 1090–1115.
Velicogna I and Wahr J (2006a) Acceleration of Greenland ice mass loss in spring 2004. *Nature* 443(7109): 329–331.
Velicogna I and Wahr J (2006b) Measurements of time variable gravity show mass loss in Antarctica. *Science* 311: 1754–1756.
Vincente RO and Yumi S (1969) Co-ordinates of the pole (1899-1968) returned to the conventional international origin. *Publications of the International Latitude Observatory of Mizusawa* 7: 41–50.
Vincente RO and Yumi S (1970) Revised values (1941-1961) of the co-ordinates of the pole referred to the CIO. *Publications of the International Latitude Observatory of Mizusawa* 7: 109–112.
Vondrak J (1984) Long period behaviour of polar motion between 1900.0 and 1980.0. *Annals of Geophysics* 3: 351–356.
Waelbroeck C, Labyrie L, Michel E, et al. (2002) Sea-level and deep water temperature changes derived from benthic foraminifera isotopic records. *Quaternary Science Reviews* 21(1–3): 295–305.
Wahr JM (1982) The effects of the atmosphere and oceans on the Earth's wobble-I. Theory. *Geophysical Journal of the Royal Astronomical Society* 70: 349–372.
Wahr JM (1983) The effects of the atmosphere and oceans on the Earth's wobble and on the seasonal variations in the length of day-II. Results. *Geophysical Journal of the Royal Astronomical Society* 74: 451–487.
Widder DV (1946) *The Laplace Transform*. Princeton, NJ: Princeton University Press.
Williams GE (1997) Precambrian length of day and the validity of tidal rhythmite paleotidal values. *Geophysical Research Letters* 24(4): 421–424.
Williams GE (1998) Precambrian tidal and glacial clastic deposits: Implications for Precambrian Earth-Moon dynamics and paleoclimate. *Sedimentary Geology* 120: 53–74.
Williams GE (2000) Geological constraints on the Precambrian history of Earth's rotation and the Moon's orbit. *Reviews of Geophysics* 38: 37–59.
Wilson CR and Haubrich RA (1976) Meteorological excitation of the Earth's wobble. *Geophysical Journal of the Royal Astronomical Society* 46: 707–743.
Wilson CR and Vincente RO (1990) Maximum likelihood estimates of polar motion parameters. In: McCarthy DD and Carter WE (eds.) *Variations in Earth Rotation*. *American Geophysical Union Monograph Series*, vol 59, pp. 151–155. Washington, DC: AGU.
Wu P and Peltier WR (1984) Pleistocene deglaciation and the Earth's rotation: A new analysis. *Geophysical Journal of the Royal Astronomical Society* 76: 202–242.
Yoder CF (1995) www.agu.org/references/geophys/4_Yoder.pdf.
Yoder CF, Williams JG, Dickey JO, Schutz BE, Eanes RJ, and Tapley BD (1983) Secular variation of the Earth's gravitational harmonic J_2 coefficient from LAGEOS and non-tidal acceleration of Earth rotation. *Nature* 303: 757–762.
Yokoyama Y, Lambeck K, DeDekkar P, Johnston P, and Fifield LK (2000) Timing of the Last Glacial Maximum from observed sea level minima. *Nature* 406: 713–716 (Correction, 2001, *Nature* 412: 99).